GEORGIA INSTITUTE OF TECHNOLOGY
OFFICE OF CONTRACT ADMINISTRATION
SPONSORED PROJECT INITIATION

Date: July 2, 1979

Project Title: *Development of High Stiffness Aluminum Alloy from Rapidly Solidified Powders for Aerospace Structural Applications.*

Project No: *E-19-675* Green card

Project Director: *Dr. E. A. Starke, Jr.*

Sponsor: *Lockheed Missiles and Space Company, Inc. - Palo Alto, CA*

Agreement Period: From *1/16/79* Until ~~2/28/81~~ 9/30/82

Type Agreement: *Subcontract No. HJ80C2630R (under Air Force Prime Contract No. F33615-78-C-5203)*

Amount: *$76,477 (partially funded at $21,905 through 9/5/79)*

Reports Required:

Sponsor Contact Person (s):

Technical Matters

Contractual Matters
(thru OCA)

J. F. Kern, Orgn. 50-43, B/204
Lockheed Missiles and Space Co., Inc.
3251 Hanover Street
Palo Alto, CA 94304

Defense Priority Rating: *DO-A2 under DMS Reg. 1*

Assigned to: *Chemical Engineering* (School/Laboratory)

COPIES TO:

- Project Director
- Division Chief (EES)
- School/Laboratory Director
- Dean/Director—EES
- Accounting Office
- Procurement Office
- Security Coordinator (OCA)
- Reports Coordinator (OCA)
- Library, Technical Reports Section
- EES Information Office
- EES Reports & Procedures
- Project File (OCA)
- Project Code (GTRI)
- Other

CA-3 (3/76)

GEORGIA INSTITUTE OF TECHNOLOGY OFFICE OF CONTRACT ADMINISTRATION

S/R 3/9/10

SPONSORED PROJECT TERMINATION SHEET

Date August 1, 1983

Project Title: "Development of High Stiffness Aluminum Alloy from Rapidly Solidified Powders for Aerospace Structural Applications"

Project No: E-19-675

Project Director: Dr. Edward A. Starke, Jr.

Sponsor: Lockheed Missiles and Space Company

Effective Termination Date: 9-30-82

Clearance of Accounting Charges: 9-30-82

Grant/Contract Closeout Actions Remaining:

- [X] Final Invoice and Closing Documents
- [ ] Final Fiscal Report
- [X] Final Report of Inventions
- [X] Govt. Property Inventory & Related Certificate
- [ ] Classified Material Certificate
- [ ] Other _____

Assigned to: Chemical Engineering (School/~~Laboratory~~)

COPIES TO:

Administrative Coordinator	Research Security Services	EES Public Relations (2)
Research Property Management	Reports Coordinator (OCA) ✓	Computer Input
Accounting	Legal Services (OCA)	Project File
Procurement/EES Supply Services	Library	Other _____

FORM OCA 10:781

12/11/79

Del No 7

GEORGIA INSTITUTE OF TECHNOLOGY

Contract Administration/Georgia Tech Research Institute

Atlanta, Georgia 30332

TELECOPIER: (404) 894-3120

(3M/4 MINUTE AUTOMATIC)

VERIFICATION: (404) 894-4850

TO: DR. R. E. LEWIS
LOCKHEED MISSILES
PALO ALTO, CA

ADDRESSEE'S NO. 415-493-4411 (45743)

TELECOPIER NO. 415-493-4411 (x45747)

VERIFICATION NO. 415-493-4411 (x45711)

FROM: E. A. STARKE

CAMPUS EXT. 2880

DEPT.: CHEM ENG.

CHARGE NO. E-19-6745

THIS TRANSMISSION CONSISTS OF 3 PAGES

(Excluding Leader Page)

OCA CONFIRMATION DESK

Date 12-11-79 Time 4:00 Operator RB

TRANSMITTED: ✓

TLX____

TWX____

Postal cable____

Air Mail letter____

Express____

Telegram____

FAX ✓

RECEIVED:____

Person notified:____

Time:____ Date:____

NOTE:

xc: Starke

Task 3 - Quantitative Microstructural
Analysis and Mechanical Property Correlations

This task is being performed by Georgia Institute of Technology

Tensile Properties

In addition to the tensile tests carried out on the underaged, peak aged and overaged conditions of alloys 1.2 and 1.6 a few tests on alloy 1.2 were performed in the as-quenched condition. The yield stress was found to be fairly low ($\sigma_{0.2} \approx 325$ M Pa), while the elongation to fracture did not increase drastically ($\epsilon \approx 8\%$) as compared to the underaged condition of the same alloy ($\epsilon \approx 2.8\%$).

The relatively low yield stress values of both alloys in the peak aged condition, which are far below goal B, are also lower than the values given in Table 9 of the Intrium Technical Report (LMSC - D 67877). One reason for this discrepancy might be the slightly higher ageing temperature of 200°C as compared to the ageing temperature of 190°C for the previous specimens. A few tensile tests will therefore be performed on specimens aged at a lower temperature. It might be possible to increase the volume fraction of the δ' - precipitates by decreasing the ageing temperature. This should increase the yield stress.

Microstructural Observations

From TEM studies it was observed that the subgrain size in alloy 1.2 ranged from about 2 to 4 μm, while in alloy 1.6 a size of about 5 μm was found. The δ' - precipitates in the underaged condition exhibited sizes of about 200 to 200 Å in diameter for both alloys. The precipitate free zones along grain boundaries are approximately 0.1 - 0.15 μm wide in both alloys.

The peak aged condition was studied so far only for alloy 1.6. The size of the δ' - precipitates increased to approximately 200 to 300 Å, as compared

to the underaged condition. The width of the precipitate free zones also increased to about 0.2 μm.

A brief survey of one TEM - foil of alloy 1.6 in the overaged condition showed a somewhat surprising result. It was not possible to find superlattice reflections in the diffraction pattern due to δ' - precipitates. Since it is Known from previous studies that an ageing treatment of 100 h at 200°C does not lead to the dissolution of the δ' - precipitates, this preliminary result will be rechecked for other specimens.

Fracture Surface Observations

The low elongation to fracture values as well as the low true fracture strains, found for all ageing treatments of alloy 1.2 and 1.6, seem to be due to delamination along the flake boundaries. This can be seen by the observation of long cracks on the surfaces of tensile specimens running parallel to the loading axis or extrusion direction. Cracks of this type were also found on the fracture surface of all tensile specimens. Crack nucleation seems to occur at or near the specimen surface for all aging treatments, even for the specimens of alloy 1.2 in the as-quenched condition. The nucleation of cracks at prior flake boundaries, decorated with oxide layers, would explain the minor response of the elongation to fracture values with regard to the different heat treatments, although a large variation in strength was observed between the as-quenched, underaged, peak aged, and overaged conditions.

The fracture surfaces of the underaged and peak aged conditions of both alloys seem to indicate that, once crack nucleation occurred, the cracks propagate mainly along grain or subgrain boundaries. This type of fracture made leads to small dimples covering the individual grain or subgrain boundaries. The distances between these dimples were observed to be

approximately 0.5 μm. It is yet to be found whether these dimples are nucleated at grain boundary particles or formed by ductile tearing within the soft precipitate free zones.

The fracture surfaces of tensile specimens in the overaged conditions of both alloys are somewhat different compared to the underaged and peak aged microstructures. The whole fracture surfaces as well as the specimen surfaces seem to be covered with a layer, which could be the result of a corrosion process due to the surrounding laboratory air. It is therefore difficult to establish which fractures on the fracture surfaces of the overaged conditions belong to the fracture process and which are due to the corrosion process.

It will be noted that similar surface effects were observed on polished samples, prepared for light microscopy studies. This corrosive effect seems to be more pronounced in alloy 1.6 than in alloy 1.2.

January 8, 1980

TO: Dr. R. E. Lewis
Lockheed Missiles
Palo Alto, CA

ADDRESSEE'S NO: (415) 493-4411 (45743)
TELECOPIER NO: (415) 493-4411 (x45747)
VERIFICATION NO. (415) 493-4411 (x45711)

FROM: E. A. Starke,
Chem Eng.

CAMPUS EXTENSION 2880
CHARGE NO: E-19-675

1 of 1 pages

Tensile specimens were machined from extrusions of alloys 1.2 and 1.6 in the longitudinal direction. Gage length was one inch and gage diameter was 0.16 inch.

The pre-machining heat-treatment consisted of solution treating at 812K (1002F) for 0.5 hr., ice water quenching, and aging at 453K (356F) for 1, 10 or 100 hrs. Preliminary tensile test results at room temperature are as follows:

Alloy 1.6

Aging Time (hrs.)	Yield Strength (MPa)	Fracture Stress (MPa)	Elongation (%)
10	387 (0.1%)	387	0.5
10*	368 (0.1%)	375	0.6
100	385 (0.1%)	385	0.6
100*	370 (0.1%)	370	0.9

Alloy 1.2

1	467 (0.2%)	472	1.0
1*	387 (0.2%)	387	0.7
100	404 (0.2%)	483	1.0
100*	412 (0.2%)	427	1.0

* Machined from center of extrusion

Elongation to fracture was 1% or less for all samples tested. Delamination along prior particle boundaries dominated most of the fracture surfaces. For all of the aging times tested, there was an increase in fracture stress for samples machined from material near the edge of the extrusion. This may be due to enhanced oxide breakup during extrusion. Fractographic and microscopic examination will follow, in order to document possible reasons for the low ductility.

Transmission electron microscopy studies of Alloy 1.2 were performed for the peak aged and overaged conditions. In the peak aged condition (8h 200°C) spherical $\bar{C}'$-precipitates were observed with sizes of about 300 to 500 Å. The width of the precipitate free zones increased slightly to about 0.2 μm as compared to a value of 0.1 to 0.15 μm observed for the underaged microstructure. Within the matrix Θ'-precipitates were found. The maximum lengths of these platelets are approximately 1 μm and the thickness is about 100 Å. Very often a large number of much smaller Θ'-platelets was found along low angle boundaries, with platelet trace lengths of about 0.15 μm.

No superlattice spots due to S'-precipitates were found so far ~~in~~ in the overaged condition. This finding will be confirmed by studying foils taken from samples with intermediate aging times at 200°C. The only precipitates found so far in the overaged condition are Θ'-precipitates. The maximum length of the observed platelet-traces is approximately 1 μm and the thickness is about 150 Å.

DARPA

Monthly Letter Report
April 15, 1980

Tensile tests were conducted for alloys 1.2A-3 (Al-3Li-2Cu-0.2Zr) and 1.6 A-2 (Al-3Li-1.5Mn) extruded at a 20:1 reduction ratio. The specimens were solution treated in a lead bath at 1000°F for 0.5 h, ice water quenched, room temperature aged for two days, and artificaially aged in a 190°C oil bath for 0.75, 8 or 40 h. The test results, given in Table 1, indicate increases in yield stress values over those reported previously.

Samples of alloy 1.2A-3 were subjected to solution treating (at 1000°F), quenching (ice water), room temperature rolling and aging at 190°C. TEM observations of 10% reduction followed by 8 h aging revealed an increased volume fraction of fine σ' precipitates. Tensile tests of 14% reduction, peak-aged specimens did not indicate any improvement in either yield strength or ductility.

Compression testing of alloy 1.2 has been initiated to facilitate examination of the deformation structure.

TABLE 1

Alloy	Aging Time at 190°C (hrs)	$\sigma_{0.2}$ (MPa)	σ_f (MPa)	ε_P (%)	ε_T (%)
1.2A-3	0.75	466	561	3.09	3.84
		456	553	3.50	4.19
	8.0	515	591	2.63	3.13
		506	552	1.40	2.18
	40	448	546	3.59	4.33
		438	553	5.34	6.00
1.6A-2	0.75	382	525	4.91	5.53
		384	477	3.09	3.75
	8.0	431	555	3.92	4.59
		442	560	4.00	4.66
	40	423	545	4.25	4.84
		425	537	3.81	4.42

3.3 Task 3 - Quantitative Microstructural Analysis and Mechanical Property Correlations

This task is being performed by Georgia Institute of Technology, with Dr. E. A. Starke, Jr. as principal investigator.

Additional tensile tests were conducted for alloys 1.2A (Al-3Li-2Cu-0.2Zr) and 1.6A (Al-3Li-1.5Mn), extruded to a rectangular bar at a reduction ratio of 20:1. The specimens were solution treated in a lead bath at 811K (1000°F) for 0.05 hr., ice water quenched, aged at room temperature for 2 days, and artificially aged in an oil bath at 463K (375°F) for 0.75, 8, or 40 hrs. The test results are presented in Table 1. For the peak aged condition, the yield and ultimate tensile strength results are higher than those reported previously. One possible explanation for this increase is the beneficial effect of rapid heating to solution treating and aging temperatures by the lead bath and oil bath procedures, respectively, compared to still air and circulating air heating procedures.

Samples of alloy 1.2A (extrusion 1.2A-3) were solution treated at 811K (1000°F), ice water quenched, rolled 10 or 14 percent reduction at room temperature and aged at 463K (375°F) for 8 hr. In the material cold rolled 10 percent reduction, TEM observations revealed an increased volume fraction of the δ' precipitate, compared to un-cold rolled material. In the material cold rolled 14 percent, tensile tests disclosed no improvement in either yield strength or ductility.

A compression test of alloy 1.2A has been initiated to facilitate study of the plastic deformation structure.

3.4 Task 4 - Application Studies

This task is being performed by Lockheed-California Company, with Messrs. G. Wald and J. E. Rhodes as principal investigators.

DARPA Report
8/22/80

The crystallographic texture was determined for the extrusions 1.2 A-1, -5, -10, -11 and -12. CuK_{α} radiation was used, at a setting of 20 ma and 35 kV. one inch square samples were prepared by aligning rectangular sections from the center of the extrusions. Intensities were plotted by computer for the (111), (200) and (220) poles, with the center of the pole figure corresponding to the extrusion axis. Pole figures for rectangular extrusions are oriented with respect to the thickness and width directions, where the thickness direction is vertical, and the width is horizontal.

The contour lines represent an increment of intensity which is consistent for each pole group. This allows direct, quantitative comparison of the figures within each group. The increments were chosen to produce 30 contour lines in the most sharply textured figure of each group.

The deviation from complete radial symmetry in the pole figures for the axisymmetric extrusions (1.2 A-10 and 1.2 A-12) is presumably due to the rectangular shape of the components of the one-inch-square, mosaic samples.

The pole figures follow. The pole figure captions are explained on the first pole figure.

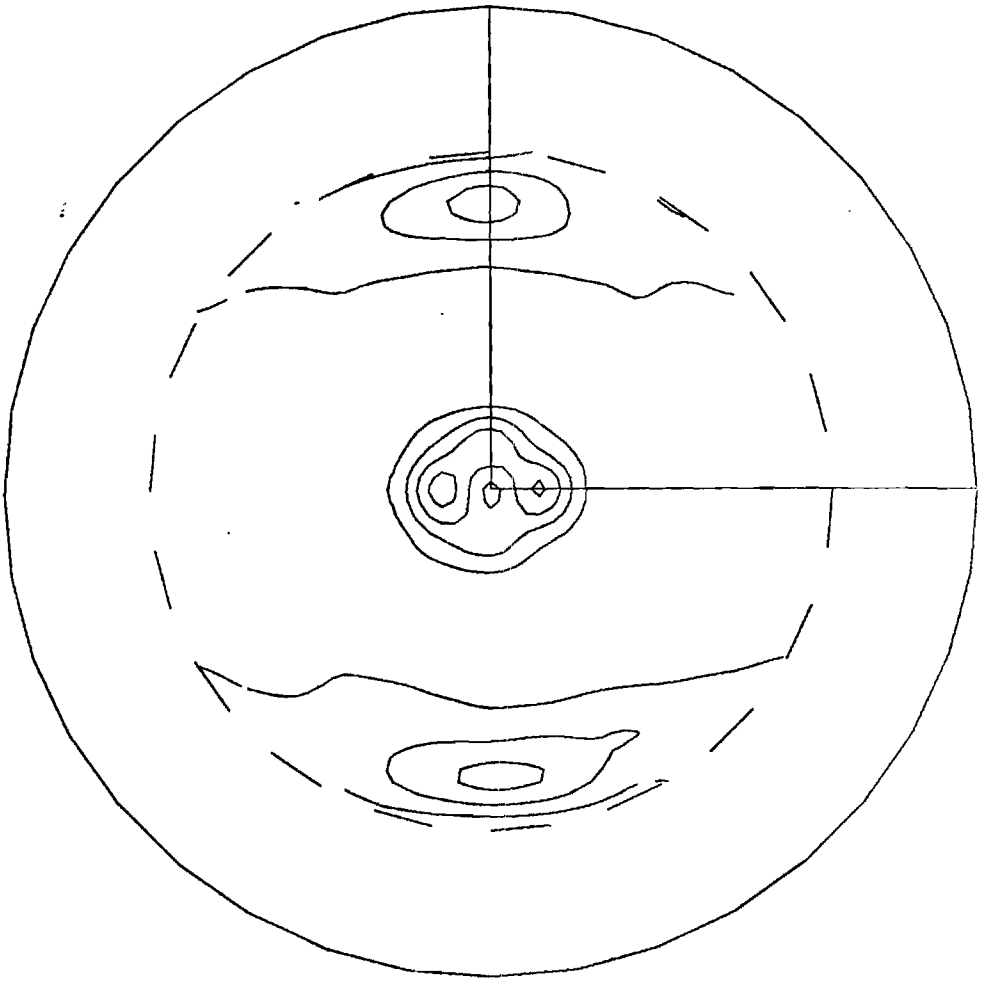

2169.415

1.2 A-1 8/1 (111) 4.974

.212

rect. width 1.09"
0.39"

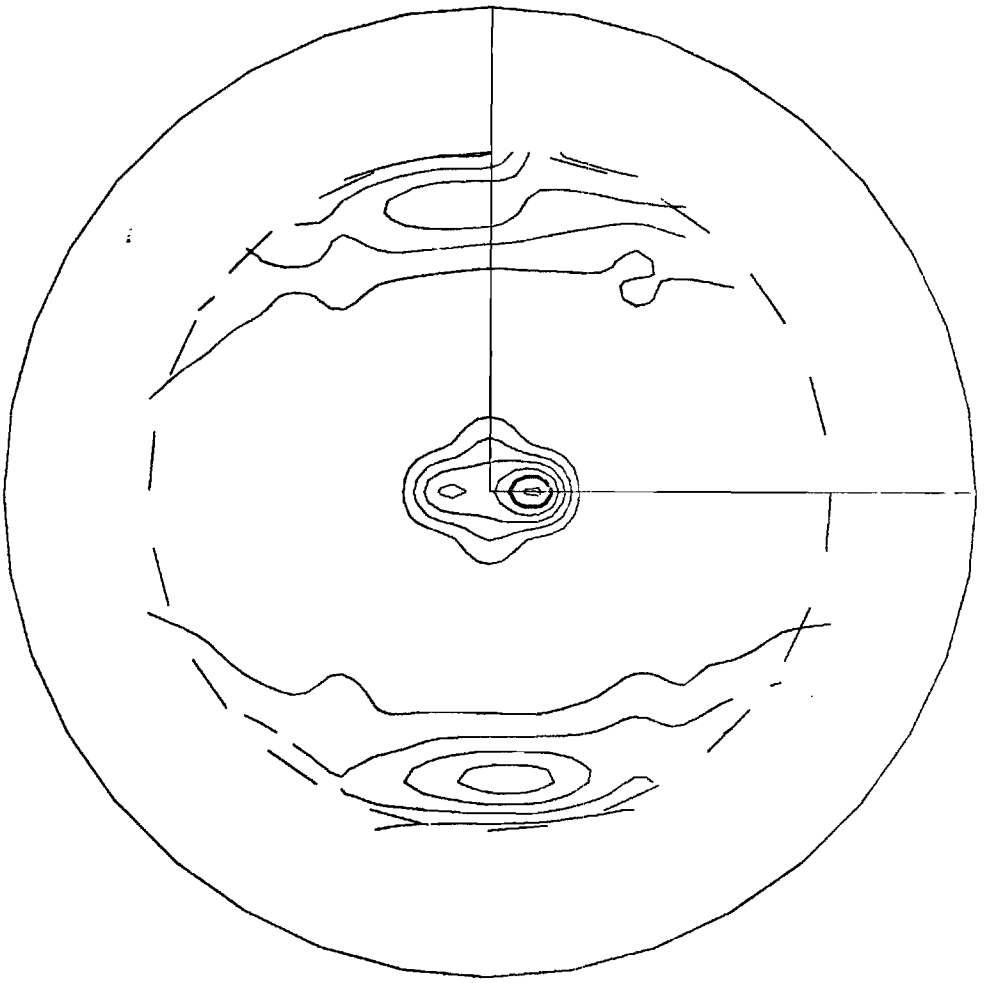

2058.053

1.2 A-5 (111) 6.542

.141

width .580

thick .293"

a/R 2.0

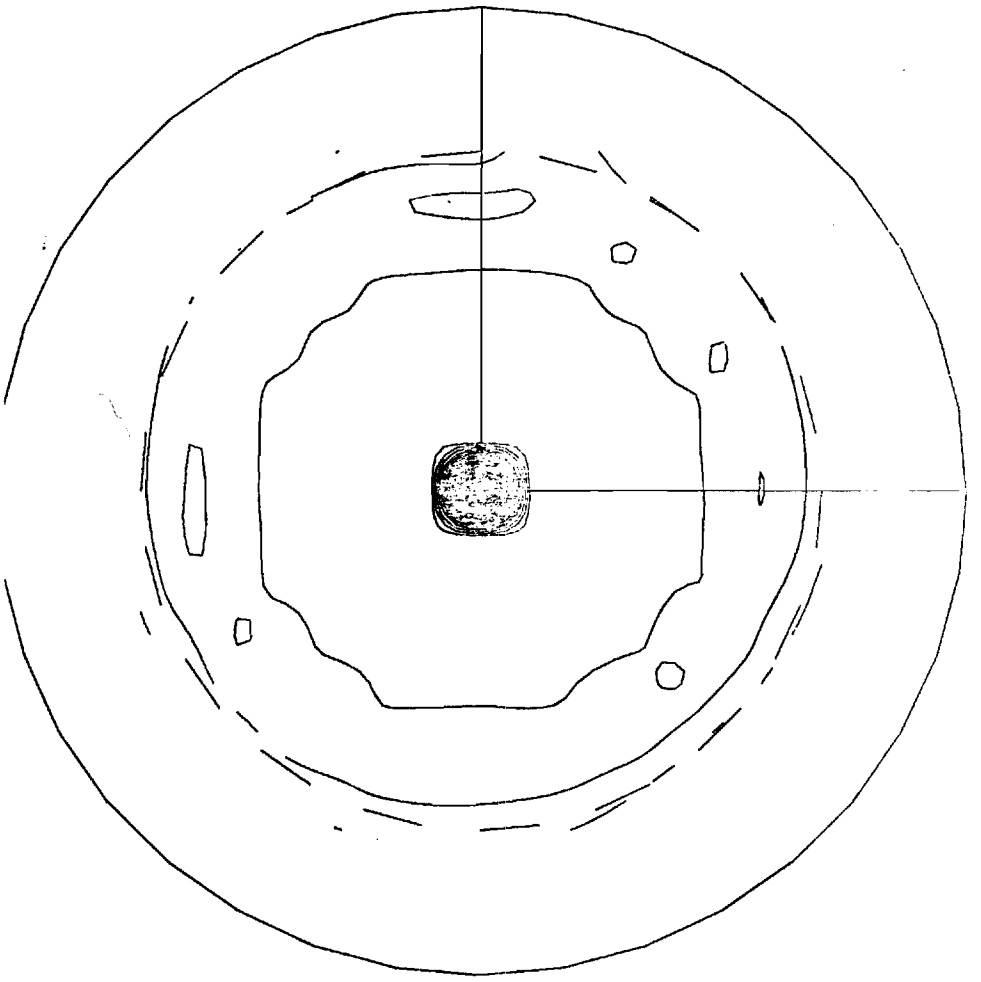

1752.268

1.2 A-10 20/1 (111) 29.312

.209

round .466"D

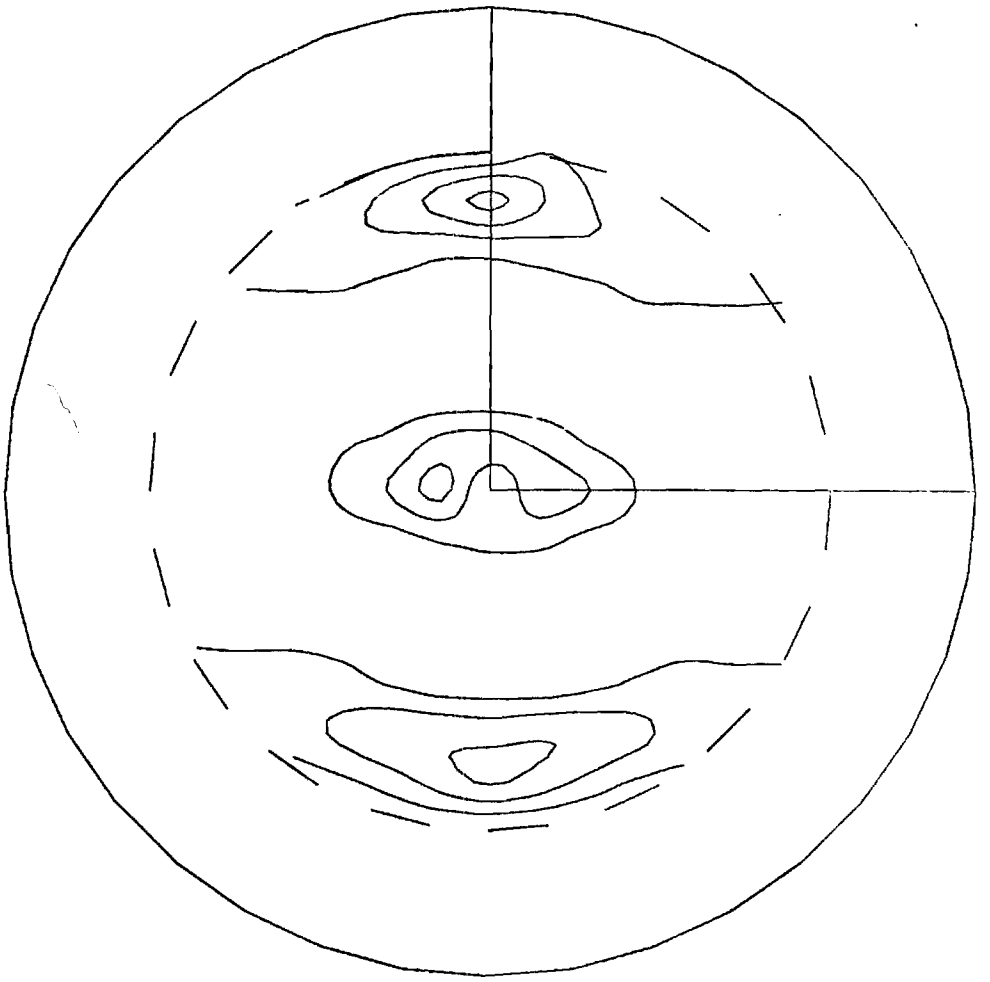

2179.259

1.2 A-11 10/1 (111) 4.736

.210

rect. 1.563 width
.214" thick

amp 7.3

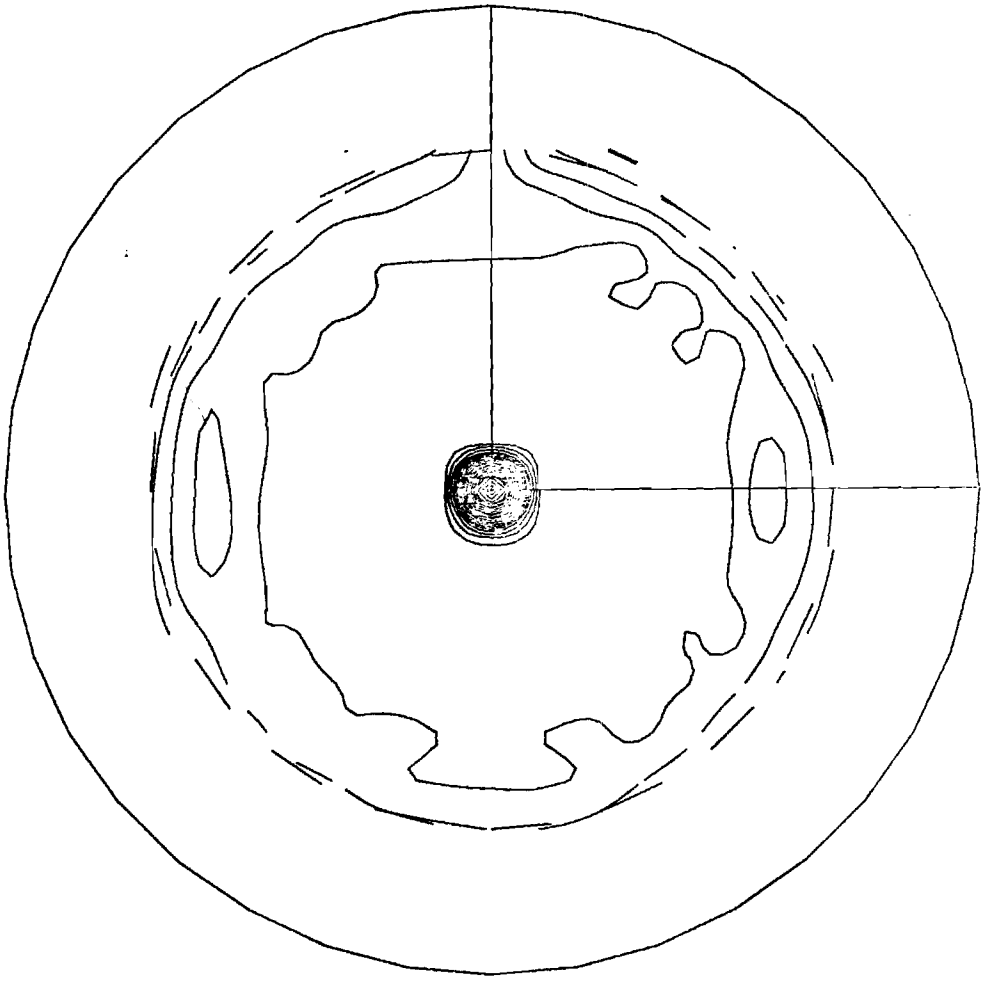

1938.842

1.2 A-12 (111) 25.103

.163

round . 461'D

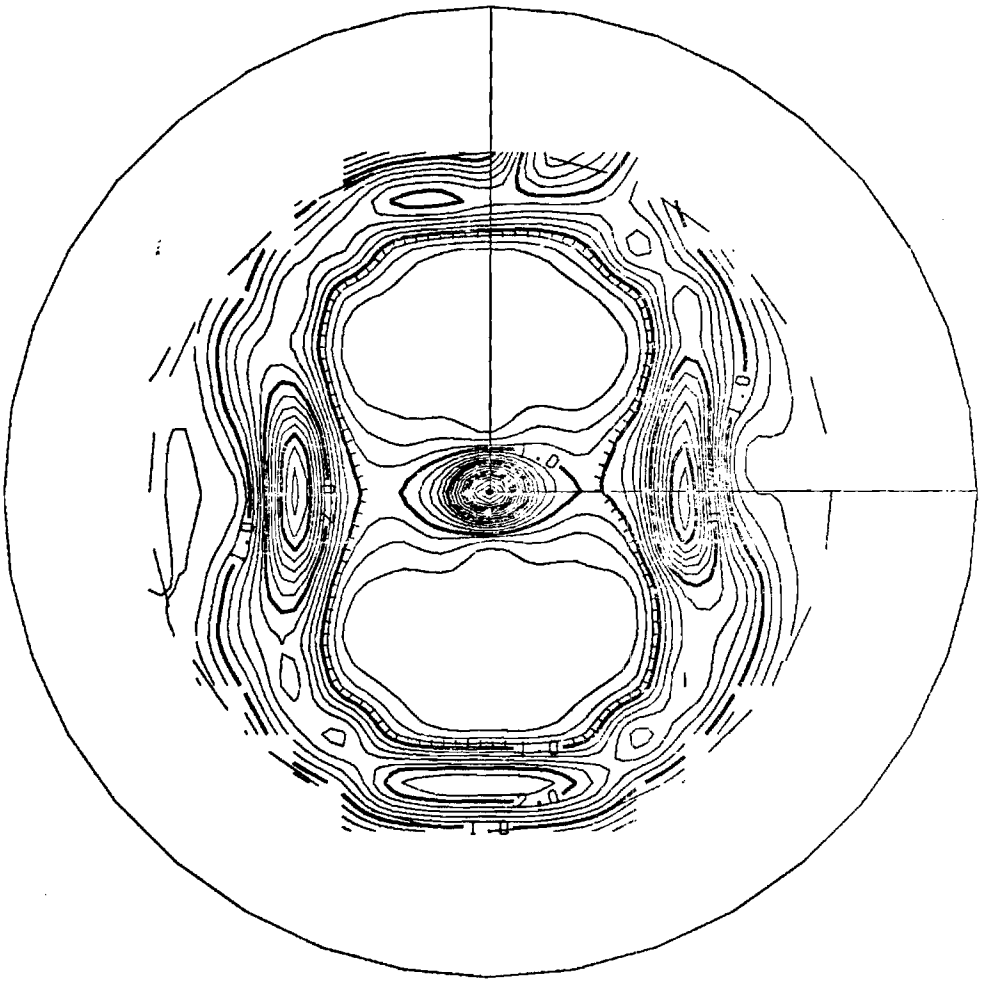

1093.410

1.2 A-1 8/1 (200) 4.175

.237

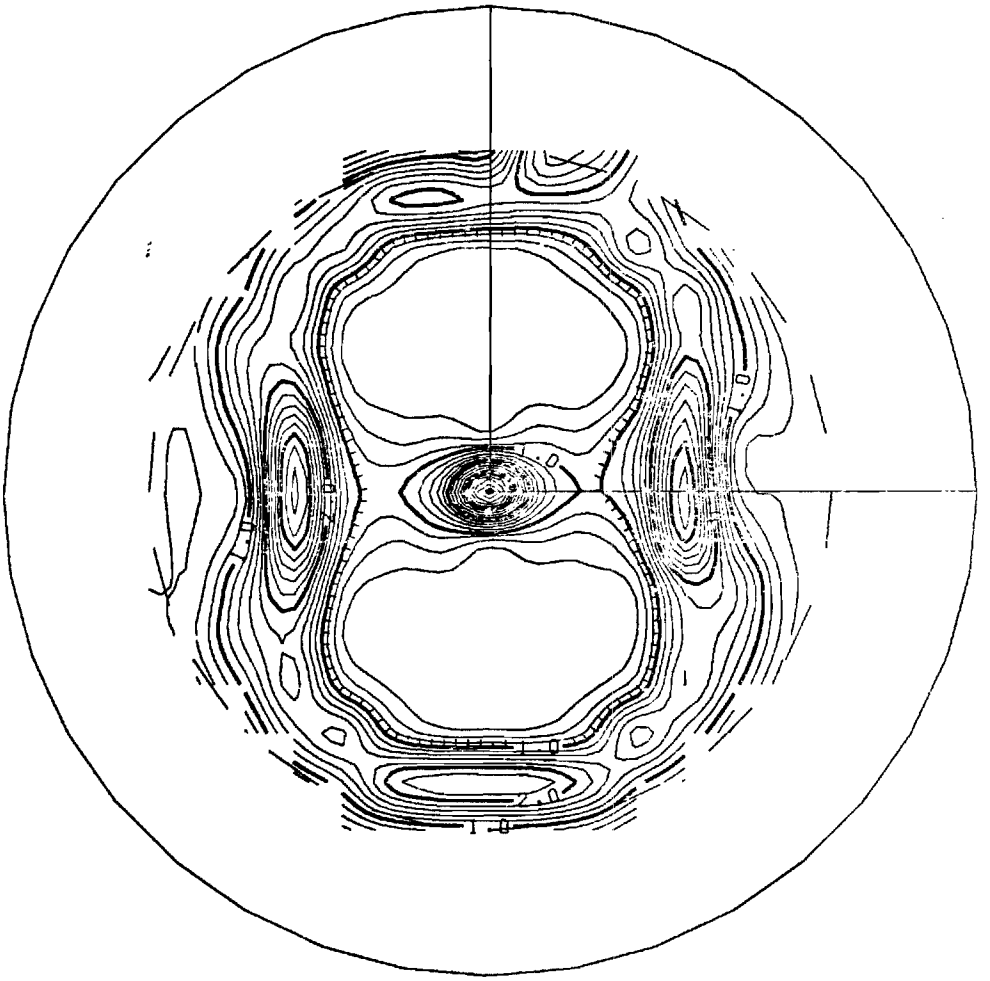

1093.410

1.2 A-1 8/1 (200) 4.175

.237

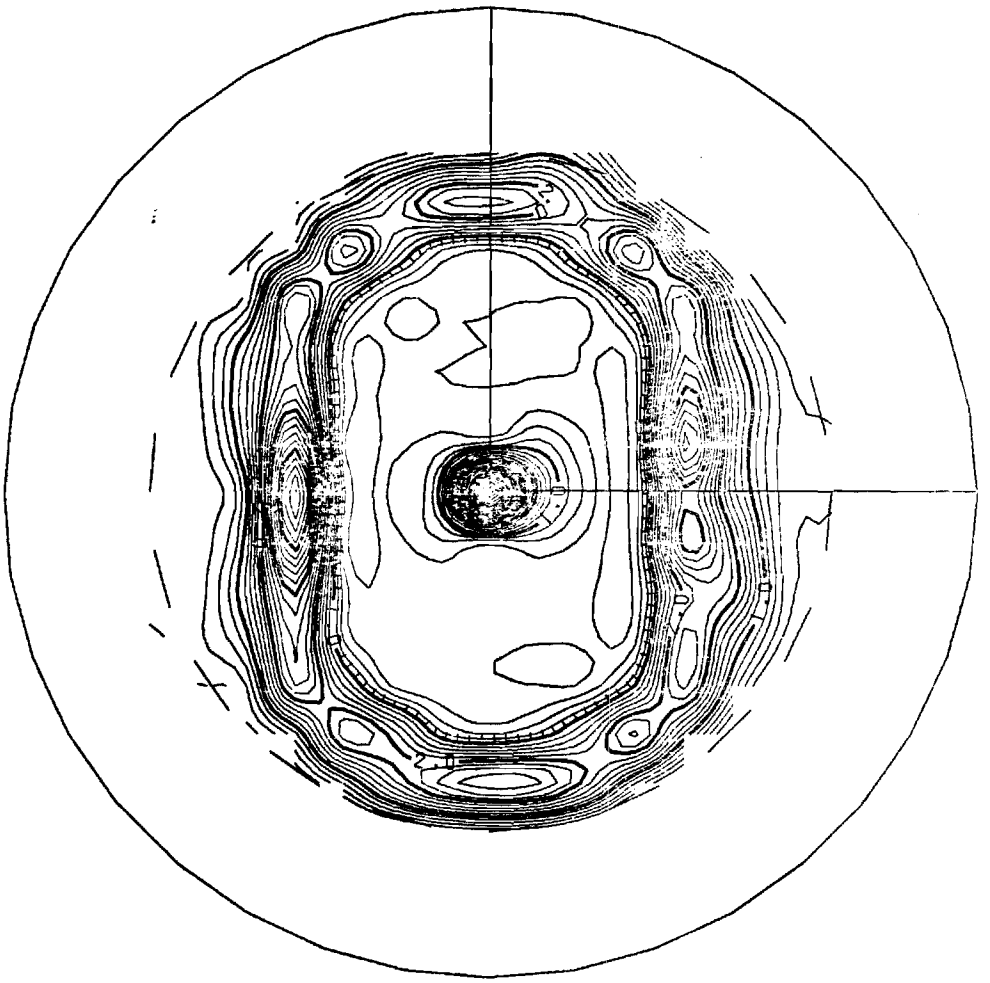

1026.168

1.2 A-5 (200) 6.025

.193

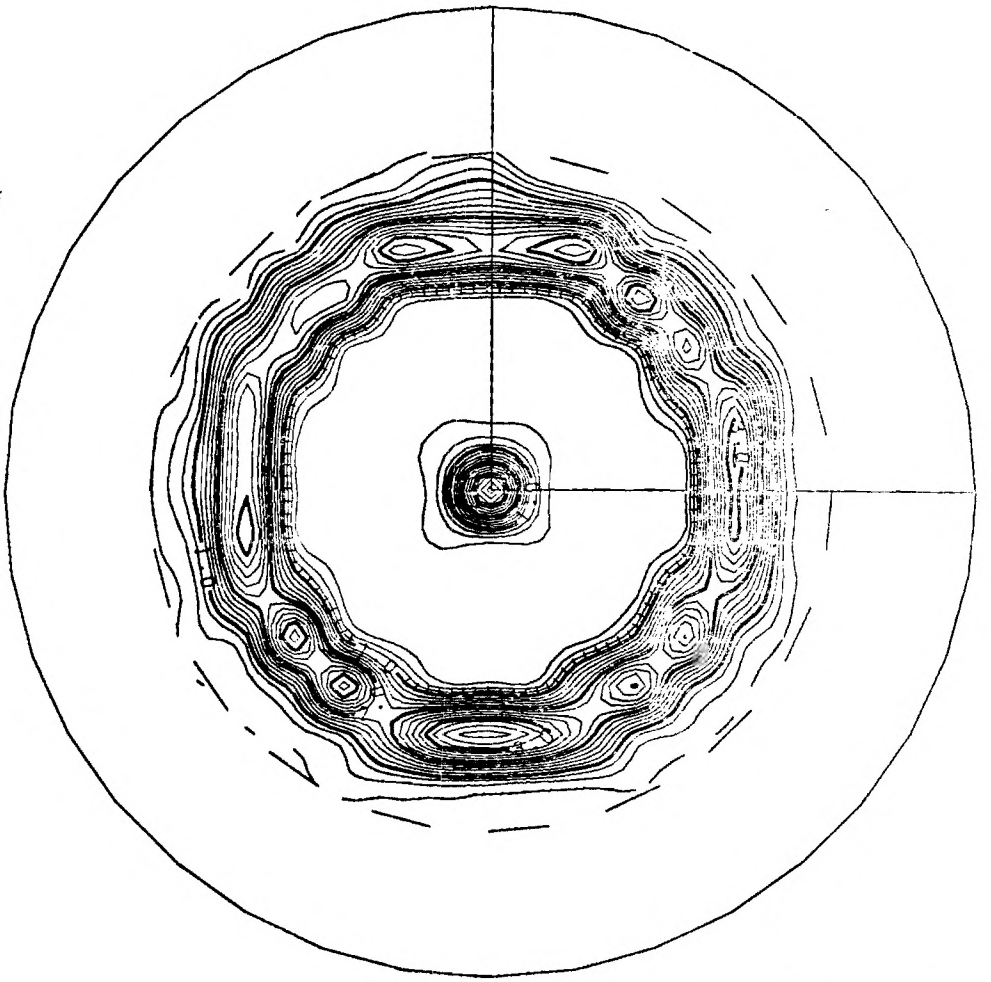

1004.571

1.2 A-10 20/1 (200) 4.121

.262

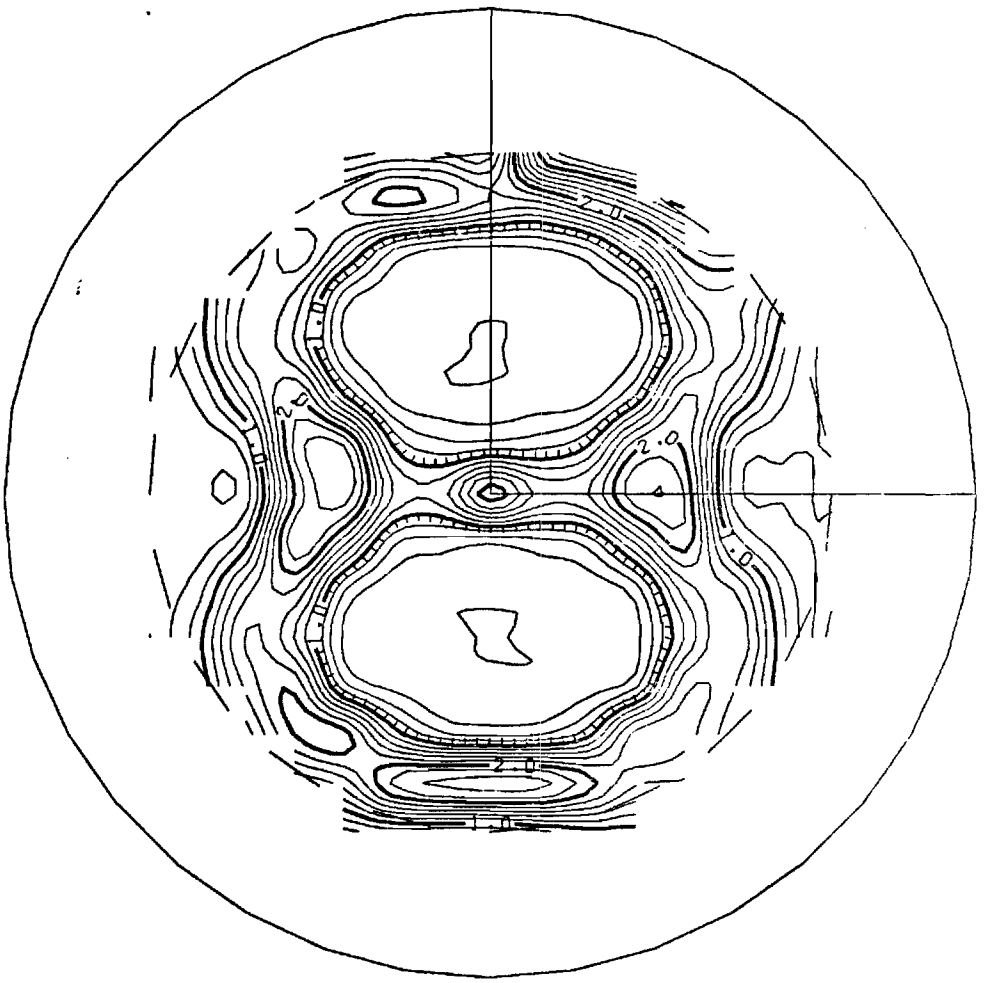

1180.462

1.2 A-11 10/1 (200) 3.420

.193

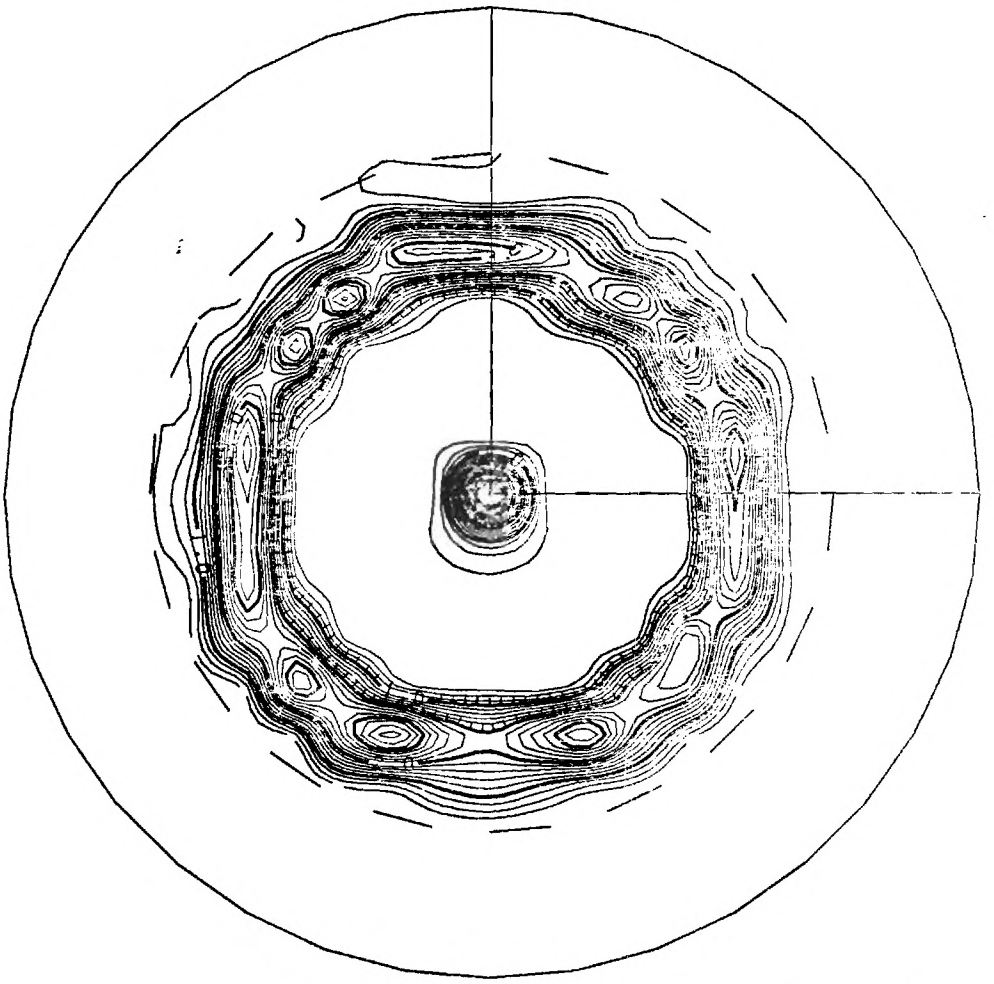

1218.882

1.2 A-12 20/1 (200) 5.889

.208

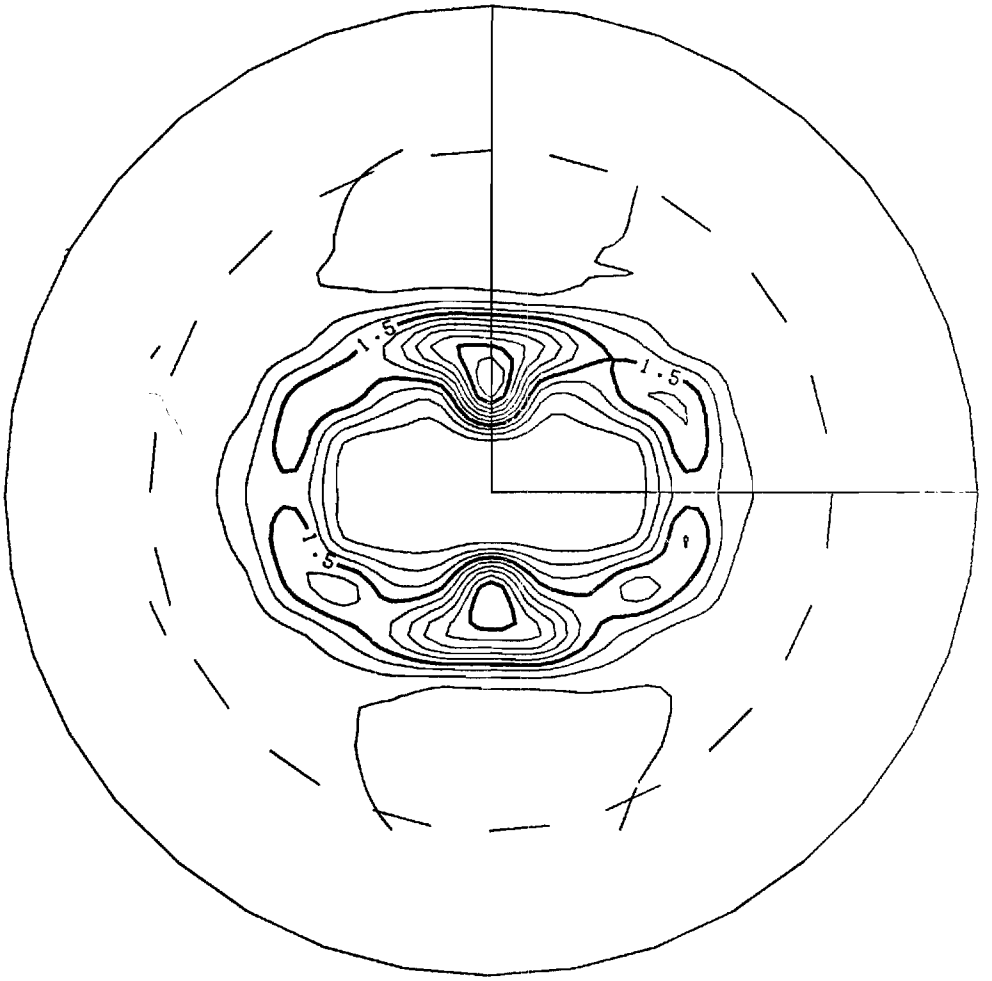

1.2 A-1 8/1 (220)

648.737
7.898
.332

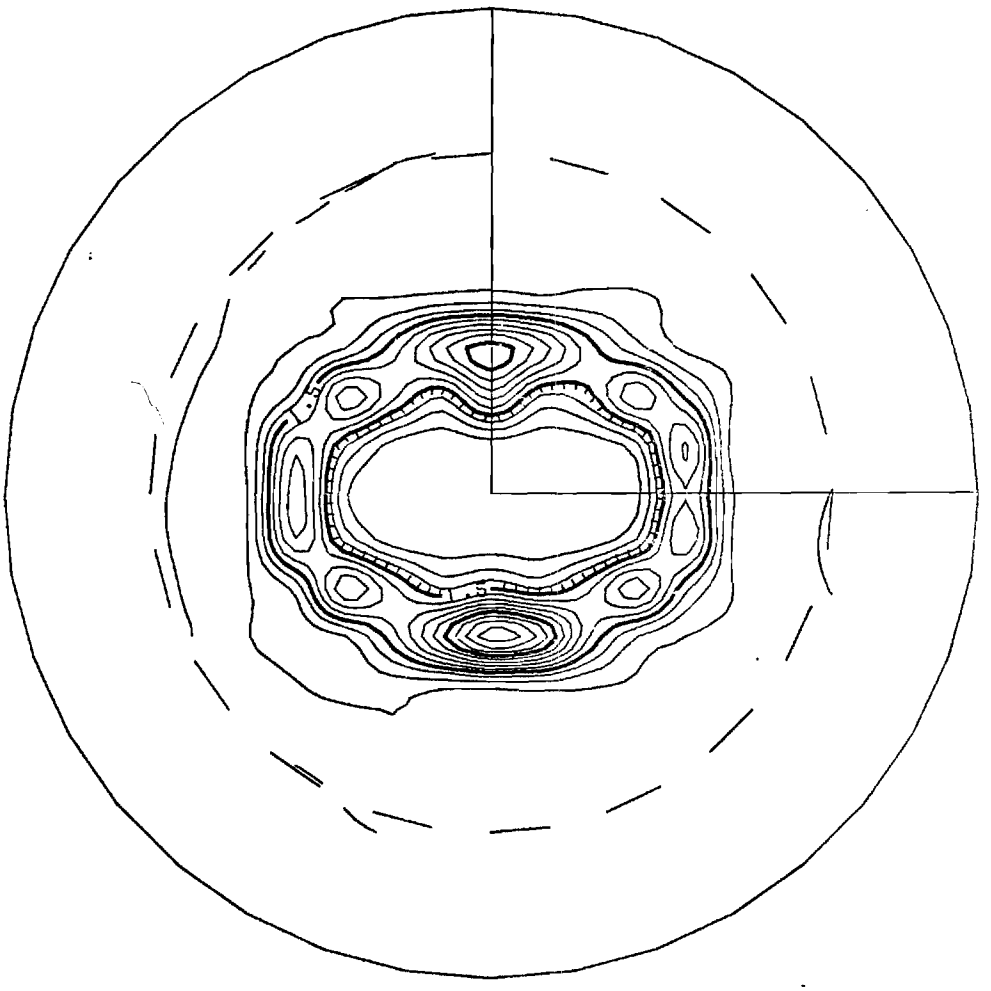

626.033

1.2 A-5 (220) 6.688

.360

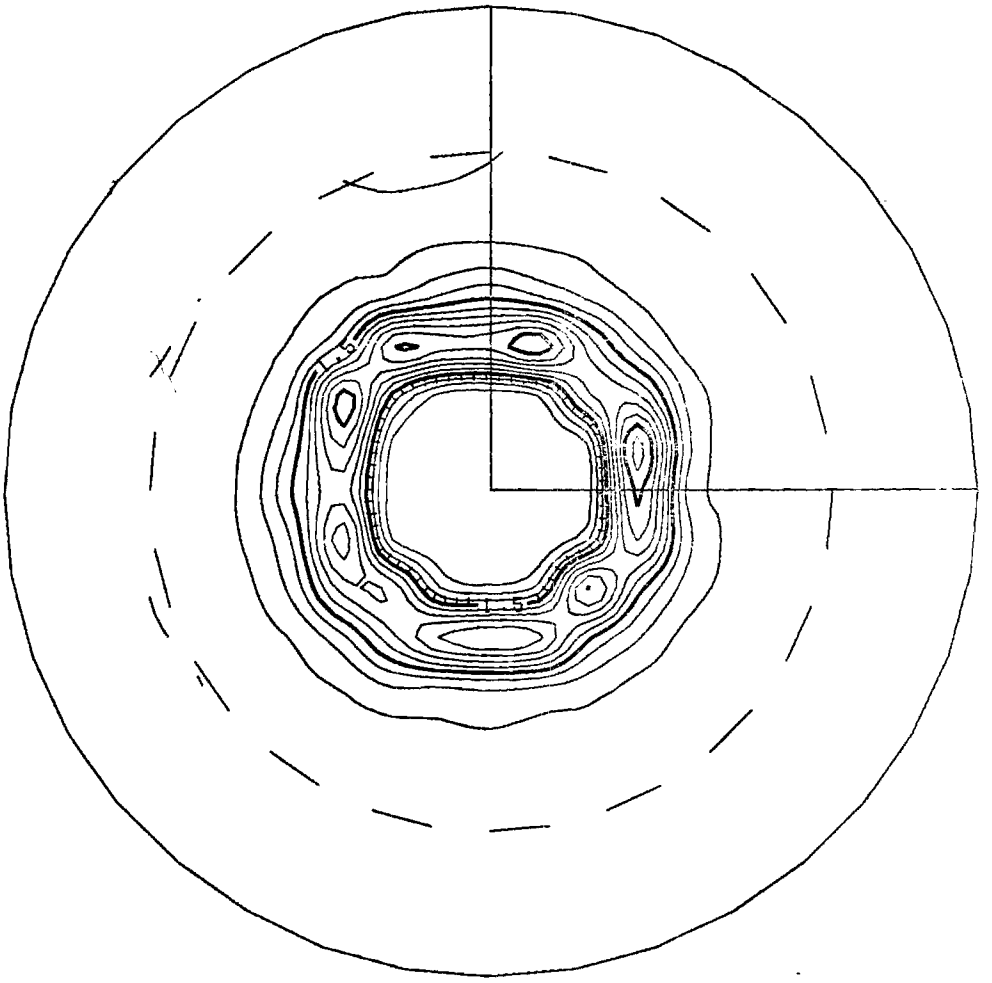

622.239

1.2 A-10 20/1 (220) 3.457

.328

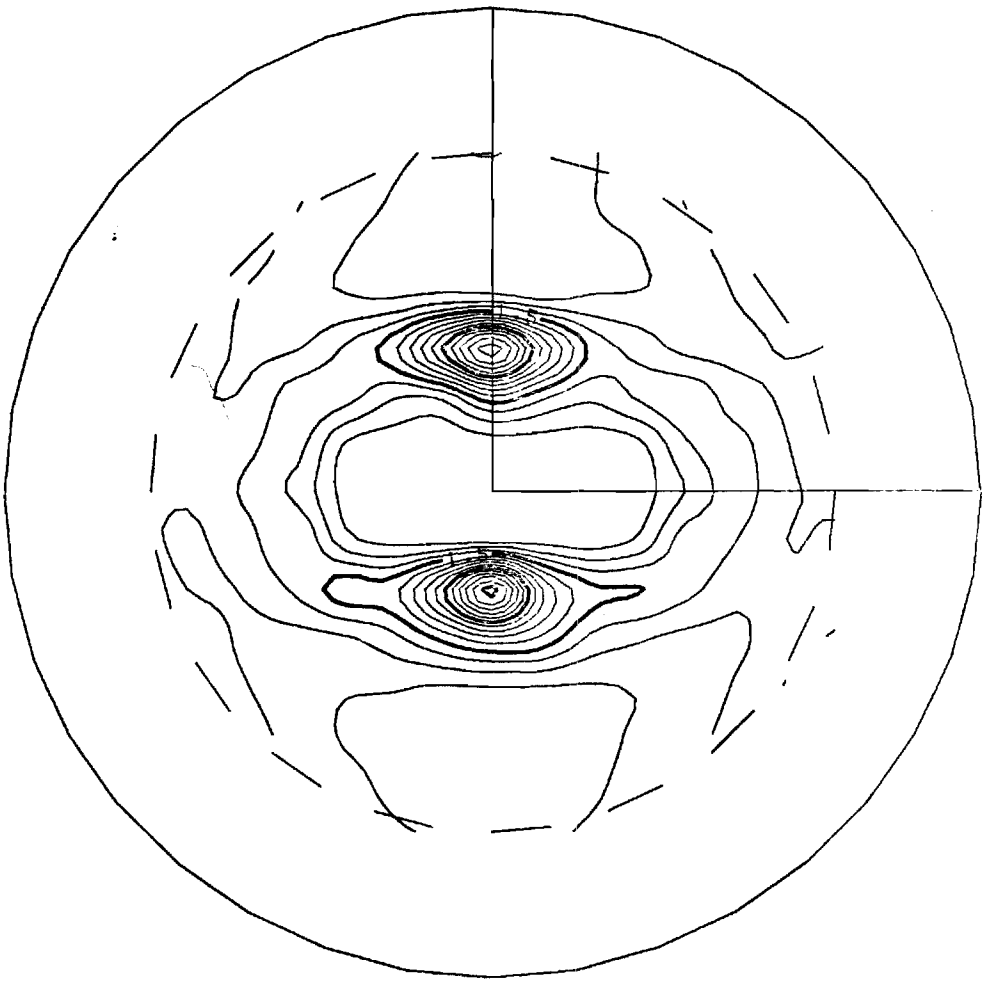

692.150

1.2 A-11 10/1 (220) 7.462

.363

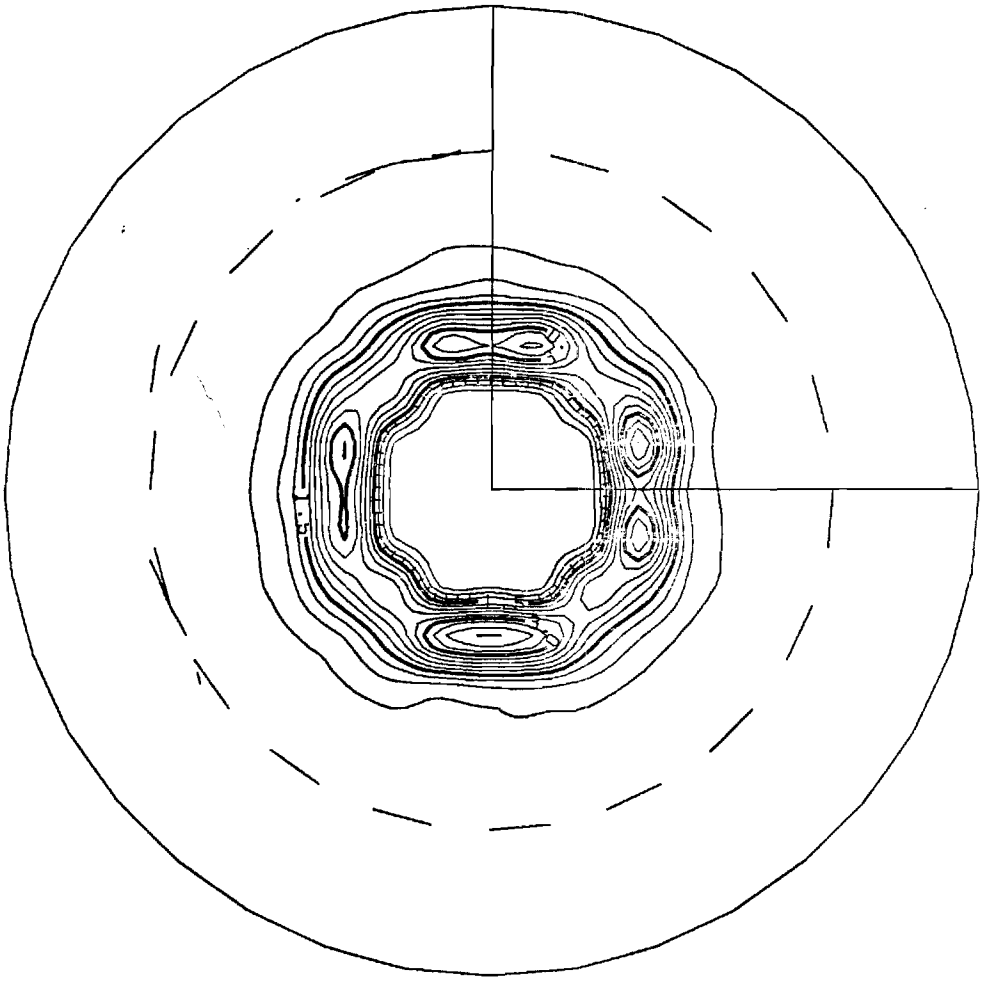

715.752

1.2 A-12 20/1 (220) 4.039

.334

GEORGIA INSTITUTE OF TECHNOLOGY

Contract Administration/Georgia Tech Research Institute

Atlanta, Georgia 30332

TELECOPIER: (404) 894-3120

(3M/4 MINUTE AUTOMATIC)

VERIFICATION: (404) 894-4850

TO: Dr. R. E. Lewis
Lockheed Missiles
CA

ADDRESSEE'S NO. x:45743

TELECOPIER NO. 415-493-4411 x:457~~55~~66

VERIFICATION NO. x:45548 ~~x:45544~~

FROM: E. A. Starke

CAMPUS EXT. 2880

DEPT.: Chem. Engg.

CHARGE NO. E-19-675

THIS TRANSMISSION CONSISTS OF 6 PAGES

(Excluding Leader Page)

OSA COMMUNICATIONS DESK

Date 9-15-80 Time 4:30 Operator KG

TRANSMITTED: ✓

TLX: ___

TWX: ___

Intl Cable: ___

Intl Ltr Letter: ___

Intl Telex: ___

Telegram: ___

FAX ✓

RETRIEVED: ___

Person notified: ___

Time: ___ Date: ___

NOTE:

xc: Starke

FRACTURE AND FATIGUE RESEARCH LABORATORY
GEORGIA INSTITUTE OF TECHNOLOGY

QUARTERLY REPORT
FOR PERIOD
5 June to 5 September 1980

FIRST INTERATION ALLOYS

The crystallographic textures have been determined for extrusions of alloy 1.2 (al-3Li-2Cu-0.2Zr) with different cross-section aspect ratios (width/thickness). Previously conducted tensile tests at LMSC resulted in significantly different yield stress values for these extrusions, ranging from 521 MPa for round axisymmetric extrusions to 414 MPa for sheet bar extrusions with an aspect ratio of 8:1 (see R&D Status Report for Period 5 March to 5 June 1980). The pole figures for (111), (220), and (200) lattice planes showed that the texture became more pronounced with decreasing extrusion aspect ratio, resulting in a very sharp fiber texture for round axisymmetric extrusions.

The pole figures of round extrusions indicate a maximum in the distribution of (111) lattice plane poles in a narrow angular region of about 10° centered around the extrusion axis. With increasing aspect ratio the intensity of (111) poles near the extrusion axis decreased and the angular distribution became wider. The large number of (111) lattice planes oriented nearly perpendicular to the extrusion axis in the case of axisymmetic extrusions might explain in a qualitative way the higher yield stress values observed in tensile tests with the loading axis parallel to the extrusion axis, because of the unfavorable orientation of the

(111) slip planes. These results are in accordance with those obtained on an Al-Zn-Mg-Cu (7475) alloy, which also showed that significant texture hardening can be obtained in Al alloys, despite the high symmetry of the FCC lattice [1].

RELATED PROGRAM ON 2020 ALLOYS

A comparison of microstructure and tensile properties has been made between I/M and P/M 2020 alloys (Al-4.45Cu-1.21Li-0.51Mn). The results obtained for the 2020 alloys will be used in the present program to serve as a comparison to those obtained for the second interation alloys. The P/M 2020 material was prepared from the I/M alloy by an Argon-atomization process. The atomized powder (-200 mesh) was cold compacted, vacuum degassed upon heating to 493°C and hot compacted. The billets were extruded to round rods with an extrusion ratio of 23:1.

Tensile properties of I/M and P/M 2020 for three different aging conditions are shown in Table 1. It should be noted that these results have been obtained from specimens without intermediate stress relief before aging. Yield stress values were found to be approximately similar for I/M and P/M material, while elongation to fracture values were slightly higher for the I/M specimens. However reduction in area values, which seem to be more suitable for comparison because of specimen necking, are higher for the P/M material. Metallographic studies showed the presence of a significant amount of spherical particles with sizes of up to 70 μm in the P/M material due to impurities introduced during the powder atomization process. SEM examination of fractured P/M 2020 tensile

specimens indicated that crack initiation occurred at these large particles. Tests are currently under way on P/M 2020 material with a reduced amount of these detrimental particles due to an improved atomization procedure. It is expected to increase the ductility of the P/M material by removing the large particles.

SECOND INTERATION ALLOYS

Preliminary tensile results have been obtained for two of the second interation alloys 1.11 (Al-3Cu-2Li) and 1.12 (Al-3Cu-2Li-0.2Zr). The heat treatment procedures previously applied for the first interation alloys have been adopted for alloys 1.11 and 1.12 to obtain preliminary tensile properties. The solution heat treatment was carried out at 538°C for 0.5 h, followed by cold water quenching and aging at 190°C for 0.75 h, 8 h, and 40 h. Some specimen blanks were also stretched 2% after SHT and then aged at 190°C for 8 h to study the response with regard to a thermal mechanical treatment. It will be noted that these aging treatments might not have resulted in optimum tensile properties. Age-hardening curves are currently established at LMSC for all four second interation alloys to select the proper aging treatments for under-, peak-, and over-aged conditions.

The results of the tensile tests are summarized for alloy 1.11 in Table 2 and for alloy 1.12 in Table 3. It can be seen that alloy 1.12 has superior yield stress and ultimate tensile stress values as compared to alloy 1.11. For example in the peak-aged condition alloy 1.12 showed a yield stress of about 463 MPa as compared to about 391 Mpa obtained for alloy 1.11. A 2% stretch before aging proved to be beneficial with regard to the yield stress as well

as the ultimate tensile stress. In the peak-aged condition the yield stress for alloy 1.12 increased from about 463 MPa without stretching to about 544 MPa with intermediate 2% stretching.

The elongation to fracture values of both second interation alloys are higher as compared to those obtained previously for all of the first interation alloys. Furthermore it should be noted that the intermediate stretching procedure, which resulted in higher yield stress as well as ultimate tensile stress values, did not adversely affect the elongation to fracture values (Tables 2 and 3). Transmission electron microscopy studies of thin foils and scanning electron microscopy investigations of the fracture surface have been initiated to characterize the microstructure and the fracture behavior respectively of these second interation alloys.

REFERENCE

1. K. Welpmann, A. Gysler and G. Lütjering, "Influence of Texture and degree of Recrystallization on the Mechanical Properties of an Al-Zn-Mg-Cu Alloy," to be published in Proc. 7th Intern. Conf. on Light Metals, Leoben, Austria, June 1981.

TABLE 1. TENSILE PROPERTIES OF I/M and P/M 2020

Alloy	Aging Treatment	$\sigma_{0.2}$ (MPa)	ε_f (%)	RA (%)
I/M	15 h 149°C	452	8.1	10.1
P/M		462	6.8	13.1
I/M	18 h 160°C	542	7.0	8.5
P/M		519	6.4	12.5
I/M	18 h 160°C	448	9.8	13.8
P/M	+15 min. 250°C	431	7.3	19.3

TABLE 2. TENSILE PROPERTIES OF ALLOY 1.11 (Al-3Cu-2Li)

Aging Condition	$\sigma_{0.2}$ (MPa)	UTS (MPa)	ε_f (%)
0.75 h 190°C	235	389	> 15*
	234	386	> 15*
8 h 190°C	390	460	10.6
	393	463	9.9
2% stretch	439	480	10.3
	444	485	10.3
40 h 190°C	378	436	9.3
	374	437	8.9

* Specimen elongation exceeded strain gage capacity

TABLE 3. TENSILE PROPERTIES OF ALLOY 1.12 (Al-3Cu-2Li-0.2Zr)

Aging Condition	$\sigma_{0.2}$ (MPa)	UTS (MPa)	ε_f (%)
0.75 h 190°C	351	503	12.0
	351	503	12.0
8 h 190°C	461	531	8.3
	466	537	8.3
2% stretch	541	567	7.4
	546	568	11.4
40 h 190°C	436	496	11.0
	438	495	6.4

FRACTURE AND FATIGUE RESEARCH LABORATORY
GEORGIA INSTITUTE OF TECHNOLOGY
ATLANTA, GEORGIA 30332

(404) 894-2880

October 6,1980

Metallographic examination of the longitudinal plane of Alloy 1.12 reveals some large-grain regions, which give the appearence of a partially recrystallized microstructure. However, the same inhomogeneities appear in the as-extruded temper (figure 1); suggesting the presence of large, unrecrystallized grains. The large grains correspond to large splat particles which are easily recognized in the cross section (figure 2). Most of the large particles are greater than 300μ in the longest direction (measured in the S-T plane, after processing). Additional screening of the splat particulate to remove the + 50 screen fraction would result in a more homogeneous microstructure.

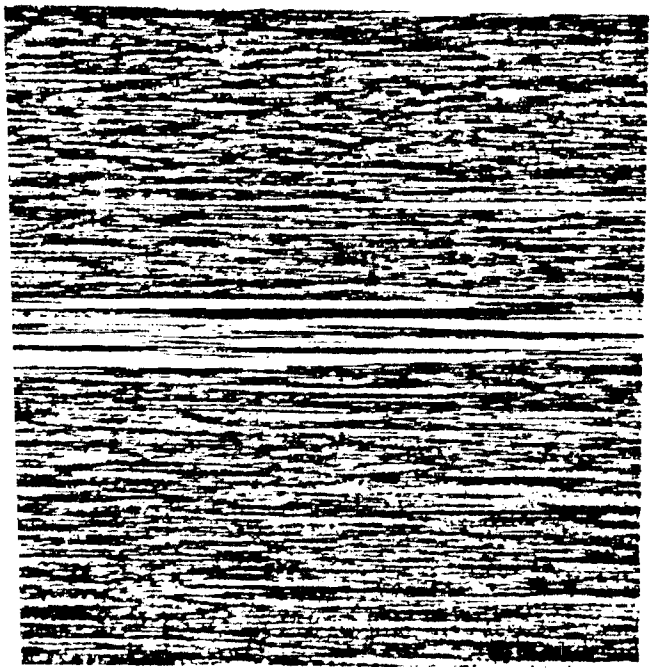

Figure 1. L-S plane,anodized, polarized light, 50 X

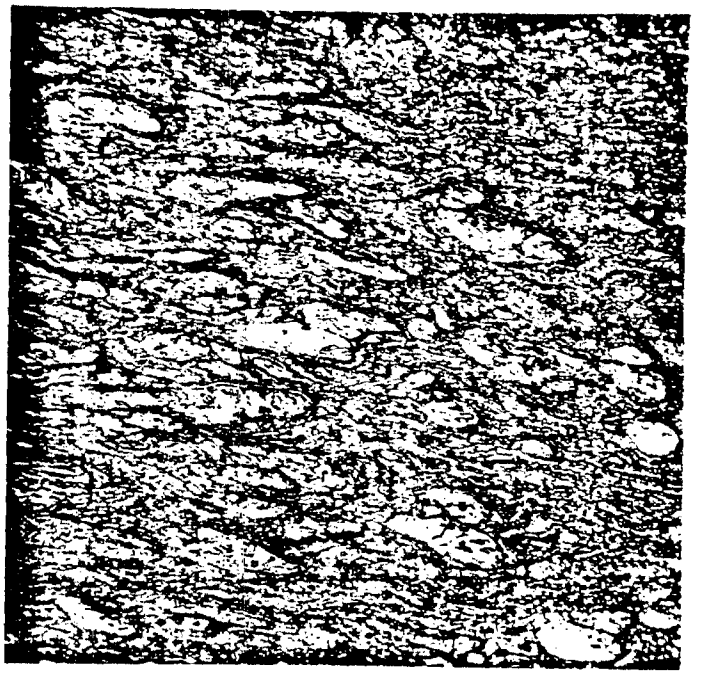

Figure 2. S-T plane,anodized, sensitive tint, 50 X

MONTHLY LETTER REPORT - TASK 3 - QUANTITATIVE MICROSTRUCTURAL ANALYSIS AND MECHANICAL PROPERTY CORRELATIONS

November 1980

Roy Crooks
E. A. Starke, Jr.
Fracture and Fatigue Research Laboratory
Georgia Institute of Technology
Atlanta, Georgia 30332

An investigation was begun to determine the optimum artificial aging conditions for Alloy 1.12. Melt analysis has shown the composition[1]:

Al-3 Cu-1.58 Li-0.79 Mg-0.16 Zr-0.04 Fe-0.04 Si-0.01 Zn-0.01 Ni

Al-Cu-Mg alloys exhibit an increase in yield strength when subjected to plastic deformation after solution-heat-treatment and before aging. This is due to an increase in the volume fraction of θ' precipitates, which nucleate at dislocations. Research at Alcoa has shown that a maximum increase in yield strength is obtained for the alloy 2124 after 4% cold rolling.[2] A similar increase in yield strength can be anticipated for Alloy 1.12.

Experimental Procedure

Flat tensile samples (ASTM standard sub-size) were stretched to approximately 2, 4, and 6% (plastic) after solution-heat-treatment for 0.5 hours at 538°C. Room temperature aging response was then determined from DPH measurements of the gage sections. DPH measurements were then taken after 1 hour and 24 hours at 190.6°C.

20 ASTM standard sub-size cylindrical tensile samples (gage length 16 mm, diameter 4 mm) were machined and solution-heat-treated for 0.5 hours at 538°C and ice-water-quenched. Ten were stretched to approximately 4% plastic elongation immediately after removal from the ice bath (with less than 15 minutes at room temperature during the stretching cycle). The samples were then room-temperature-aged 42.5 to 44 hours before artificial aging at 190.6°C.

Two samples of each were tested after 1, 4, 8, 16 and 24 hours on a MTS machined, monitoring load versus strain (with an X-Y recorder). The extensometer used had a limit of 4% strain, which required the test to be stopped (prior to the onset of plastic instability)to remove the gage. Stroke was then monitored to failure.

Results and Discussion

DPH values are plotted in Figure 1. Error bars represent ± s (standard deviation) for five measurements.

Tensile test results are given in Table 1 and plotted in Figures 2 and 3. Comparison of Figures 2 and 3 with Figure 4 (LMSC determination of R_B hardness versus aging time at 190.6°C) suggests that hardness curves can not be used for predicting the tensile strength aging response for this alloy.

Conclusions

The highest value of yield strength for 0% pre-strain was obtained after 16 hours aging time at 190.6°C. The highest value of yield strength for 4% pre-strain was obtained after 4 hours at 190.6°C. It may be beneficial to determine the peak aging time more accurately, with additional tensile tests; and, possibly, a lower aging temperature. Additional tensile tests should be run at different (i.e., higher and lower) amounts of pre-strain. This work is in progress. In addition, studies are now underway to determine the deformation structure and fracture mode of the stretched and unstretched material.

References

1. LMSC-D771068 Monthly Letter Report, 5 August 1980, p. 8.

2. Robinson, D. L., Unpublished Research, Alcoa Laboratories, referenced in Sanders, T. H., Jr., and Staley, J. T., "Review of Fatigue and Fracture Research on High Strength Aluminum Alloys" Fatigue and Microstructure, American Society for Metals, 1979, pp. 495-497.

Table 1

Tensile Test Results

Test	Pre-strain %	Aging Time hours	$\sigma_{0.2}$ MPa	ϵ_f %	ln A_o/A_f	R A %
A	0	1	331	18*	.261	22.9
B	0	1	326	18*	.268	23.5
E	0	4	417	14*	.330	28.1
F	0	4	406	14*	.304	26.2
I	0	8	453	14*	.372	31.1
J	0	8	460	13*	.376	31.3
M	0	16	475	8.8	.317	27.2
N	0	16	449	6.6	.111	10.5
Q	0	24	447	11	.305	26.3
R	0	24	462	8.5	.281	24.5
C	3.97	1	456	14*	.336	28.5
D	4.05	1	459	14*	.180	16.5
G	4.20	4	556	8.8	.406	33.3
H	4.06	4	562	7.4	.288	25.0
K	4.14	8	542	5.0	.177	16.2
L	4.12	8	558	7.2	.400	33.0
O	4.12	16	526	8.3	.411	33.7
P	4.08	16	527	8.5	.417	34.1
S	3.98	24	510	6.7	.284	24.7
T	3.96	24	525	9.3	.295	25.5

*These data are suspect. Cutting of the sample by the grips made the load readings erratic.

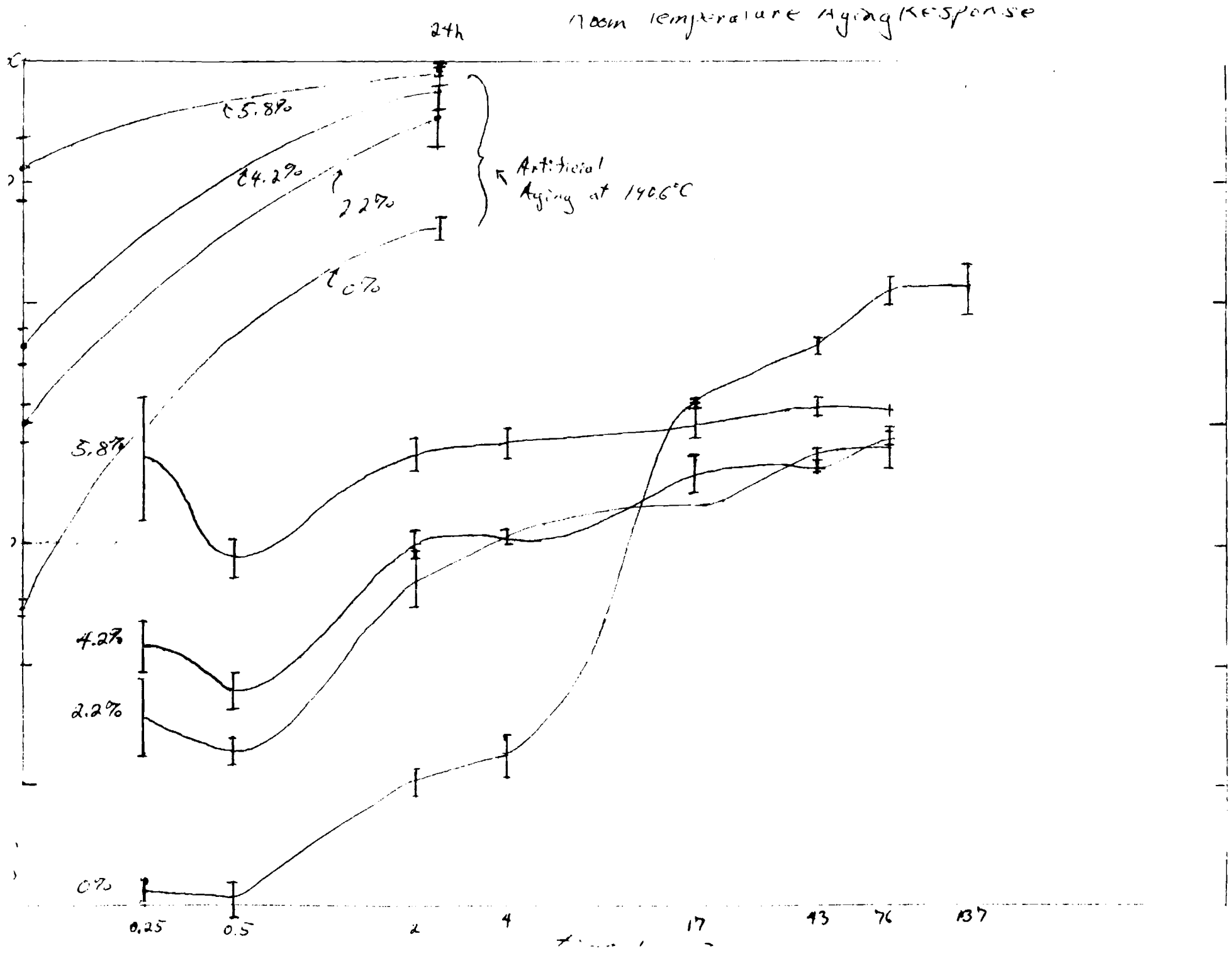
24h
Room temperature Aging Response
5.8%
4.2%
2.2%
0%
Artificial Aging at 140.6°C
5.8%
4.2%
2.2%
0%
0.25
0.5
2
4
17
43
76
137

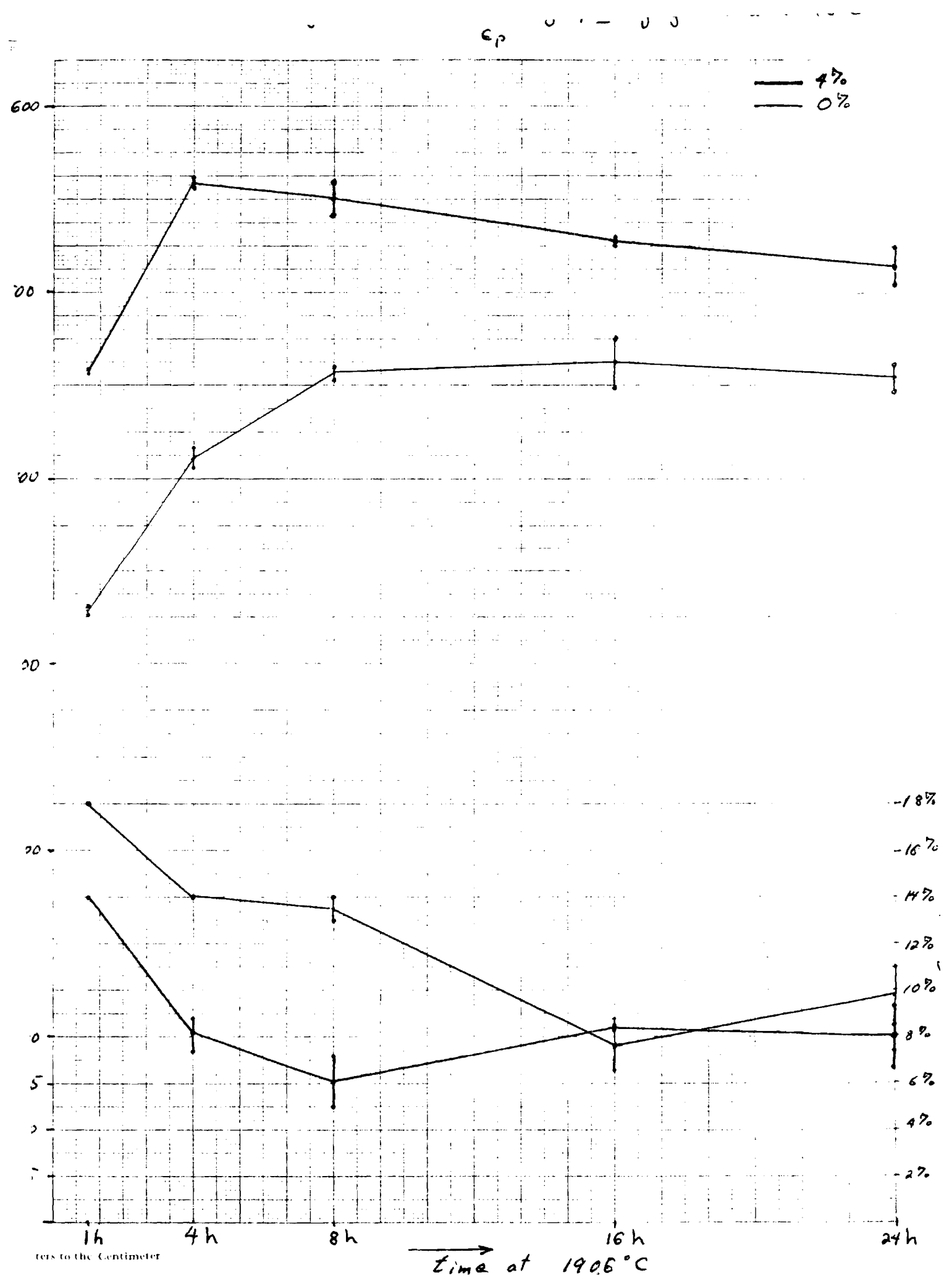

ters to the Centimeter

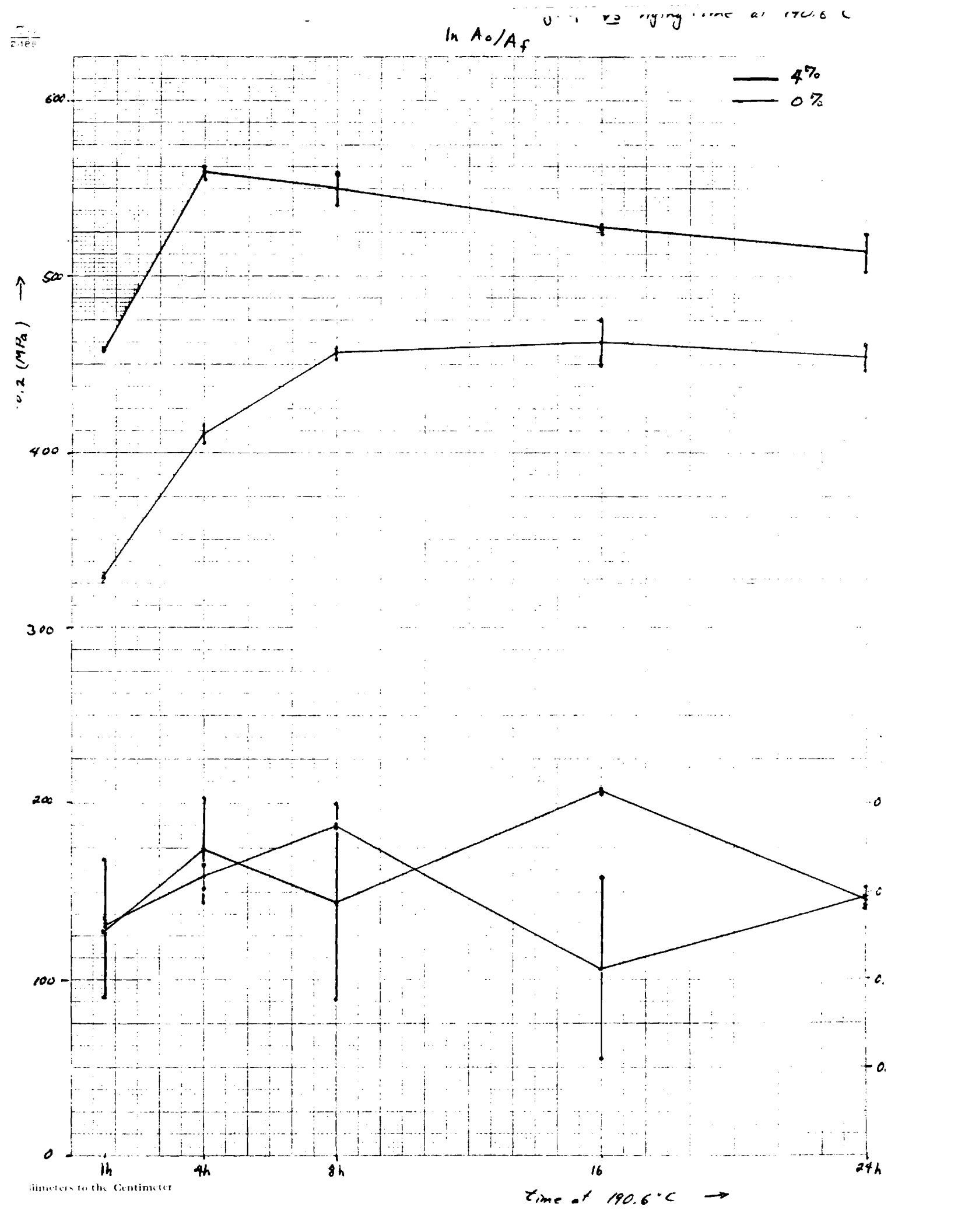

limeters to the Centimeter

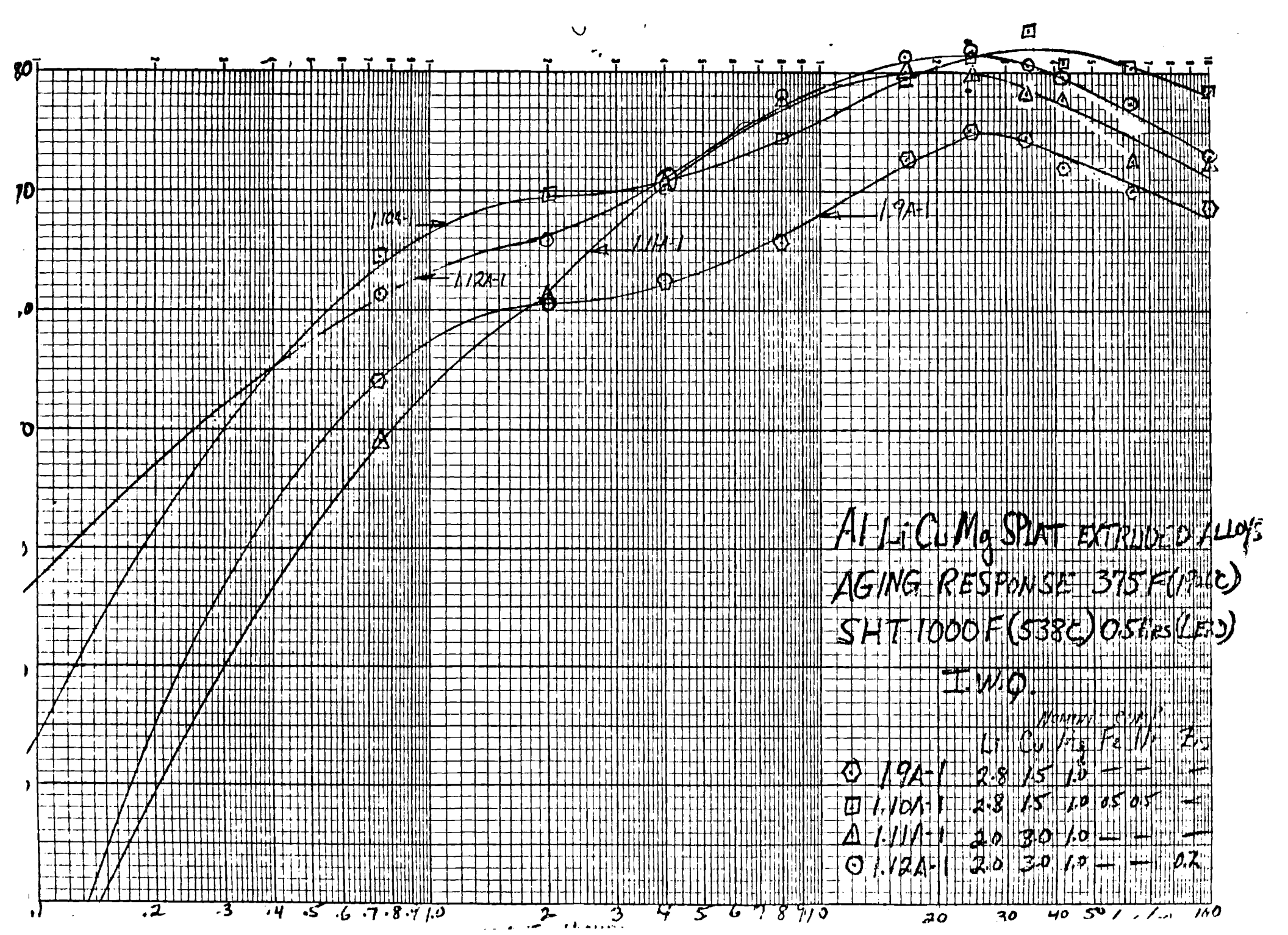
80
70
60
50
40
30
20
10
0
1.10A-1
1.12A-1
1.11A-1
1.9A-1
.1
.2
.3
.4
.5
.6
.7
.8
.9
1.0
2
3
4
5
6
7
8
9
10
20
30
40
50
100
Al Li Cu Mg SPLAT EXTRUDED ALLOYS
AGING RESPONSE 375 F (191 C)
SHT 1000 F (538 C) 0.5 HRS (LEG)
T.W.O.
Nominal Comp. %
Li Cu Mg Fe Mn Zr
1.9A-1 2.8 1.5 1.0 — — —
1.10A-1 2.8 1.5 1.0 0.5 0.5 —
1.11A-1 2.0 3.0 1.0 — — —
1.12A-1 2.0 3.0 1.0 — — 0.2

E-19-675

DARPA
Monthly Report
5 March - 5 April 1981

A Ph.D. thesis proposal was prepared during this report period. The proposed research will continue the development work on Alloy 1.12. The topic of the research is "The Influence of Microstructure on the Ductility of an Al-Cu-Li-Mg-Zr Alloy," The microstructure and peak-strength-ductility of Alloy 1.12 (nominally Al-3Cu-2Li-1Mg-0.2Zr) will be compared after production by splat quenching, inert gas atomization and conventional, ingot production methods, and the appropriate heat treatments. A copy of the proposal is enclosed.

THE INFLUENCE OF MICROSTRUCTURE ON THE DUCTILITY OF AN Al-Cu-Li-Mg-Zr ALLOY

Roy Edmond Crooks
Ph.D. Thesis Proposal
April, 1981

SUMMARY

The alloy Al-3Cu-2Li-1Mg-0.2Zr will be studied after production by conventional ingot methods, inert gas atomization, and splat quenching. Rapid solidification results in a smaller grain size and a finer, more homogeneous distribution of intermetallic particles. Modification of the precipitate size and distribution will be effected by final thermal mechanical treatment and artificial aging. Grain size and morphology, intermetallic particle size and distribution, and precipitate size and distribution are important parameters affecting the ductility of aluminum alloys. Variation of these parameters should allow conclusions to be drawn concerning the influence of the microstructure on the ductility of this alloy.

INTRODUCTION

The two major high-strength aluminum alloy systems currently in use for aerospace applications are of the Al-Cu type (Aluminum Association designation 2XXX series) and the Al-Zn-Mg-Cu type (Aluminum Association designation 7XXX series). The majority of alloy development efforts have been concerned with improving strength, corrosion properties, fatigue resistance and fracture toughness through modifications of the alloy chemistry and microstructure.

There is a great demand in aerospace design for aluminum alloys which offer an increase in specific strength (σ/ρ) or specific stiffness (E/ρ). Major improvements in the strength levels of conventional aluminum alloys appear to be limited by a reduction in secondary properties. A significant increase in stiffness can be obtained by the development of a large volume fraction of a finely despersed second phase. In the Al-Li system, a metastable, Al_3Li phase can precipitate in large volume fractions; resulting in a high elastic modulus. A significant amount of the elastic modulus increase observed in Al-Li alloys is attributed to a solid solution effect which results in a modulus increase before precipitation occurs, and at lithium levels below the saturation limit.[66] Lithium additions also reduce the density of the alloy, thereby increasing the specific stiffness. Aluminum-lithium alloys have been shown to have the advantages of high strenth, high modulus, low density, and excellent fatigue crack growth and corrosion resistance. The major barrier to the succussful industrial utilization of alloys in the Al-Li system has been the lack of adequate fracture toughness and ductility at peak strength. Large increases in the

solidification rate can cause a reduction in both the grain size and constituent particle size, and should have a beneficial effect on ductility and fracture toughness.

A research program has been underway at LMSC and Ga. Tech to assess the effect of rapid solidification processing on the mechanical properties of various Al-Li alloys. The most promising alloy, with regard to peak strength and ductility, was chosen for this study. The nominal composition of the alloy is:

Al - 3 wt % Cu - 2 wt % Li - 1 wt % Mg - 0.2 wt % Zr

Copper additions to aluminum alloys promote homogeneous deformation and increase strength. Magnesium also contributes to the strength by reducing the solubility of lithium in the matrix, which enhances precipitation, and by adding a solid solution strengthening effect. Zirconium was added to this alloy to inhibit recrystallization.

Comparisons will be made between batches produced by splat quenching, argon atomizing, and ingot production methods.

The objective of the proposed research is to determine the influence of various microstructural parameters on the ductility of this alloy.

LITERATURE REVIEW

The mechanical properties of aluminum alloys are strongly influenced by the nature of the second phase particles. These particles have been classified into three groups[1]:

1. Precipitate particles, which generally range in size from 0.01 to 0.5 μm, and are used to strengthen the matrix.
2. Dispersoid particles, 0.05 to 0.5 μm in size, used to inhibit recrystallization and grain growth; usually rich in Cr, Mn or Zr.
3. Constituent particles, which may range from 1 to greater than 10μm in size. These particles are rich in Fe, Si or Cu, and are formed during casting. In high strength aluminum alloys, Fe and Si are present as impurities, while Cu is a deliberate addition.

Age hardening alloys derive their increase in strength over that of a solid solution alloy from the interaction of dislocations with precipitates which form during aging.[2] The strengthening mechanism depends on the particle size, type and distribution. If the precipitates are coherent or partially coherent with the matrix, they may be sheared by dislocations during deformation. The critical resolved shear stress due to this interaction can be described by:

$$\tau = c\, f^{m}\, r^{\rho}$$

where c is an alloy constant representing coherency, interface, chemical, stacking fault and modulus hardening effects[3], f represents the volume fraction, r is the particle radius, and m and ρ are positive. For precipitate shearing mechanisms, the strength increases with both volume fraction and particle size. As the particles increase in size, the increase

in coherency strains may be relieved by the loss of particle coherency. Dislocations can loop incoherent particles by a mechanism referred to as Orowan hardening[4], with a resultant critical resolved shear stress[5]:

$$\tau = \frac{0.8\ G\ b\ \sqrt{f}}{2\ \pi\ \{2\ (1-\nu)r\}^{1/2}}\ \ln\frac{1.6}{r_o}\ r$$

where G is the shear modulus; b,the Burgers vector; ν, Poisson's ratio, and r_o is the inner cutoff radius of the dislocation. For dislocation looping, the strength decreases with increasing particle size.

Precipitation Sequences

The Al-Cu-Li-Mg-Zr alloy chosen for this research has not been studied before, and it is convenient, here, to consider the precipitation sequences of similar alloy systems, in order to estimate which precipitation reactions may occur in this alloy.

Al-Cu

The precipitation sequence in aluminum-copper alloys is considered the classical example of age hardening. The free energy barrier to the formation of the equilibrium phase is circumvented by a series of intermediate phases with successively greater lattice misfit[6]. The decomposition process may be represented as:

Supersaturated Solid Solution (SSSS) → G.P. zones → θ'' → θ' → θ

Guinier-Preston (G.P.) zones are fully coherent, solute-rich clusters which were first detected independently and reported simultaneously by

Guinier[7] and Preston[8]. A widely accepted model for G.P. zones in Al-Cu, proposed by Gerold[9] describes a single plane of copper atoms on $\{100\}_\alpha$, with a surrounding strain field. G.P. zones nucleate homogeneously, but θ'' probably nucleates heterogeneously at the G.P. zone : matrix interface.[10] The major strengthening precipitate of Al-Cu binary alloys, θ' (Al_2Cu), has a large misfit in one direction and always nucleates heterogeneously at dislocations. The equilibrium phase, θ, is nucleated at planar interfaces, such as grain boundaries or θ' : matrix interfaces.

Al-Cu-Mg

Al-Cu-Mg alloys with a Cu : Mg weight ratio of 2.2 : 1 form a pseudo-binary Al-AlCuMg system. The precipitation sequence is:

$$SSSS \rightarrow \text{G.P. zones} \rightarrow S' \rightarrow S\ (Al_2CuMg)$$

The pseudo-binary alloy was compared to an alloy with a Cu : Mg weight ratio of 7 : 1 by Silcock[11]. G.P. zones in the higher copper alloy were a mixture of the flat discs characteristic of the Al-Cu binary alloys, and the cylindrical G.P. zones found in the pseudo-binary system. The S' phase occurs as rods with an orthorhombic crystal structure, with three specific orientations relative to the matrix:

$$[100]_{S'} \,||\, [100]_\alpha,\ [010]_{S'} \,||\, [021]_\alpha,\ [001]_{S'} \,||\, [012]_\alpha$$

The S' phase nucleates heterogeneously on dislocations. The equilibrium phase, S, has the same orientation relationship and similar lattice parameters to the S' phase, and forms by the coherency loss of S'.[12,13,14]

Al-Li

The precipitation sequence for Al-Li binary alloys has been shown

to be:

$$SSSS \rightarrow \delta' \rightarrow \delta$$

The metastable, Al_3Li, δ' phase has an $L1_2$ structure. This can be considered as a face centered cubic structure with Al at the faces and Li at corner sites. The metastable precipitate is coherent with the matrix, and forms spheres with a cube/cube,precipitate/matrix orientation. Coherent, spherical particles require a low lattice misfit, and Noble and Thompson have measured a misfit of - 0.18% [15]. The precipitate : matrix interfacial energy has been determined to be 0.18 j/m^2. This is much lower than the value determined for θ', which is 1.5 j/m^2. [16] A low interfacial energy promotes homogeneous nucleation, which is observed for δ' precipitation.

Al-Cu-Li

Al-Cu-Li alloys follow the precipitation sequence:

$$SSSS \rightarrow \begin{cases} \text{G.P. zones} \rightarrow \theta'' \rightarrow \theta' \rightarrow \theta \\ \qquad\qquad\qquad\qquad\quad \rightarrow T_1 \\ \delta' \rightarrow \delta \end{cases}$$

Copper and lithium precipitate according to the sequences established for the binary alloys.[18] Under certain conditions of aging and for some alloy compositions, ternary precipitates, such as the equilibrium Al_2CuLi phase, T_1, may be present.[19]

Al-Mg-Li

The aging sequence for Al-Mg-Li alloys has been shown to be:[20]

$$SSSS \rightarrow \delta' \rightarrow Al_2MgLi$$

Thompson and Noble reported that additions of magnesium up to 2 wt% Mg

had little effect on the size and distribution of δ' particles, and that the equilibrium phase, Al_2MgLi, was not observed for additions of 2 wt% Mg, or less.[20]

Al-Zr

Zirconium is added to aluminum alloys to inhibit recrystallization. Al_3Zr precipitates, like Al_3Li (δ') metastable precipitates, have a cube/cube relationship with the matrix, and an $L1_2$ crystal structure. Al_3Zr forms at relatively high temperatures (approximately 500 °C), by the sequence:[21]

$$SSSS \rightarrow Al_3Zr$$

When a grain boundary migrates during recrystallization, and changes the orientation of the matrix, an incoherent interface develops at the Al_3Zr precipitate. This results in an additional component of drag on the grain boundary, proportional to the misorientation.[22,23]

Lithium may act to produce a higher volume fraction of Al_3Zr, by decreasing its solubility in the matrix, or by substituting for zirconium. Possibly because of these effects, a small amount of zirconium is effective in preventing the recrystallization of Al-Li alloys.[23]

Deformation Mechanisms

Dislocation shearing of a coherent, strengthening precipitate causes a reduction in the effective diameter of that particle, and promotes a localized, planar mode of slip. Shearing of ordered particles requires the movement of pairs of dislocations of the same type separated by an antiphase boundary.[24] This effect has been observed in Al-Li binary alloys,[25] and is termed superlattice dislocation movement. For constant volume

deformation, five independent slip systems must be available, and this condition is satisfied in face-centered-cubic lattices. Cross slip of superlattice dislocations results in pairs of sessile dislocations which impede further deformation and cause a high work hardening rate. These factors combine to create high stress concentrations and fracture along subgrain boundaries.[18]

For many age hardening aluminum alloys, precipitate free zones (PFZ's) develop at grain boundaries and intermetallic particle interfaces. To understand the effect of PFZ's on deformation, it is important, first, to consider their origin.

PFZ Formation

Typically,a precipitation hardenable alloy is subjected to a high temperature solution heat treatment, and subsequently quenched and aged. The purpose of the solution heat treatment is to distribute the solute in a homogeneous solid solution. The quench serves to delay the segregation of solute atoms during cooling, and to capture vacancies. The equilibrium vacancy concentration can be expressed as:

$$c_v = \exp(-\frac{E}{kT})$$

where E is the energy of formation of one vacancy, and k is Boltzmann's constant. The mobility of vacancies decreases exponentially with decreasing temperature, and therefore, the rate of quenching affects the vacancy concentration[26].

The precursors of the intermediate precipitate phases are referred to as G.P. zones. G.P. zones form during aging below a critical temperature, T_c [27]. In the presence of an excess vacancy concentration, G.P.

zone formation is possible[2] above T_c, up to a maximum temperature T_c'. Since grain boundaries act as sinks or conductorsfor vacancies, an excess vacancy concentration gradient is established in the vicinity of the boundary[28]. As a consequence,formation of G.P. zones is prohibited above T_c within a certain distance of the grain boundary, dependent upon the temperature and the vacancy concentration. Below T_c, G.P. zone formation does not require excess vacancies, but G.P. zones near the boundary will not grow as rapidly as the others, since the solute diffusion rate depends on the vacancy concentration[29]. If aging is continued at a higher temperature, G.P. zones which are larger than a critical size develop into intermediate precipitates, and those which are smaller, re-dissolve[2]. The region near a grain boundary where precipitates are not observed is referred to as a precipitate free zone or PFZ. PFZ's may also form at boundaries due to the preferential segregation of solute to the boundaries during cooling, or to heterogeneous precipitation at the grain boundaries.

The Influence of PFZ's on Ductility

The relationship between deformation and PFZ's has been the subject of much speculation. Geisler first suggested that the regions adjacent to grain boundaries in precipitation hardened alloys would be preferred areas for plastic flow[30]. Thomas and Nutting[31] suggested that deformation in peak-aged Al-Zn-Mg alloys was confined to the PFZ's, which rapidly work hardened and fractured. Ryum and Baardseth reported an increase in ductility with wider PFZ's at constant yield stress (430 MPa), in a superpure Al-Zn-Mg alloy[32]. Studies of the same alloy system have shown

no change[33], or a reduction in ductility[34] with increasing PFZ width. It is clear from the variety of reported attributes of the PFZ, that it can not be considered apart from other, pertinent microstructural features. Where there is a large area fraction of grain boundary precipitates, variations in PFZ width (at constant yield stress) have no effect on ductility or fracture toughness[33,35]. In some cases, a reduction of ductility with longer aging times and larger PFZ's can be attributed to the growth of equilibrium precipitates at high angle boundaries[34]. When the matrix deformation is predominantly planar, and there is a small area fraction of grain boundary precipitates, ductility increases with increasing PFZ width[35]. Ryum[36] proposed a model for relaxation of slip band stress concentrations in the PFZ's to explain the increase in ductility. The inhomogeneity of deformation between the PFZ and the matrix is most pronounced in the peak aged condition. Gräf and Hornbogen have reported an average measured strain of approximately one order of magnitude greater than the bulk for PFZ's of an Al-Zn-Mg alloy[37].

The Effect of Grain Size on Ductility

Lütjering, Hamajima and Gysler[38] demonstrated the effect on ductility of reducing the grain size, from 220 μm to 30 μm, of a high purity Al-Zn-Mg-Cu alloy, for two aging conditions. For one condition, deformation was predominantly by precipitate shearing, and for the other, most deformation was localized within PFZ's. By reducing the grain size, true fracture increased from 0.35 to 0.65 for precipitate shearing, and from 0.10 to 0.42 for PFZ localized deformation. In both cases, the increase in ductility was attributed to a reduction in slip length with the decrease in grain size.

Ductile Fracture

During the initial stages of tensile deformation, a commercial, polycrystalline material undergoes uniform elongation. At sites where the compatibility of deformation is difficult, such as at large inclusions or grain boundary triple points, voids form at relatively low strains. At the onset of plastic instability, deformation becomes localized, and a neck develops which leads to increased hydrostatic stresses. Void nucleation, growth and coalescence occur in the center of the neck, resulting in ductile fracture. Examination of the fracture surface reveals a predominance of equiaxed dimples[39].

Voids may be nucleated by particle fracture or interface decohesion. Very small particles may initiate voids. Palmer and Smith[40] observed voids nucleated by 50 Å particles in internally oxidized copper-silicon alloys. They also noted that the number of particles associated with voids at the onset of necking, increased with a decrease in temperature; with 34% contributing at 293 K and 84% at 77 K. Pelloux[41] confirmed, by comparison of dimple size to particle spacing, that only a fraction of the particles present contribute to fracture in age hardening aluminum alloys and maraging steels; and Beachem and Pelloux[42] observed a temperature dependence of void formation in steel.

During the process of ductile fracture in aluminum alloys, voids are formed in two distinguishable stages, corresponding to the size of the particles involved[43]. Failure begins with the fracture or delamination of relatively large constituent particles (~10 μm) at low strains. Van Stone, Merchant and Low[44] have characterized the size, shape, and approximate sequence of fracture of constituent particles for the alloys and

conditions: 2014-T6, 2024-T851, 7075-T351, and 7079-T651. All of the particles analyzed contained Fe or Si, with the exception of one type found in 2024, which was determined to be $CuAl_2$. The second stage of void formation is associated with dispersoid particles[44,45] (~0.1 μm) or large, equilibrium precipitates[46].

Broek[45] observed that the dimples associated with dispersoid particles are too shallow to be caused by the accepted mechanism of axial void growth and coalescence. After a detailed study of 13 aluminum alloys (of 2XXX,3XXX,6XXX and 7XXX types), including in situ electron microscopic observations of fracture, Broek concluded that the conditions for void coalescence are already fulfilled at the instance of dispersoid void formation, and that void growth is, therefore, essentially lateral.

Hahn and Rosenfield[47] maintain that the dispersoid particles are more resistant to fracture than the constituent particles and are involved in the fracture process only after deformation has become localized; they conclude that the dispersoid particles are not injurious to toughness. Other investigators disagree[44,45,46]. Broek[45] claims that the constituent particle voids, which can form at very low strains ($\varepsilon \approx 0.03$, where $\varepsilon_f = 0.25$), cause stress concentrations which determine the site of failure, but that the smaller voids, which cover most of the fracture surface, represent the critical events of ductile fracture. Van Stone, Merchant and Low[44] suggest that coalescence of the larger voids occurs by the formation of void sheets at the dispersoid particles, and that this coalescence stage may be delayed by the reduction in dispersoid size.

The production of high purity alloys (low in Fe and Si) can minimize

the detrimental effect of constituent particles. High purity, however, is not a sufficient condition for the improvements in toughness which have been achieved in alloy development[48]. The improvement in toughness of 7475 over 7075, for instance, is attributed to both high purity and a proprietary thermomechanical treatment which controls the size and distribution of dispersoid particles[49].

Impurity Elements

In addition to Fe and Si, which lower toughness by combining to form large, brittle, constituent particles (e.g. $FeAl_6$ and Mg_2Si), the impurity elements Na and K, which are introduced in trace amounts with Li additions, are detrimental to mechanical properties. Auger analysis of the fracture surfaces of Al-Li alloys has demonstrated the presence of greater than average concentrations of Na and K at subgrain boundary facets.[23] This effect has been attributed to interfacial segregation. In a study of an Al-Mg-Li alloy, with 0.0031 wt% Na, Vainblat, Kopeliovich and Gol'der[50] added sufficient bismuth to form the compound NaBi; and, consequently, observed an increase in toughness from 92 to 110 $kg/mm^{3/2}$, and a change in fracture mode from intergranular to transgranular. It is apparent that even small concentrations of sodium are detrimental to fracture toughness.

FTMT

Aluminum alloys containing copper benefit from cold working immediately after quenching and before aging. This process is termed a final thermal mechanical treatment (FTMT)[51] and has been the subject of several studies[52-56].

The dislocations introduced during FTMT serve as nucleation sites for Cu-rich precipitates, such as θ' (Al_2Cu) and S' (Al_2CuMg), and reduce the effect of a vacancy depleted PFZ. Broek and Bowles[56] studied the effect of 0, 1,3 and 6% stretching prior to aging on 2024 sheet. At low strains (1% and 3%), dislocations act as vacancy sinks, while at high strains (6%) vacancies are generated by the deformation process. Since diffusion relies on vacancies, precipitate growth during natural aging proceeds more slowly than undeformed material for small amounts of strain, and more rapidly after large strains[55]. During artificial aging, Broek and Bowles[56] observed that the 3% strain produced a larger number of small precipitates than the 6% strain, due to the enhanced diffusion rate and rapid, selective growth of the precipitates of the highly strained material. While FTMT results in a more homogeneous distribution of finer precipitates, there is a concomitant loss in ductility related to the amount of deformation.

Rapid Solification

Rapidly solidified powder production methods have been used for the microstructural refinement of aluminum alloys. The techniques developed can be classified into two groups: atomization and splat quenching. Atomization involves the cooling of small (~0.1mm) droplets in a gaseous environment at rates of approximately 10^2 to 10^4 K/s. Splat quenching requires a solid heat sink (e.g. a water cooled copper surface) to obtain particles < 0.1mm thick at cooling rates of 10^5 to 10^7 K/s or greater[57].

High cooling rates result in a smaller grain size, and this may be the cause of the increased ductility reported for some powder processed

aluminum alloys[58-60]. Dendrite arm spacings decrease with increasing cooling rates[61], and this promotes a finer distribution of interdendritically segregated intermetallics, which should contribute to an increase in fracture toughness.

Consolidation of aluminum powders typically involves: sieving, cold compaction, vacuum degassing, hot pressing and extrusion[61]. The degree of bonding between the powder particles and the amount and distribution of the oxides introduced during powder processing are important factors affecting the toughness of the final product. The severity of hot working, the morphology of the powder particle, and the thickness of the particle oxide layer determine the extent to which oxide film rupture and consequent interparticle bonding occur[62,63].

EXPERIMENTAL PROCEDURE

The purpose of this investigation is to determine the influence of certain microstructural parameters on the ductility of an alloy of nominal composition:

Al- 3Cu - 2Li - 1Mg - 0.2Zr.

The material to be studied will be produced by splat quenching, inert gas atomization and conventional ingot methods. The rapid solidification rates of the powder metallurgy (P/M) products should introduce varying degrees of refinement of the grain size and intermetallic particle size and distribution. Further variations in microstructural parameters will be achieved by comparing different heat treatments and by the use of FTMT processing.

The P/M material will be screened, cold compacted, canned, vacuum degassed, and hot compacted at 538 ^{o}C. All material will be extruded at 427 ^{o}C, at a 20:1 ratio. The extrusion cross section dimensions are approximately 7 X 14 mm.

A schematic of the experimental procedure is given in figure 1. Details of the experimental procedures are presented in Appendix I.

Microstructural Characterization

Samples of each extrusion will be retained by the LMSC laboratories for chemical analysis to determine the exact alloy composition. This is particularly important because of the reactive nature of lithium, and since the powder production process may increase the chances of solute loss.

The microstructure of the as extruded material will be examined in order to determine the effect of subsequent heat treatments. Optical metallography will be used to determine the grain size and morphology, and the presence of large intermetallic particles. Bromine etching will be used in conjunction with scanning electron microscopy to observe oxide and intermetallic particle distributions. Particles revealed by bromine etching will be qualitatively identified by EDAX. Thin foils will be prepared and examined by transmission electron microscopy to reveal fine microstructural details. The crystallographic texture will be determined in the extrusion direction by X-ray analysis and described by pole figures of the (111),(200), and (220) reflections.

Processing Optimization

A systematic comparison of processing conditions and resultant mechanical properties will be conducted to develop the optimum combinations of yield strength and ductility. The processing conditions subject to variation include the solution heat treatment (SHT) time and temperature, the aging time and artificial aging time and temperature, and the amount of final thermal mechanical treatment (FTMT).

Preliminary optimization studies have been completed for the splat quenched alloy (Figure 2). Work on the other two materials will employ the same technique. The SHT temperature used was 538 $^{\circ}$C. The effect of higher and lower SHT temperatures on both microstructure and tensile properties (at peak strength) will be examined. TEM observations of the splat quenched alloy indicate that it does not recrystallize during SHT. Pole figures will be plotted for all materials after SHT, to determine the effect of the SHT on texture. Samples of the peak aged material

will be examined by the Guinier method of phase analysis. This information will be used in conjunction with TEM observations, EDAX analysis, and electron diffraction studies to positively identify the phases observed.

Deformation Mechanism Studies

Thin foils will be examined by TEM in order to characterize the deformation mechanisms of peak aged samples. The foils will be prepared from tensile and compression samples. Compression samples will be used to allow the study of large amounts of deformation.

Fracture Mechanism Studies

Fracture surfaces will be examined by SEM. Metallographic sections normal to the fracture surfaces will be studied to supplement the SEM information and help to determine the fracture mode. Fine details of fracture surfaces will be studied by high resolution SEM.

Several investigators have reported methods for studying the sequence of ductile fracture events in aluminum alloys and stressed the importance of obtaining information beyond that available from examination of the fracture surface[44,45,64,65]. Accordingly, flat, polished tensile samples and longitudinal, metallographic sections of tensile samples will be studied after plastic deformation and prior to failure.

Comparison and Conclusions

The microstructure will be characterized for the optimum processing conditions. Deformation and fracture mechanisms will be correlated with the microstructural parameters from the different processing and alloy production methods. Conclusions will then be drawn relating the microstructure and ductility.

APPENDIX I

DETAILS OF THE EXPERIMENTAL PROCEDURE

Microstructural Characterization

Optical Metallography	Polish to 1 μm diamond Examine as polished surface Anodize in 55ml HBF_4 + 948ml H_2O + 7 g Boric acid for 1 min. at 18 volts.
Bromine Etching	Wet grind to 600 grit finish, immerse in boiling solution of 10% Br + 90% CH_3OH for 1.5 min.
TEM	Foils thinned in Struers twin jet electropoliching apparatus, in a 2 : 1 solution of CH_3OH : HNO_3.
Texture	Siemens goniometer, Cu K_α radiation.

Processing

SHT	Salt bath, controlled to $\pm$ 1 °C.
FTMT	Stretched on MTS servo-hydraulic equipment, with strain monitored by a clip on extensometer. Cross head rate of 0.02 mm/s
Artificial Aging	In an oil bath, controlled to $\pm$ 0.5 °C.

Mechanical Testing

Tensile Samples	ASTM standard sub-size, cylindrical, 16mm gage length, polished to a 1 μm diamond finish.
Tensile Tests	Tested on MTS equipment, strain monitored through failure with a clip on extensometer, cross head rate of 0.1mm/s.

Tensile Data	$\sigma_{0.2}$, σ_{uts}, $\frac{A_o - A_f}{A_o}$, $\ln\left(\frac{A_o}{A_f}\right)$, ε_f.
Compression Samples	6mm X 6mm diameter, cylindrical.
Elastic Modulus Data	determined with strain gages, on flat tensile samples
Specific Gravity Data	determined with analytical balance

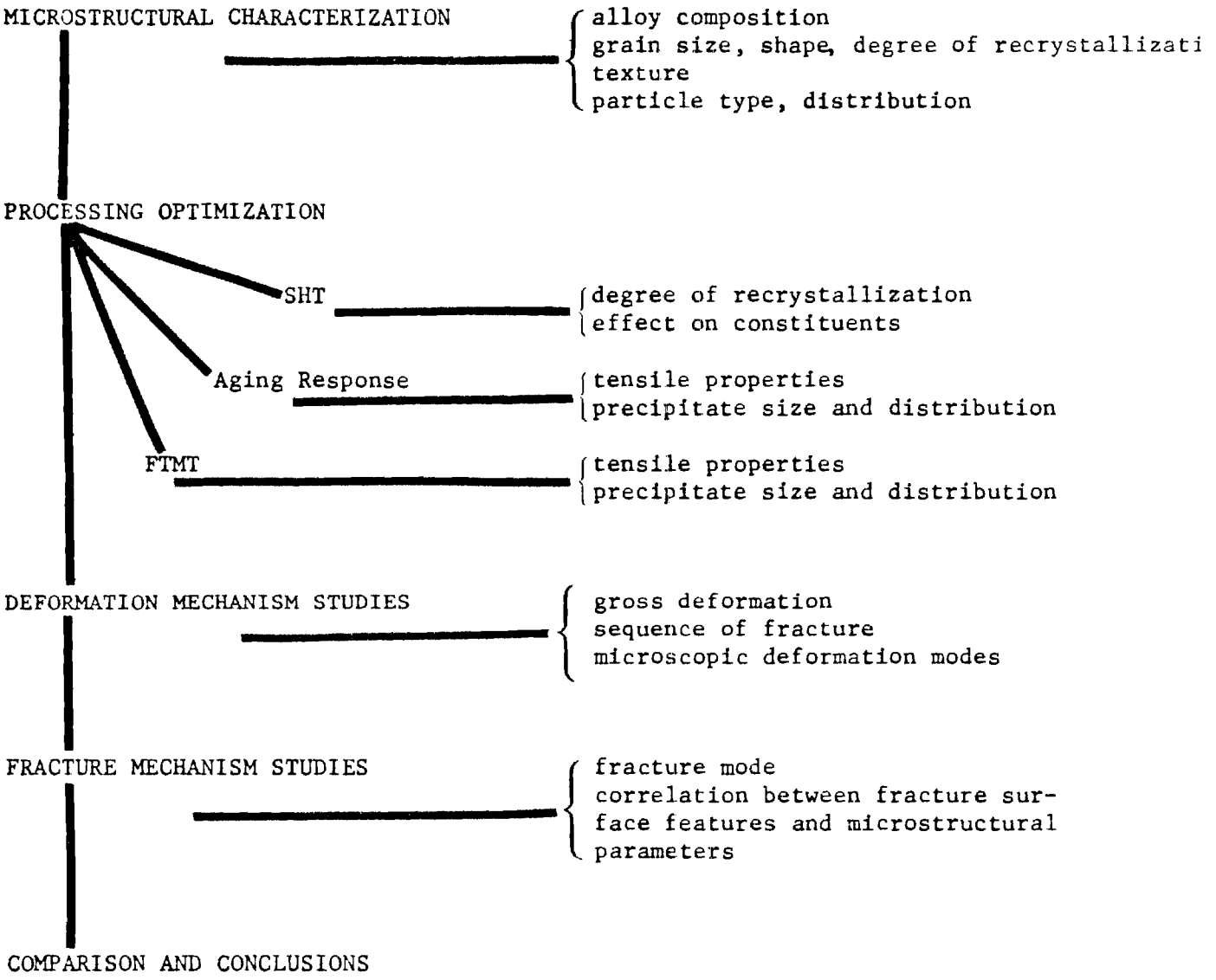

Figure 1. Schematic of Experimental Procedure.

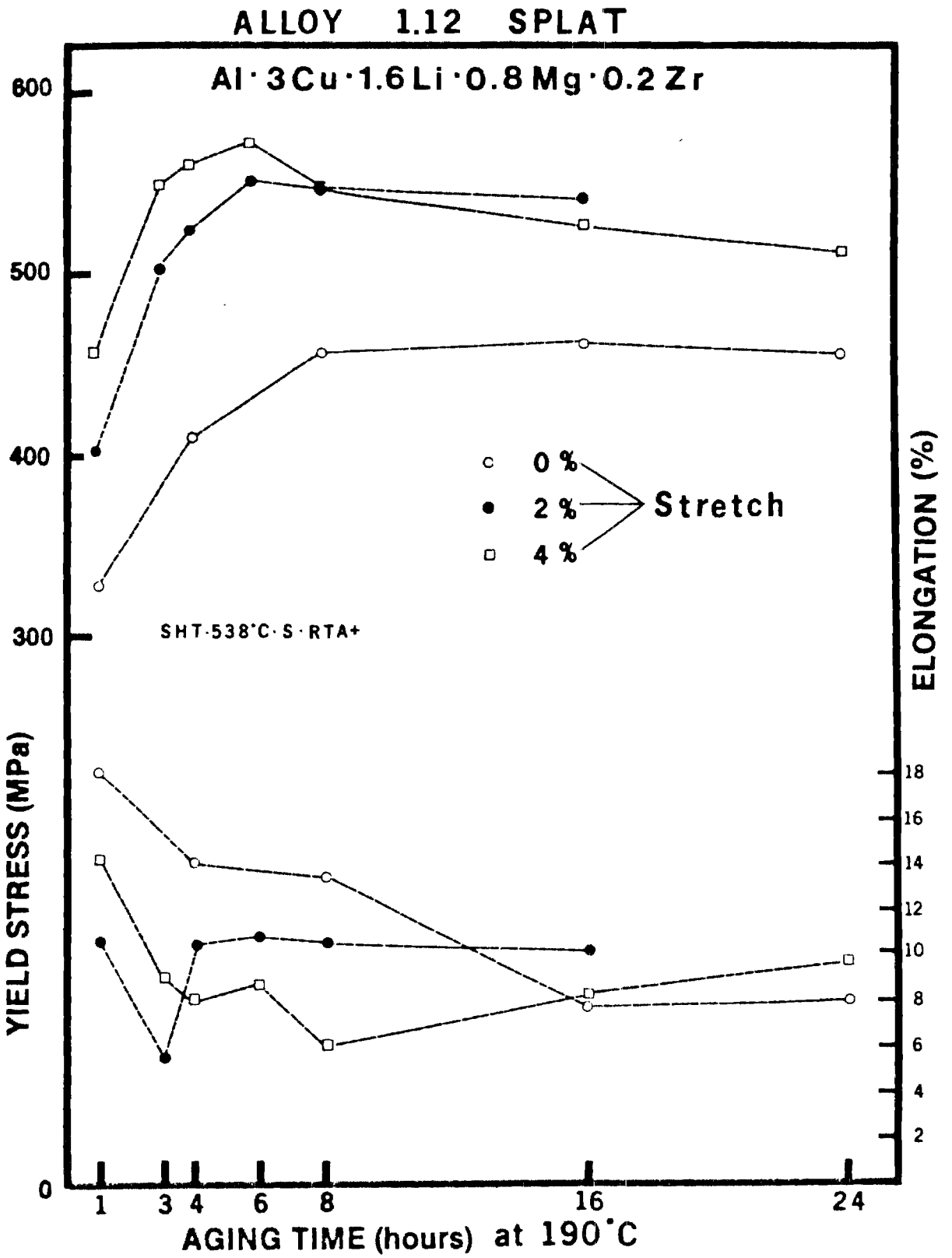

Figure 2. Preliminary Processing Optimization Results for the Splat-Quenched Material.

BIBLIOGRAPHY

1. J. T. Staley, ASTM STP 605, 1976, p. 71.
2. E. A. Starke, Jr., J. Metals, 22, no. 1, 1970, 54.
3. P. M. Kelly, Int. Met. Rev., 18 no. 172-c, 1973, 31.
4. E. Orowan, Symposium on Internal Stress in Metals and Alloys, Institute of Metals, London, 1948, p. 451.
5. E. A. Starke, Jr. G. Kralik and V. Gerold, Mat. Sci. Eng., 11, 1973, 319.
6. G. W. Lorimer, "Precipitation in Aluminum Alloys," Precipitation Processes in Solids, 1976 A. I. M. E. Symposium, 1978, 87.
7. A. Guinier, Nature, 142, 1938, 569.
8. G. D. Preston, Nature, 142, 1938, 570.
9. V. Gerold, Z. Metallk., 45, 1954, 593, 599.
10. P. E. Marth, H. I. Aaronson, G. W. Lorimer, T. C. Bartell and K. C. Russell, Met. Trans. 7A, 1976, 1519.
11. J. M. Silcock, J. Inst. Metals, 89, 1961, 203.
12. H. Perlitz, A. Westgren, Ark. Kemi. Miner. Geol. B., 16, 1943, 13.
13. R. N. Wilson, P. G. Partridge, Acta Met., 13, 1965, 1321.
14. G. C. Weatherly, R. B. Nicholson, Phil. Mag. 1, 1968, 801.
15. B. Noble, G. E. Thompson, Met. Sci. J., 5, 1970, 114.
16. M. Tamura, T. Mori, T. Nakamura, J. Japan Inst. of Metals, 34, 1970, 919.
17. M. E. Fine, Met. Trans., 6A, 1975, 625.
18. T. H. Sanders, Jr., NADC-76397-30, June 9, 1976.
19. J. M. Silcock, J. Inst. Metals, 88, 1955-56, 357.
20. G. E. Thompson, B. Noble, J. Inst. Met., 101, 1973, 111.
21. N. Ryum, Acta Met., 17, 1969, 269.
22. N. Ryum, Aluminium, 53, 1977, 193.
23. T. H. Sanders, Jr., NADC 62269-76-C-0271, Final Report, June 1979.

24. H. Gleiter, E. Hornbogen, Mat. Sci. Eng., 2, 1967, 285.

25. J. D. Boyd, R. B. Nicholson, Acta Met., 19, 1971, 1101.

26. Derek Hull, Introduction to Dislocations, 1965, Pergamon Press.

27. D. W. Pashley, M. H. Jacobs, J. T. Vietz, Phil. Mag., 16, 1967, 51.

28. G. W. Lorimer, R. B. Nicholson, Acta Met., 14, 1966, 1009.

29. H. K. Hardy, T. J. Heal, The Mechanisms of Phase Transformations in Metals and Alloys, Institute of Metals, London, 1956, p. 1.

30. Geisler, Trans. AIME, 180,1949, 245.

31. G. Thomas, J. Nutting, J. Inst. Metals, 86, 1957-58, 337.

32. N. Ryum, K. Baardseth, J. Inst. Metals, 96, 1968, 92.

33. P. T. N. Unwin, G. C. Smith, J. Inst. Metals, 97, 1969, 299.

34. A. J. Cornish, M. K. B. Day, J. Inst. Metals, 99, 1971, 377.

35. S. P. Lynch, Met. Sci. J., 7, May 1973, 93.

36. N. Ryum, Acta Met., 16,1968,327.

37. M. Graf, E. Hornbogen, Acta Met., 25, 1977, 883.

38. G. Lutjering, T. Hamajima, A. Gysler, " Influence of Grain Size on the Fracture of Aluminum Alloys," Fracture 1977, Vol. 2, p. 7.

39. H. C. Rogers, "Effect of Material Variables," Ductility, ASM,1968, p.31.

40. I. G. Palmer, G. C. Smith, "Fracture of Internally Oxidized Copper Alloys," AIME Conf. Oxide Dispersion Strengthening, Bolton Landing, New York, June 1966, Gordon and Breach, New York, 1967

41. R. M. N. Pelloux, Met. Eng. Quarterly, 5, 1965, 26.

42. C. D. Beachem, R. M. N. Pelloux, ASTM STP No. 381, p. 210.

43. A. W. Thompson, P. F. Weibrauch, Scripta Met., 10, 1976, 205.

44. R. H. Van Stone, R. H. Merchant, J. R. Low, Jr., "Investigation of the Plastic Fracture of High-Strength Aluminum Alloys," Fatigue and Fracture Toughness-Cryogenic Behavior, 1974, p. 93.

45. D. Broek, Eng. Fract. Mech., 5, no.1, 1973, 55.

46. I. Kirman, Met. Trans., 2A, 1971, 1761.

47. G. T. Hahn, A. R. Rosenfield, Met. Trans. 6A, 1975, 653.

48. J. S. Santner, Met. Trans., 9A, 1978, 769.

49. J. M. Orden, D. E. Pettit, Met. Progr., 112, no. 8, 1977, 28.

50. Yu. M. Vainblat, B. A. Kopeliovich, Yu. G. Gol'der, Fitz. Met. Metalloved,42, no. 5, Nov. 1976, 1021.

51. J. T. Staley, Met. Eng. Quarterly, 16, 1976, 52.

52. M. Conserva, E. DiRusso, F. Gatto, Alluminio, 9, 1968, 441.

53. F. G. Ostermann, W. H. Reiman, ASTM SMP 467, 1969, 169.

54. F. G. Ostermann, Met. Trans., 2A, 1971, 2897.

55. E. Hornbogen, Aluminium, 43, 1967, 41, 115, and 163.

56. D. Broek, C. Q. Bowles, J. Inst. of Metals, 99, 1971, 255.

57. H. Jones, Aluminium, 54, no. 4, 1978, 274.

58. C. E. Mobley, A. H. Clauer, B. A. Wilcox, J. Inst. of Metals, 100, 1972, 142.

59. B. M. Watts, M. J. Stowell, J. Mater. Sci., 6, 1971, 228.

60. G. Beghi, et. al., J. Mater. Sci., 5, 1970, 820.

61. H. Matyja, B. C. Giessen, N. J. Grant, J. Inst. Metals, 96, 1968, 30.

62. R. E. Lewis, D. Webster, I. G. Palmer, AFML-TR-78-102.

63. D. P. Voss, " Development of High Strength Aluminum Powder Metallurgy Products," European Office of Aerospace Research and Development, 1978.

64. R. H. Van Stone, T. B. Cox, Fractography-Microscopic Cracking Processes, 1976, p. 5.

65. D. L. Jones, H. Liebowitz, Eng. Fract. Mech., 5, no. 2, June 1973, 397.

66. S.J. Harris, University of Nottingham, private communication.

E-19-675

DAPRA
Monthly Report
5 April - 5 May, 1981

Alloy 1.19 was examined in SEM after a bromine etching treatment. Large (approximately 40 μm), rounded, contaminant particles were observed and found (by EDAX) to contain Co and Fe. This type of contamination by superalloy particles is typical of the atomized alloys studied.

Design and preparation of samples for in situ deformation studies was begun. Initially, specimens of an I/M Al-Li binary alloy will be prepared by photoresist etching and electropolishing and observed during deformation in a high voltage electron microscope (HVEM) at Oak Ridge National Laboratories. If the preliminary study is successful, further work will include Alloy 1.12.

High cycle fatigue tests are being conducted on a set of extrusions of alloy 1.2 that was prepared having different aspect (width/thickness) ratios. Previous studies have shown that the aspect ratio has a significant effect on the texture and consequently on the yield strength. The yield strength values range from 521 MPa for round axisymmetric extrusions to 414 MPa for sheet bar extrusions of aspect ratio 8:1. The effect of these parameters, i.e., texture and associated strength, on the stress-life behavior is being evaluated.

DARPA
Monthly Report
for the period
5 May - 5 June 1981

High cycle fatigue tests were conducted on samples of Alloy 1.2. The final tests should be completed before the next report period.

Samples of Alloy 1.12 were prepared for phase analysis by a Guinier-deWolff camera.

Samples of the atomized powder Alloys 1.19 and 1.21 are being prepared for tensile testing.

Work is continuing on the development of samples for *in situ* electron microscopic deformation studies.

DARPA
MONTHLY REPORT
For the Period 5 July to 5 August 1981

The high cycle fatigue tests of the extrusions of Alloy 1.2 have been completed and are presented in Table I. Due to the small number of samples and the amount of experimental scatter, it is difficult to reach a statistically valid conclusion relating fatigue life to the crystallographic texture. However, it appears that the samples of extrusion 1.2 A-8 had consistently longer fatigue lives than those of 1.2 A-11.

Work is continuing on Alloy 1.12, to identify the phases present. Samples on the material were given a peak aging treatment: SHT for 1h @ 811°K (1000°F), WQ + 2 days RTA + 16h @ 463°K (374°F), and examined in a Guinier-deWolff camera. The d-spacings were then determined for the phases detected. The identification procedure is in progress.

TABLE I. ALLOY 1.2 HIGH CYCLE FATIGUE DATA

Extrusion	(MPa)	N_f
1.2 A-5	300	100,000
	300	58,200
	275	382,300
	250	1,160,500
1.2 A-8	300	95,000
	287.5	272,800
	275	500,000
	275	180,000
	262.5	3,418,600
	250	4,200,000
	250	600,000
	237.5	7,729,100
1.2 A-11	450	2,000
	275	150,000
	275	108,600
	250	168,100
	225	7,000,000*
	225	7,000,000*
1.2 A-12	300	28,900
	300	58,500
	300	141,600
	275	50,400
	275	53,100
	250	4,612,500
	225	36,700
	200	7,000,000*

*Did not fail

DARPA
Quarterly Report
For the Period 5 June - 5 September 1981

Alloy 1.12

Phase analysis studies have begun on alloy 1.12 (Al-3Cu-1.6Li-0.8Mg-0.2Zr, splat-quanched). Two methods have been employed: bromine etching and x-ray diffraction.

For the bromine etching technique, small (2x4x8 mm) samples were cut, wet-ground on 600 grit SiC paper and etched for one minute in a boiling solution of 10% bromine + 90% methanol (by volume). The samples were then examined in a JEOL 100C STEM in the SEM mode. An EDAX unit was used to determine the elements present in specific particles. Large, cylindrical particles with lengths on the order of 1 μm were observed, frequently in the vicinity of grain bounadries, and found to contain relatively large amounts of iron. These may be Al_7Cu_2Fe, but a definite identification has yet to be completed. Further examination of these particles will attempt to establish a relationship between their occurrence and the prior particle type (e.g. splat versus in-flight-solidified).

X-ray diffraction studies were conducted on peak-aged [SHT 1h 811K (1000°F), WQ, 2d RTA, 16h 463K (374°F)] samples. Samples were thinned for analysis in a Guinier-deWolff camera by the following technique: Thin (0.5 mm) sections were cut from the transverse plane of the extrusion and chemically thinned in a solution of 400 ml HCl, 400 ml H_2O, 20 grams NaCl and 4 grams $NiSO_4$. The sections were then cleaned by immersion first in 5% NaOH and then concentrated HNO_3. This preparation method offers the advantage of eliminating the line broadening deformation associated with the production of powder samples of age hardened alloys. The disadvantage is that the relative line intensities cannot be directly compared to those from powder diffraction measurements, since the texture of the alloy significantly affects the intensities.

Preliminary results from the Guinier-deWolff exposures are presented in Table 1. The presence of the equilibrium phases T_1 and T_2 is confirmed. This is in agreement with the phase section suggested by H. K. Hardy and J. M. Silcock for a 3 wt.% Cu, 2 wt.% Li alloy.[1] T_1 is a hexagonal phase with an approximate composition of Al_2CuLi; T_2 has an approximate composition of Al_6CuLi_3 and an undetermined structure.

Al-Cu-Mg alloys with a Cu:Mg weight ratio of 2.2:1 form a pseudo-binary Al-AlCuMg system, and the precipitation of S phase (Al_2CuMg) occurs.[2] Both the equilibrium S and its metastable precursor, S', have a lath-morphology and three specific orientations relative to the matrix.[3-5] It is feasible that Mg participates in the precipitation sequences of this alloy, although no quaternary Al-Cu-Li-Mg phase has been previously reported. The unidentified lines in Table 1 are not associated with any reported Al-Cu-Li phases, Al-Li or Al-Cu binary phases or ternary Al_2CuMg, S, phase. They may be due to either the precursors of the identified phases T_1 and T_2 or to unidentified Al-Cu-Li-Mg phases.

In transmission electron microscopy (TEM) micrographs, T_1 exhibits a plate-morphology.[6] The partially coherent precipitates in this alloy are characterized, predominantly, by a lath-morphology, similar to S'. The specific orientations of these precipitates have not yet been determined.

Alloy 1.2

The high cycle fatigue tests of the extrusions of alloy 1.2 (Al-3Li-2Cu-0.2Zr) have been completed and are presented in Table 2. Due to the small number of samples and the amount of experimental scatter, it is difficult to reach a statistically valid conclusion relating fatigue life to the crystallographic texture. However, it appears that at stresses below 275 MPa (40 ksi), samples from extrusion 1.2 A-8 had consistently longer fatigue lives than

those of 1.2 A-11, as was predicted. Reason for the anomalously short life of some samples at low stress levels is not known, but is probably due to microstructural inhomogeneities. Attempts to determine fracture origin microstructural features was inhibited by corrosion products which formed on the fracture surfaces. Additional specimens may be tested at the lower stress levels if sufficient material can be made available.

TABLE 1

Preliminary Guinier-deWolff Results

Lines Detected	Reported, Strong, Diffraction Lines		
	Al*	T_1**	T_2**
d,Å	d,Å/hkl	d,Å/hkl	dÅ
4.97			
4.65		4.69/002	
4.25			4.24
3.88			
2.41			
2.34	2.338/100		
2.28			
2.25			2.25
2.14		2.145/200	
2.21			
2.11			
2.04			
2.02	2.024/200		2.01
2.00			
1.98		1.949/202	1.97
1.43	1.431/220		
1.39			1.39
1.22	1.221/311		

* ASTM, X-ray Powder Data File
** H. K. Hardy, J. M. Silcock, J. Inst. Metals, 84, 423.

TABLE 2

Al-Li Alloy 1.2 High Cycle Fatigue Data

Extrusion			Tensile		Fatigue		
No.	Reduction Ratio	Aspect Ratio	Yield Strength MPa (ksi)	Strain to Fracture %	Stress MPa (ksi)	Cycles to Failure N_f	-10^x
1.2 A-5	20:1	2:1	444 (64.3)	4.2	300 (44)	1	5
					300 (44)	5.8	4
					275 (40)	3.8	5
					250 (36)	1.2	6
1.2 A-8	20:1	2:1	445 (64.6)	5.2	300 (44)	9.5	4
					287.5 (42)	2.7	5
					275 (40)	5	5
					275 (40)	1.8	5
					262.5 (38)	3.4	6
					250 (36)	4.2	6
					250 (36)	6	5
					237.5 (34)	7.7	6
1.2 A-11	10:1	8:1	414 (60.0)	5.9	450 (65)	2	3
					275 (40)	1.5	5
					275 (40)	1.1	5
					250 (36)	1.7	5
					225 (33)	7	6*
					225 (33)	7	6*
1.2 A-12	20:1	1:1	518 (75.1)	2.3	300 (44)	2.9	4
					300 (44)	5.8	4
					300 (44)	1.4	5
					275 (40)	5	4
					275 (40)	5.3	4
					250 (36)	4.6	6
					225 (33)	3.7	4
					200 (29)	7	6*

*Did not fail.

REFERENCES

1. H. K. Hardy and J. M. Silcock, "The Phase Sections at 500°C and 350°C of Aluminum-Rich Aluminum-Copper-Lithium Alloys," J. Inst. of Metals, 84, 1955, 423.

2. J. M. Silcock, "The Structural Aging Characteristics of Al-Cu-Mg Alloys with Copper: Magnesium Weight Ratios of 7:1 and 2.2:1," J. Inst. of Metals, 89, 1961, 203.

3. H. Perlitz and A. Westgren, "The Crystal Structure of Al_2CuMg," Ark. Kemi Miner. Geol. B, 16, 1943, 13.

4. R. N. Wilson and P. G. Partridge, "The Nucleation and Growth of S' Precipitates in an Aluminum-2.5% Copper-1.2%Magnesium Alloy," Acta Met. 13, 1965, 1321.

5. G. C. Weatherly and R. B. Nicholson, "An Electron Microscope Investigation of the Interfacial Structure of Semi-coherent Precipitates," Phil. Mag., 1, 1968, 801.

6. B. Noble and G. E. Thompson, "$T_1(Al_2CuLi)$ Precipitation in Aluminum-Copper-Lithium Alloys," Met. Sci. J., 6, 1972, 167.

FRACTURE AND FATIGUE RESEARCH LABORATORY

QUARTERLY REPORT

ADVANCED ALUMINUM ALLOYS FROM RAPIDLY SOLIDIFIED POWDERS

1. Aluminum-Lithium Alloys

Tensile test data have been collected to determine the optimum processing conditions for the second iteration alloy 1.12 (Al-3Cu-1.6Li-0.27r). All test specimens were subjected to a solution-heat-treatment at 538°C for 0.5h, followed by quenching in cold water, room temperature aging for 2 days and artificial aging at 190°C. The Cu-rich strengthening precipitates in this alloy preferentially nucleate at dislocations, and deformation prior to aging has been shown to cause an increase in yield strength. This effect was investigated by stretching some tensile samples to 2% or 4% plastic elongation immediately after quenching. Two specimens were tested for each set of conditions. The tensile test results are given in Table I and represented graphically in Figure 1. Peak strength occurred after 6h at 190°C for both the 2% and 4% stretched material and after 16h at 190°C for the unstretched material. The peak strength for the 4% stretch is only slightly higher than that for the 2% and the 2% stretch provides the best combination of yield strength and ductility of the conditions tested.

A significant variation was noted in the properties of companion samples, particularly in the ductility measurements. Some samples, notably the two tested after 2% stretching and 3h aging at 190°C, provided elongation values which were lower than would be expected from comparison to the other tests. This may be indicative of material inhomogeneities, such as local oxide concentrations.

A polarized light optical micrograph of the longitudinal-short plane of alloy 1.12 is presented in Figure 2. The interface between areas of different

contrast correspond to high angle grain boundaries. The grains range in thickness from approximately 5 to 40 μm and from several hundred to several thousand μm in length. The grains are highly elongated in the longitudinal direction, as are the splat particles after extrusion. Many of the grain boundaries coincide with the original powder particle boundaries.

TEM observation of this alloy reveals an unrecrystallized microstructure with a sub-grain size of approximately 3 μm. Low magnification TEM photographs of 2% stretched and unstretched specimens, aged 8 h at 190°C are compared in Figure 3. Two types of precipitate are readily distinguished in the unstretched material; find, needle-like precipitates which are located predominantly in the matrix, and rounded, grain-boundary precipitates. The needle-like precipitates are considered to be S' (Al_2CuMg) since tilting of the TEM foil does not produce evidence of the plate morphology characteristic of θ' (Al_2Cu). Some sub-grain boundaries are decorated by S' precipitates, and for these boundaries, the large, rounded precipitates are absent. Selected area electron diffraction analysis across these boundaries indicates that they are of a lower angle misorientation than those that contain the larger S precipitates. The stretched sample is markedly different in appearance due to the much finer distribution of S' phase. This is a result of the increased number of nucleation sites produced by the deformation prior to aging. There are noticeably fewer grain boundary precipitates in the stretched material, and this suggests two things: first, that the precipitates are related by composition and represent competing precipitation processes, and second, that the stretching operation increases the volume fraction of S' in the matrix along with producing a finer distribution, and this decreases the probability of sub-grain boundary precipitation.

The TEM photographs of Figure 4 were prepared from tensile samples tested after 4 h and 16 h aging at 190°C, and represent both unstretched and 4% stretched

material. The 4 h and 16 h samples were chosen for comparison because they are close to the peak aging times for the stretched and unstretched material, respectively. For both aging conditions the S' particles are more numerous and of a narrower size distribution for the stretched samples. The unstretched material shows significant growth of individual particles with increased aging from 4 h to 16 h. The S' precipitates of the stretched material do not undergo an obvious increase in size, but show an apparent increase in number for the same aging period.

The volume fraction of S' precipitates is much lower in this alloy (with 1.6 wt. % Li) than that of the first iteration alloys studies (all which contained 3 wt. % Li). A bright field, dark-field pair and the associated diffraction pattern (giving the bright-field orientation) are shown in Figure 5. The foil was produced from an undeformed sample aged for 8 h at 190°C.

A bromine etching technique has been used to prepare specimens for SEM examination of particles. The technique consists of wet grinding the sample to a 600 grit surface and etching for one minute in a boiling solution of 10% bromine and 90% methanol. SEM photographs of a bromine etched sample of alloy 1.12 is shown in Figure 6 and compared to a TEM photograph of a high-oxide concentration region at the same magnification. It is clear from the SEM photograph that the prior particle oxide boundaries are broken up during the extrusion of this alloy (ratio 20:1). Previous studies of oxides in 8:1 extrusions of first iteration alloys (i.e., 1.1 and 1.6) had demonstrated the existence of semi-continuous oxide networks. The oxide particles remain, however, as the largest particles in the alloy and serve as crack nucleation sites.

A sample of the atomized powder alloy 1.13 was examined by SEM after bromine etching. Very large particles were found and identified by EDAX as Fe-Ni-Cr (i.e., possibly stainless steel). Figure 7 is a photograph of one particle

examined. These impurities are presumably the cause of the low yield strength and ductility values observed (Table 2).

Figures 8 and 9 show the fracture surfaces of tensile samples stretched 0% and 2% (respectively) prior to aging for 8 h at 190°C. There is no obvious difference in appearance. Both fractures are intergranular, with features corresponding in size to the sub-grain size. A side view (tilted 45°) of a 2% stretched specimen at peak aged temper (6 h, 190°C) is provided by Figure 10b. Vertical ridges can be seen which are oriented in the direction of the tensile and extrusion axes. Similar features are found on the fracture surface of the 8 h, unstretched sample shown in Figure 8a. Comparison of these fractographs with Figure 2 suggests that the ridges are due to decohesion along high angle grain boundaries or, possibly, the original powder particle interfaces.

2. Quantitative Microstructural Analysis and Mechanical Property Correlations of Al-Fe-Ni-Co Alloys

A microstructural study was begun to determine the degree of heteogeneity and its effect on the mechanical properties of the 2.2A and 2.4A Al-Fe-Ni-Co alloys. Recent work on the 5 atomic % solute alloys by T. H. Sanders, et al.[1] (Appendix) has shown the biomodal distribution of particle sizes evident in these alloys. To adequately model the effect of large- and small -particled bands on the over-all strength and ductility of these dispersion-hardened alloys, quantitative microstructural measurements were made. Also, several electropolished tensile specimens of selected alloys were stressed in the region of plastic instability to observe the accommodation of strain in the different particle-size regions.

Experimental Procedure. Planar surfaces ground with 600 grit paper were etched for 1 minute using a 10% volume bromine in methanol solution heated to just below boiling. This technique was found to most adequately expose entire particles that

could be photographed using SEM for size analysis on a MOP-3. Typical samplings for a region included over 200 small particles or 150 large particles for each alloy/process variation. Particles in both regions were assumed spherical and diameter measurements were always made in one direction. N_L measurements were made on (1) optical photomicrographs taken at 1000X for large particles and (2) scanning electron photomicrographs taken at 20,000X for small particles. For the former, a mechanically polished (with 1 μm diamond paste) planar surface was etched slightly using a standard Keller's etch. In the case of the latter, the specimens were electropolished at 236K in a 1:3 nitric in methanol solution at 18V. The small dispersoids were visible in an effective planar surface using the high resolution of the JEOL-ASID scanning attachment. Volume fractions for the large- and small-particled regions were determined by measuring P_p using a 25 point grid for 50 random areas of each region and assuming $P_p = A_a = V_v$. These point counts were done at 400X on the same etched surfaces used to calculate N_L. Tensile specimens were ground with 600 grit paper and then electropolished using a Tenupol and the same conditions as above.

Results and Conclusions. Quantitative values for mean diameters, $\bar{D}$, region volume fractions V_v, particles per unit length N_L, and calculated values of the mean intercept length λ are listed in Table 3. In Figure 11, the SEM photomicrograph of the necked region of an electropolished tensile specimen stressed to 67% of expected total elongation shows the anticipated particle/matrix interface separation in the large particled region. Weak mechanical bonds between large particles that have been pushed together during processing also break to initiate voids that can then coalesce. Small-particled regions show a fine planar slip. The data were analyzed according to a model proposed by Gurland[2], Figure 12.

$$\sigma_{\alpha y} = \sigma_{o\alpha} + k_\alpha \lambda_\alpha^{-\frac{1}{2}}$$

In this model $\sigma_{\alpha y}$ is the yield stress, $\sigma_{o\alpha}$ the frictional stress, k_α a constant related to the strength of the slip resisting boundary and λ_α is the boundary spacing. The model is applicable to systems which consist of unconnected particles dispersed in a continuous matrix. The data are thus represented by a Petch type relationship. All alloys except the argon splat material appear to fit this relationship. This deviation of the argon splat data is related to the large volume fraction of very coarse particles present in this microstfucture. A series of 6% total solute Al-Fe-Ni-Co alloys will be incorporated with the data on the 5 and 7.5 atomic per cent solute. At that time an attempt will be made to determine if the exponent is close to $-\frac{1}{2}$.

References.

1. Sanders, T. H., Jr., J. W. Johnson, and E. E. Underwood, "Microstructural Analysis of Wrought RSP Al-Fe-Ni-Co Alloys," in Proceedings of the Second International Conference on Rapid Solidification Processing; Principles and Technologies, Reston, VA, March 23-26, 1980.

2. Gurland, J., "A Structural Approach to the Yield Strength of Two-Phase Alloys with Coarse Microstructures," Mat'l. Sci. and Engineering, 40, (1979), pp. 59-71.

TABLE 1. Tensile Test Results for Alloy 1.12

Stretch, %	Aging, h, 190°C	$\sigma_{0.2}$ MPa	σ_{uts} MPa	ϵ_f*, % of 16 mm gage length
0	1	331	485	18
		326	498	18
"	4	417	542	14
		406	528	14
"	8	453	540	14
		460	546	13
"	16	475	576	8.8
		449	531	6.6
"	24	447	523	11
		462	560	8.5
2	1	314	547	10
		300	554	11
"	3	478	543	5
		532	590	6.3
"	4	545	600	10
		507	581	11
"	6	544	621	12
		566	623	9.1
"	8	549	605	6.6
		552	606	8.8
"	16	533	590	11
		556	608	10
"	100	447	490	12
		450	489	8.8
4	1	456	536	14
		459	549	14
"	3	544	586	7.2
		558	589	11
"	4	556	628	8.8
		562	630	7.4
"	6	574	677	7.5
		574	676	10
"	8	542	599	5
		558	632	7.2
"	16	526	616	8.3
		527	617	8.5
"	24	510	600	6.7
		525	619	9.3

*These figures were determined from gage marks on the specimens and may not be as accurate as those obtained with an extensometer.

TABLE 2. Tensile Test Results of Alloy 1.13

Stretch %	Aging h, 190°C	σ_{o_2} MPa	σ_{uts} MPa	ε_f
2	6	290	375	3.7
2	6	283	383	8.9

TABLE 3 : QUANTITATIVE METALLOGRAPHIC DATA OF Al-Fe-Ni-Co ALCOA FIRST ITERATION ALLOYS 2.2A AND 2.4A, HOT COMPACTED AND EXTRUDED AT VARIOUS TEMPERATURES

	SMALL-PARTICLED REGIONS				LARGE-PARTICLED REGIONS			
ALCOA ALLOY DESIGNATION	$\bar{D}^L$ (μm)	V_V^S (%)	N_L^S (μm^{-1})	λ^S (μm)	$\bar{D}^L$ (μm)	V_V^L (%)	N_L^L (μm^{-1})	λ^L (μm)
513702-1	0.353	97.94	1.14	0.640	1.02	2.06	0.264	3.12
513682-2	0.10	--	2.14	0.401	0.66	--	--	--
513687-1	0.14	75.1	3.34	0.21	2.25	24.9	0.204	3.40
513702-2	0.175	96.97	1.286	0.661	1.00	3.03	0.238	3.53
513702-3	0.205	--	1.575	0.499	1.06	--	--	--
513693-1X	0.40	--	1.57	0.370	--	--	--	--
513697-1X	0.41	98.14	1.21	0.552	1.14	1.86	0.138	6.57
513697-2	0.142	94.42	2.48	0.308	0.86	5.58	0.283	2.96
513697-3X	0.145	90.02	2.41	0.318	0.66	9.98	0.305	2.84

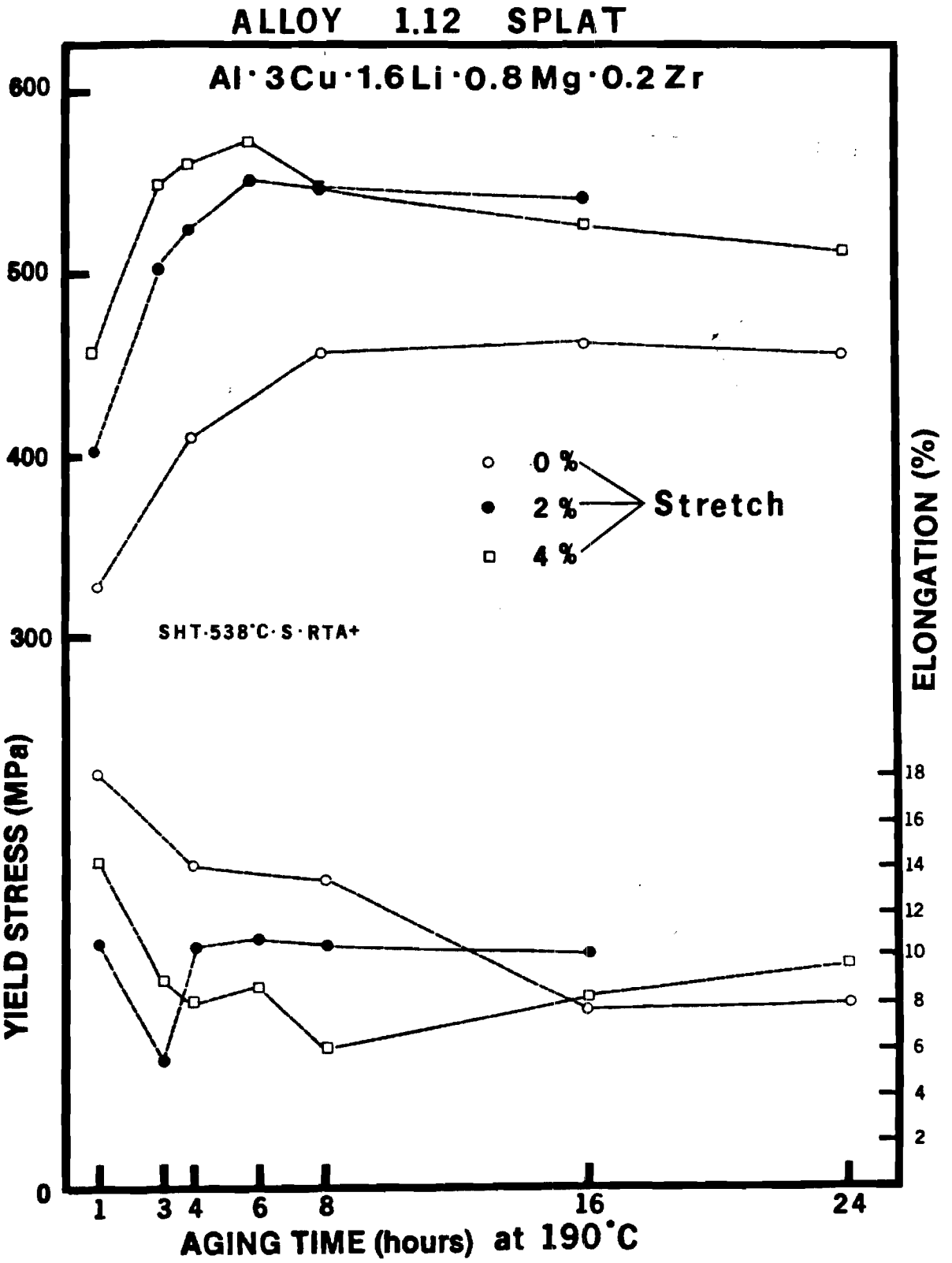
ALLOY 1.12 SPLAT
Al·3Cu·1.6Li·0.8Mg·0.2Zr
600
500
400
300
0
0 %
2 %
4 %
Stretch
SHT·538°C·S·RTA+
YIELD STRESS (MPa)
ELONGATION (%)
18
16
14
12
10
8
6
4
2
1
3
4
6
8
16
24
AGING TIME (hours) at 190°C

Figure 1.

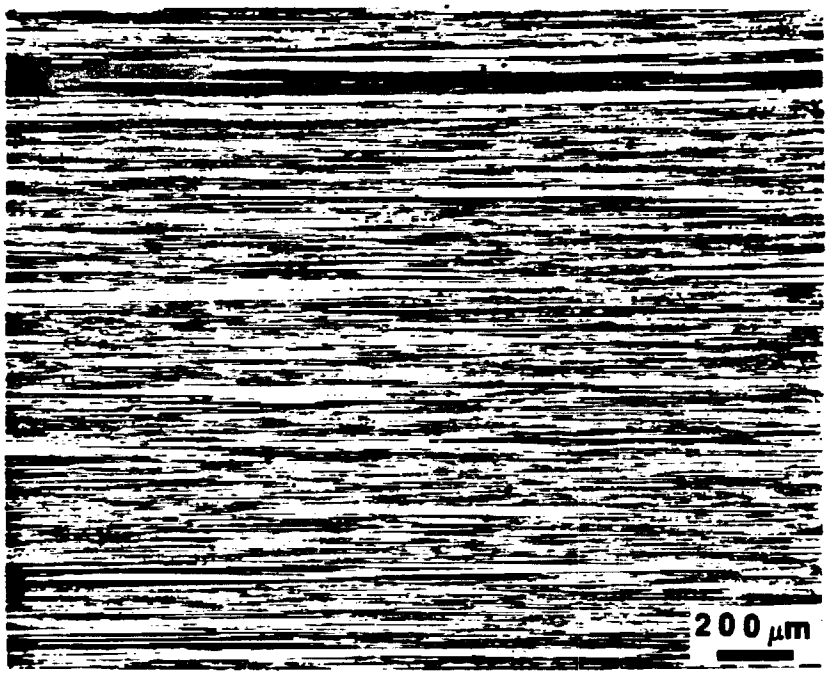

Figure 2. Optical micrograph of the longitudinal section of alloy 1.12, polarized light.

(a)

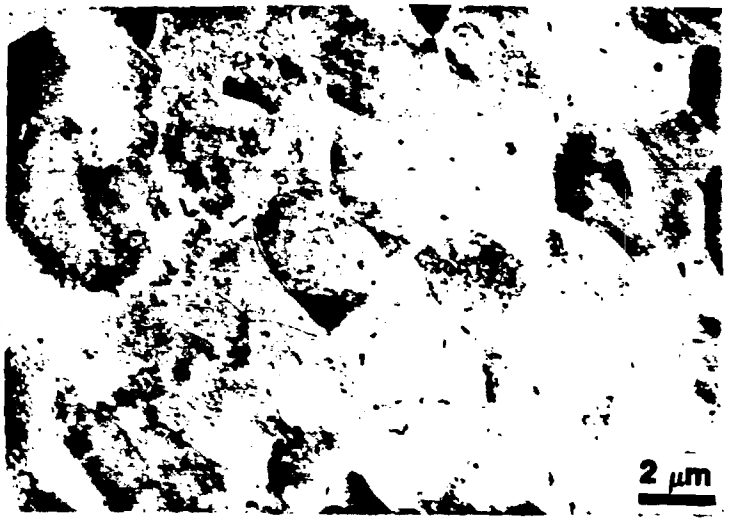

(b)

Figure 3. Transmission electron micrograph of alloy 1.12 after aging 8 h at 190°C.

(a) No stretch prior to aging,

(b) 2% stretch prior to aging.

0%, 4h

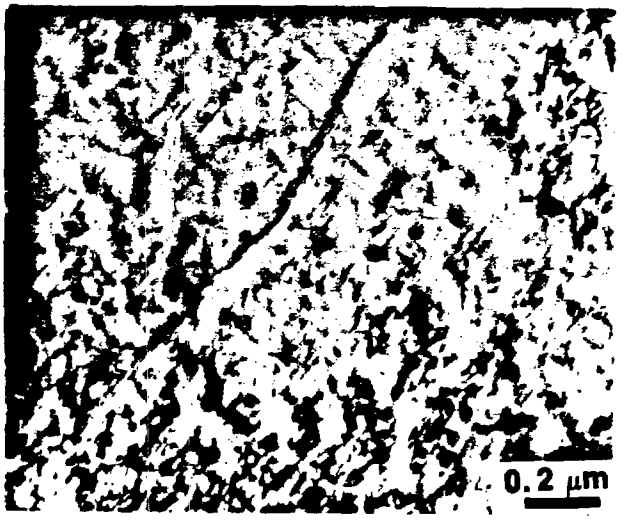

4%, 4h

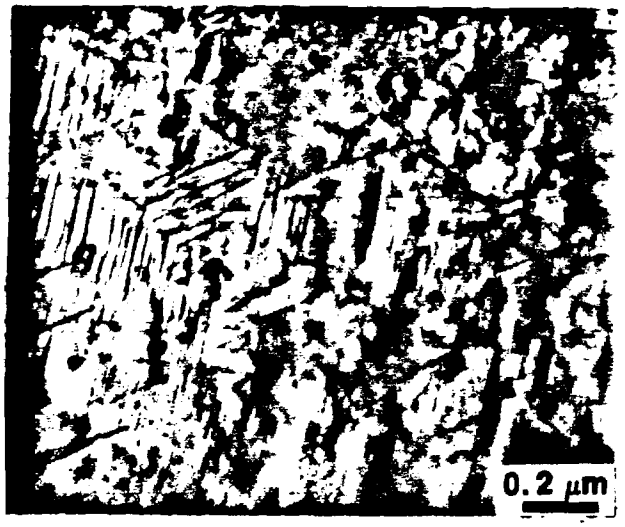

0%, 16h

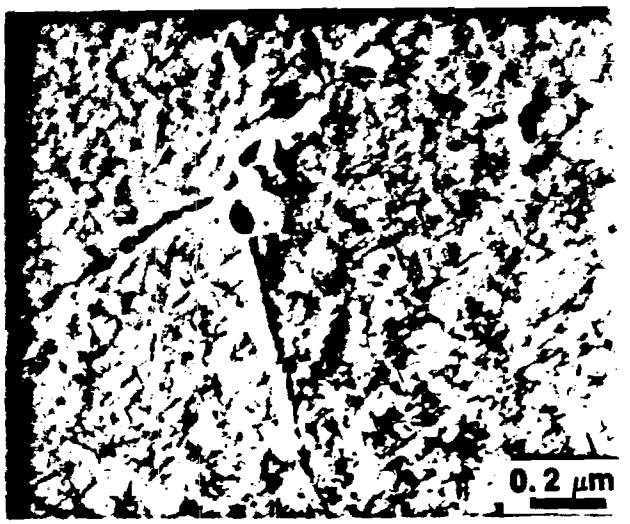

4%, 16h

Figure 4. Transmission electron micrographs of alloy 1.12 showing the effects of stretch, and aging time at 190°C.

(a)

(b)

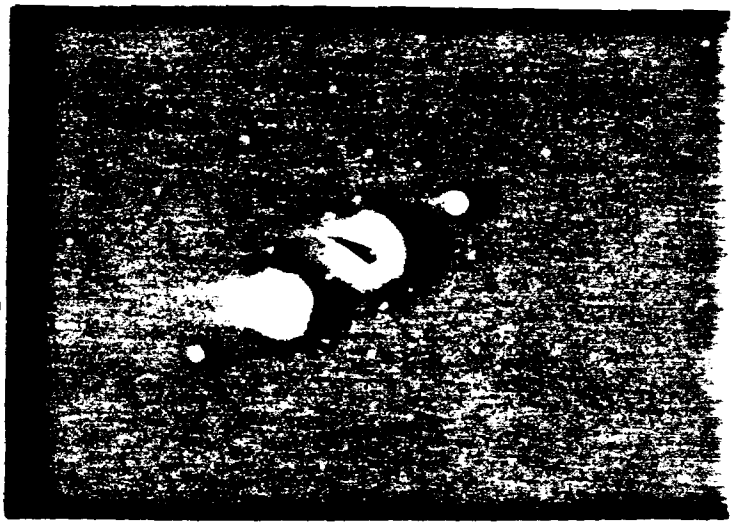

(c)

Figure 5. Transmission electron micrographs showing the distribution of S' precipitates after aging 8 h at 190°C.
(a) bright field (b) SAD (c) dark field

(a)

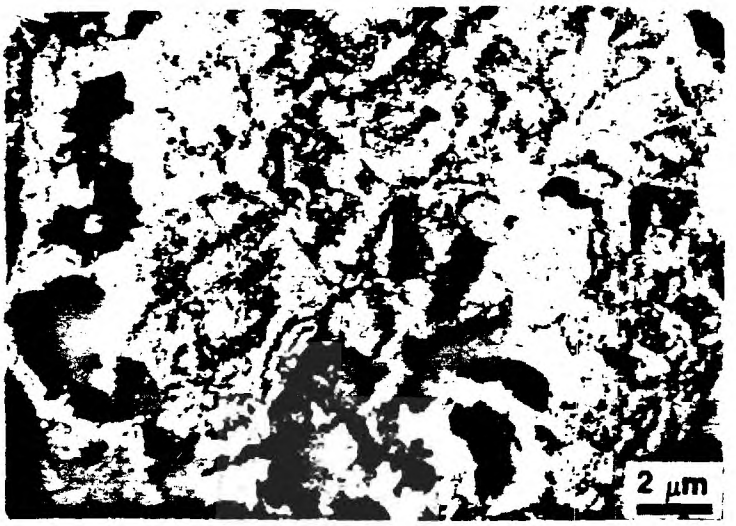

(b)

Figure 6. Scanning electron micrograph (a) and transmission electron micrograph (b) showing oxide particles in alloy 1.12 transverse sections.

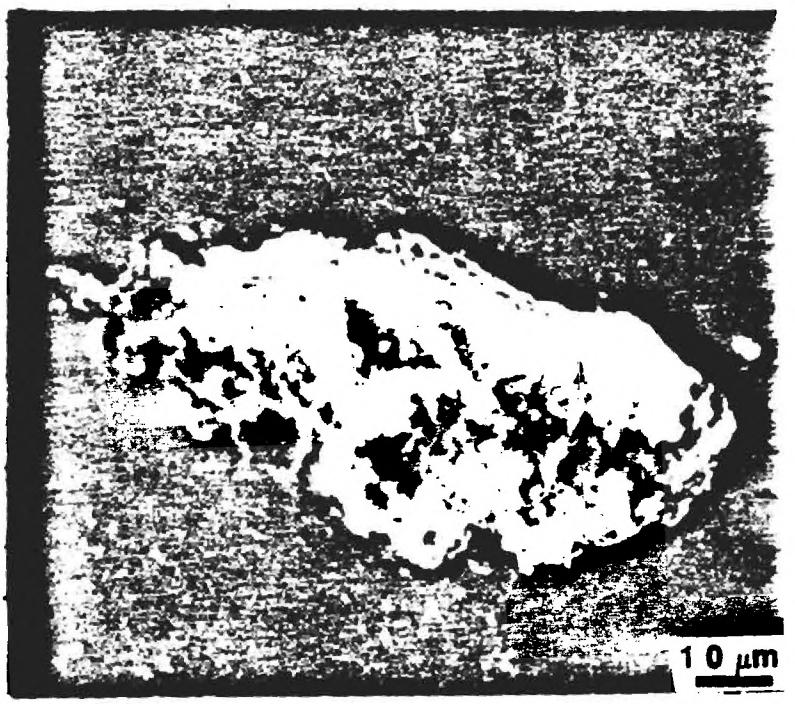

Figure 7. SEM micrograph of Fe-Ni-Cr impurity in alloy 1.13, revealed by bromine etching.

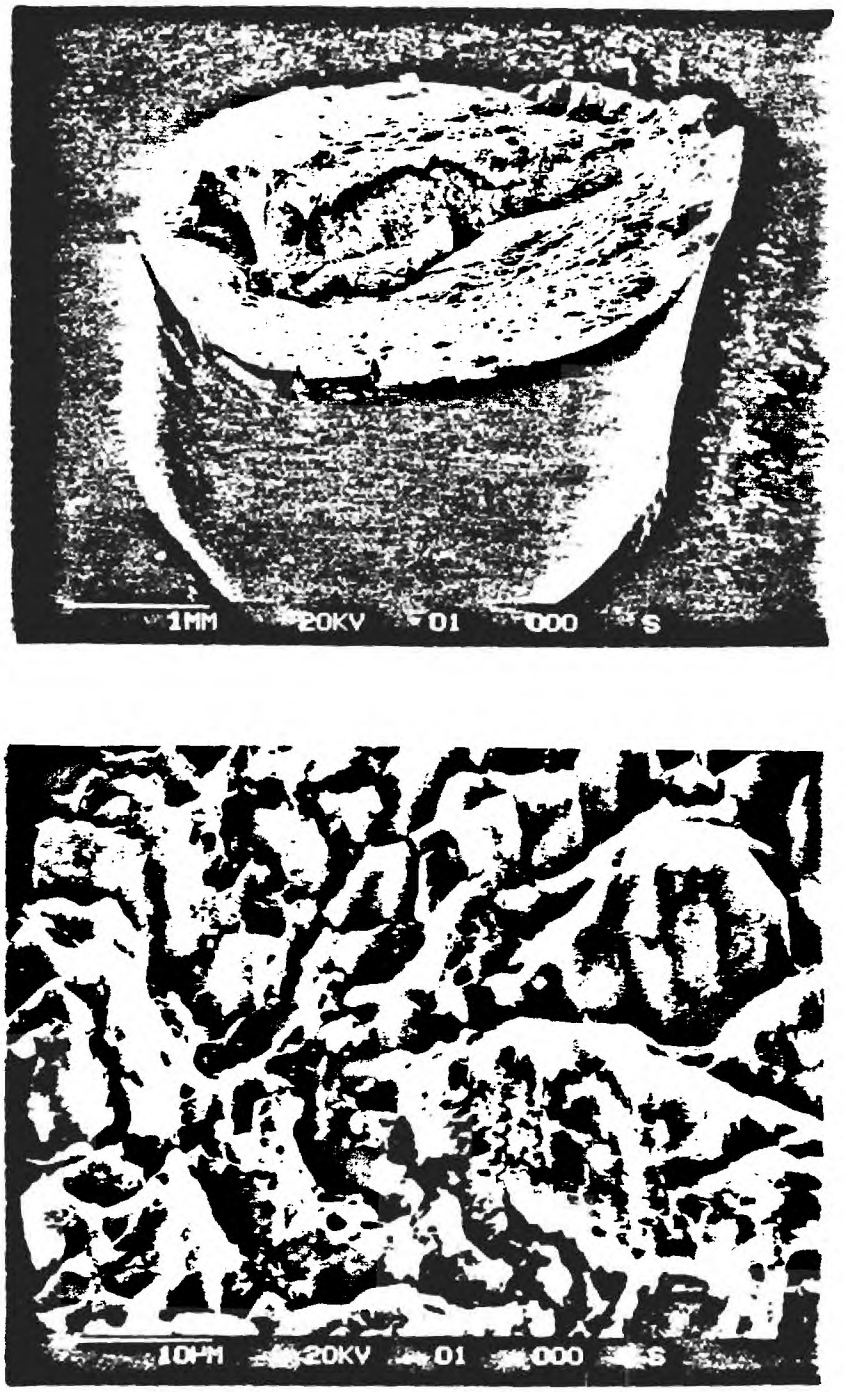

Figure 8. Scanning electron microscopy fractographs of an alloy 1.12 tensile sample, unstretched prior to aging for 8 h at 190°C.

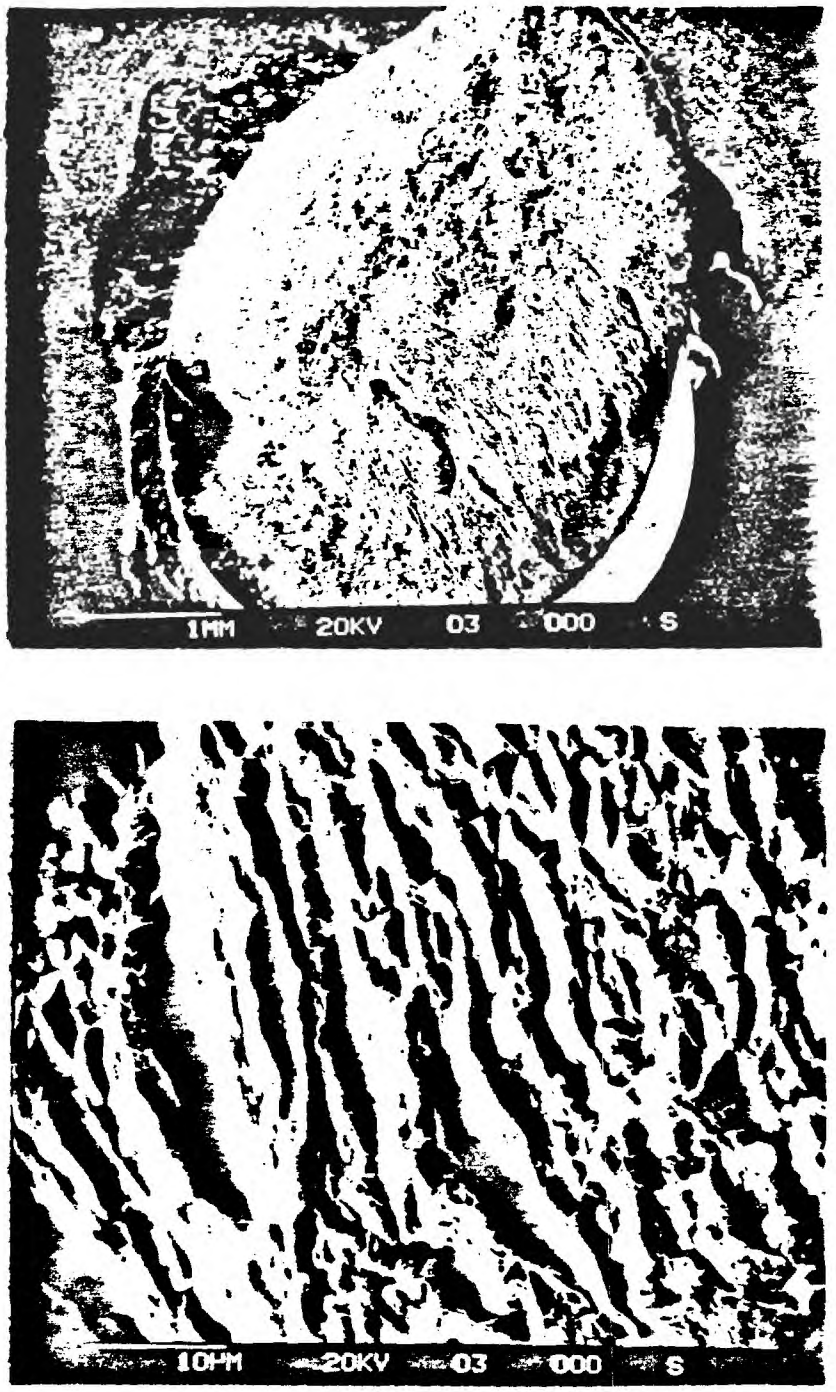

Figure 9. Scanning electron microscope fractographs of alloy 1.12 tensile sample, stretched 2% prior to aging for 8 h at 190°C.

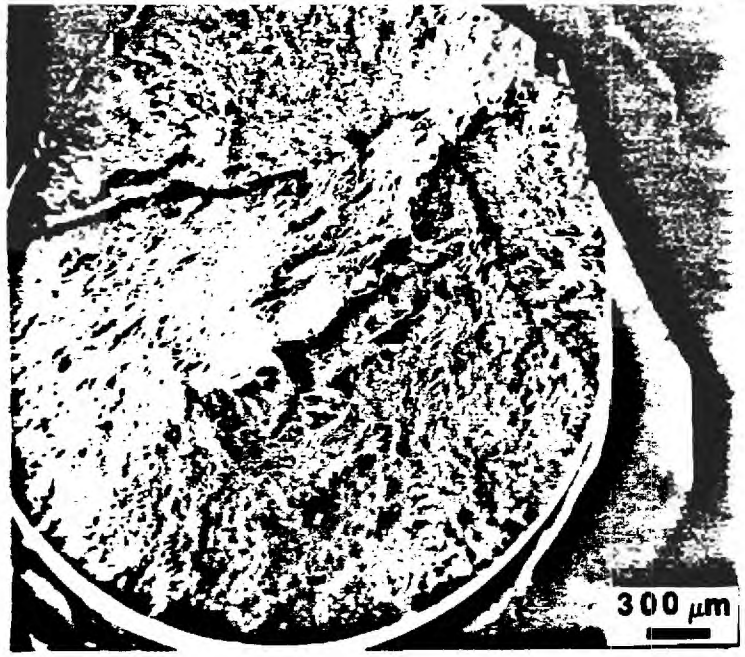

(a)

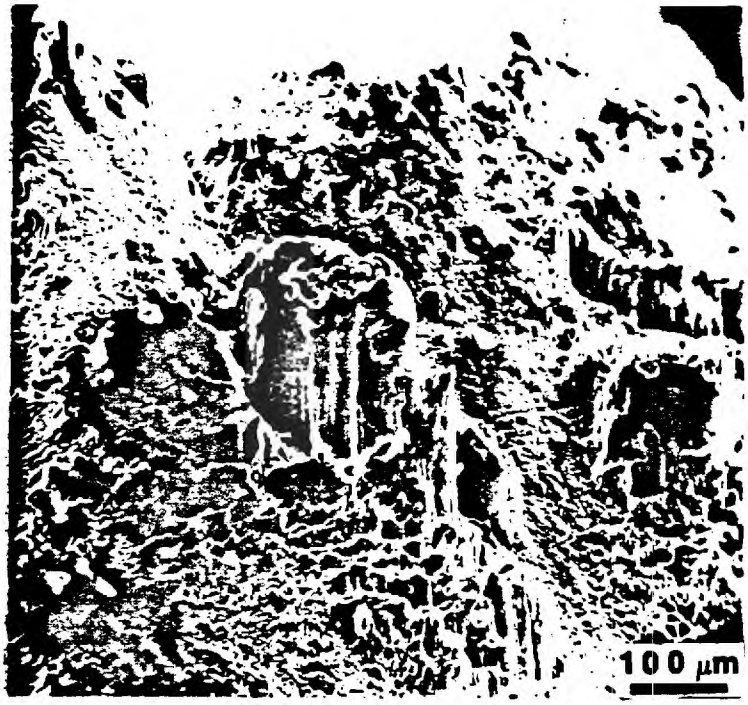

(b)

Figure 10. Scanning electron microscope fractographs of an alloy 1.12 tensile sample stretched 2% prior to aging 6 h at 190°C. (a) low magnification (b) 45° tilt, center of specimen

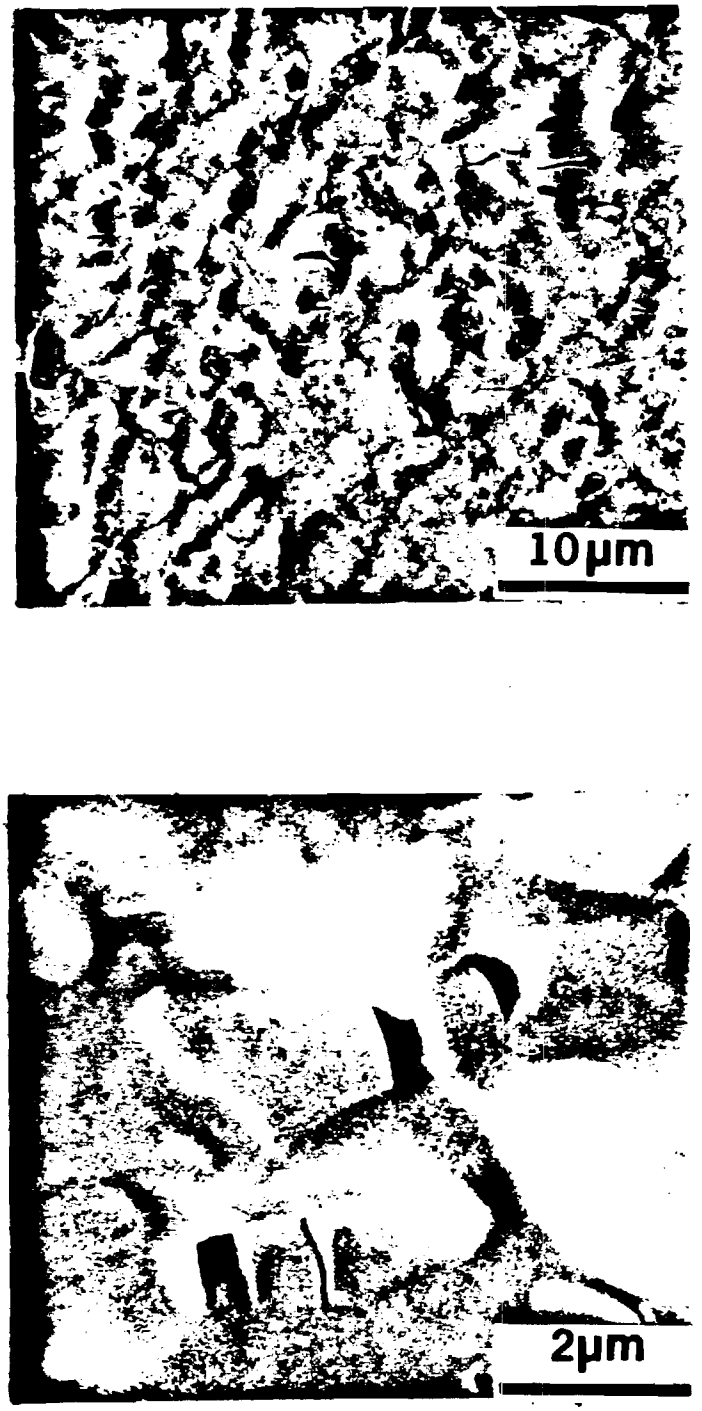

Figure 11. Large and small particled regions of tensile specimen stressed to 67% of expected total elongation, note the separation occurring at the matrix/particle interface.

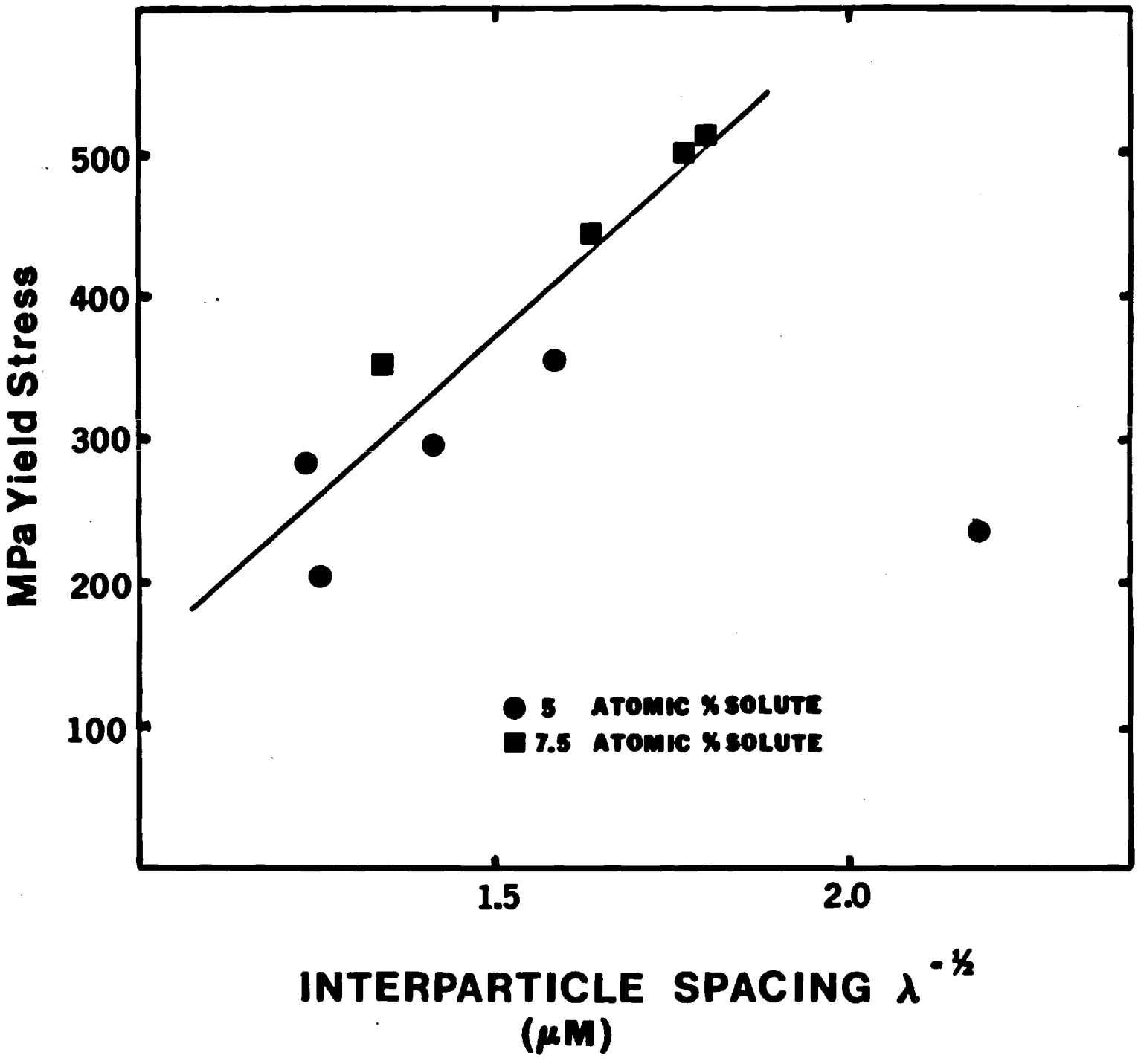

Figure 12 . Effect of Mean Free Distance Between Small Intermetallic Particles ... Yield

PHASE ANALYSIS IN ALLOY 1.12
Al-2Li-3Cu-1Mg-0.2Zr

R. E. Crooks, R. T. Chen, and E. A. Starke, Jr.
Fracture and Fatigue Research Laboratory
Georgia Institute of Technology
Atlanta, Georgia 30332

Three methods were used for the identification of phases, and these are, in order of increasing accuracy: scanning electron microscopy (SEM) with energy dispersive X-ray analysis (EDXA), transmission electron microscopy (TEM) with selected area electron diffraction (SAD), and Guinier X-ray diffraction. A JEM-100C STEM equipped with a KeVex unit was used for the EDXA and SAD studies. A Nonius Guinier-deWolff model II (2r = 114.6mm) was used for X-ray diffraction exposures, which were measured at 7x to a precision of 0.01mm.

EDXA

A large particle associated with voids which formed during a prolonged solution treatment (4h at 538°C), was examined optically and by SEM (Figure 1). EDXA measurements showed a very strong peak for silicon. This suggests the identity Mg_2Si, which was corroborated by the blue color (observed optically) characteristic of that phase [1].

A sample aged 24h at 190°C was etched for one minute in a boiling solution of 10% bromine, 90% methanol, and examined in SEM. EDXA results indicated the large, elongated particles (Figure 2) were rich in iron. In Al-Cu-Mg-Mn alloys the equilibrium tetragonal phase Al_7Cu_2Fe forms during an anneal by the transformation of metastable $(Fe,Mn,Cu)Al_6$ present in the casting [1]. Iron-rich phases in this alloy are likely to be Al_7Cu_2Fe. No significant difference in composition from the matrix was observed for the grain boundary precipitates.

SAD

TEM examination confirmed the identity of the elongated (approximately 0.2 x 1.2 μm) particles as Al_7Cu_2Fe. A bright-field micrograph and the corresponding SAD pattern are given in Figure 3.

Another intermetallic particle, tetragonal Al_3Zr (equilibrium), was identified by SAD, and is shown in Figure 4.

Matrix Precipitates

Based on the information in SAD patterns, the matrix precipitates after aging at 190°C have been identified as S'(Al_2Cu Mg), T_1(Al_2Cu Li) and Al_3Zr (metastable). The [112] and [100] diffraction patterns of the peak aged (2% stretched + 6h 190°C) condition are presented in Figures 5 and 6. The S' phase forms as rods with ⟨100⟩ growth directions, and this causes streaking in directions normal to the rod axes (⟨100⟩). With further growth laths of S' form corrugated sheets on {210} planes with {110} composite planes [2]. This results in streaking in ⟨210⟩ and ⟨110⟩ directions. The hexagonal, T_1 phase precipitates on {111} matrix planes [3], causing ⟨111⟩ streaking. Streaking in ⟨111⟩ directions (due to T_1) is seen in the [112] pattern (Figure 5), as well as ⟨210⟩ and ⟨110⟩ streaking due to S'. The [100] pattern (Figure 6) shows S' ⟨100⟩ and ⟨210⟩ streaks.

A dark field image from a T_1 ($\bar{2}020$) spot and nearby S' reflection is shown in Figure 7. Three variants of S' and one of T_1 are apparent. The beam direction is near [100] and several corrugated sheets of S' are visible in this direction. Some T_1 plates show stacking fault contrast.

A dark field image from a (100) superlattice reflection is shown in Figure 8, for a solution treated sample aged one year at room temperature. The large, spherical particles are metastable Al_3Zr. The small particles (approximately 25 Å in diameter) are probably δ' (Al_3Li). This is not positive identification since streaking from S' crosses all superlattice points (this effect is more pronounced after aging at 190°C, Figure 5). The shape of these very small particles is not very easily resolved and, therefore, it may

be possible to confuse cylindrical S' (or its precursors) for the spherical S' precipitates.

Grain Boundary Precipitates

Two types of precipitates were found along high angle boundaries. Both are rounded and incoherent, indicating that they are equilibrium phases. A bright-field, dark-field pair and diffraction pattern are shown in Figure 9, for the phase identified as S, Al_2Cu Mg. Figure 10 shows a $T_2(Al_6Cu\ Li_3)$ phase particle with the corresponding SAD pattern. Although diffraction information has been reported for this phase [4], the structure has not been determined.

Guinier Analysis

The most precise method of phase determination utilizes X-ray diffraction measurements. Guinier cameras produce high resolution diffraction photographs with low background intensities by utilizing a parafocusing geometry in conjunction with a curved crystal monochromator. The clear background is due to the elimination of other wavelengths than the K_α doublet [5].

The first commercially available Guinier camera, and the type in use at our laboratory, is based on the design of P. M. deWolff [6]. The monochromator is a quartz crystal cut at 4.5 degrees to $(10\bar{1}1)$ and bent in a logarithmic spiral. The K_α doublet is focused at θ = 15 degrees and does not separate completely in the range from 0 to 30 degrees. This design has the advantages that it can be used for different wavelengths, and that the production of the monochromator is not a high precision operation [6].

The focus of the deWolff monochromator is not as sharp as that of the Johannson type [7]. The Johannson monochromator [8] is fully focusing and is the basis for the design of the Guinier cameras presently in use at most X-ray diffraction laboratories [9].

The effect of sample thickness (in the Nonius Guinier deWolff II geometry) on the apparent values of θ and, therefore, d, can be determined from the equation [6]:

$$\Delta\theta_t = \frac{573t\ (\sin 2\theta)}{2(114.6)\cos 30 \cos (2\theta - 30)}$$

$$= 1.44t \text{ deg/mm for } \theta = 15 \text{ deg}$$

For 0 = 15 degrees, and t = 1.27 mm = 5 mil,

$$\Delta\theta_t = 0.183 \text{ deg.}$$

which corresponds to $\Delta d = 0.0351$ Å, and is unacceptably large for quantitative work. The thinnest foils used at this laboratory, have a predicted uncertainty of $\Delta d = 0.0141$ Å at $\theta = 15$ deg. Finer lines have been measured, however, indicating that the preparation method removes particles within a certain depth from the surface. For maximum precision work, powder samples must be used. The optimum powder particle size for Guinier diffraction analysis is 0.010 mm. Below this limit, particle size broadening becomes detrimental [10].

The determination of calibration curves for Guinier cameras has been discussed by Brown [11]. The use of an internal calibrant in Guinier work is considered essential [5,7,10,11]. Slight changes in the sample position relative to the tangent of the focusing cylinder result in large changes in the camera constant, K (deg./mm), as well as changes in the shape of the calibration curve [11,12]. It is, therefore, important for precise work to be able to re-determine the camera constant for each exposure through the use of an internal calibrant. Desirable properties for a calibrant include high purity, a cubic structure, chemical and physical stability, brittleness and an adequate number of reflections over the diffraction range [13]. These conditions are well met by semiconductor grade (99.9999%) silicon [13-15]. A high purity, - 200 mesh silicon powder diffraction standard reference material, SRM 640 [14], distributed by the National Bureau of Standards was used as an internal standard in a test of the reproducibility and precision of measurements at three laboratories [15]. This study suggested the use of an interpolation of measurements based on a second order curve fit

to the silicon lines. The effect of nonuniform film shrinkage was concluded to be negligible.

Although a powder sample, mixed with a powdered standard is required for high quality data, routine work may be performed by applying powder to the surface of thin aluminum foils [16]. Although this technique has been used with aluminum as the standard, it may be useful for the examination of thin foils with a powder standard.

As a result of the recommendations of the Commission on Crystallographic Apparatus of the 11th International Congress of Crystallography, a new film, specifically designed for quantitative X-ray diffraction analysis has been produced by CEAVERKERN AB, Strängnäs, Sweden. This film is particularly useful for Guinier work [9], and offers an exceptionally low level of background chemical fog [17], and was used for the present study.

Experimental Procedure

The samples examined were prepared as foils from specimens in different conditions of aging. The foils were prepared by grinding thin slices to a thickness of 0.06mm. The use of foils instead of powder allows a more realistic examination of the precipitates present in the bulk material. For age hardening aluminum alloys, annealing and aging of powder may result in an excessive amount of precipitation of equilibrium phases, due to the greatly increased surface area available during aging. The disadvantages of the foil method include inaccuracy due to specimen thickness and texture effects on phase orientations. The maximum lateral dimensions allowed by the sample holder were 4 x 16mm. The oscillating stage was not used, and the foils were placed with their centers in the beam path. The foils were supported on the ends by double adhesive tape, so that only the sample was in the beam path.

SRM 640 was not available, and a standard was produced by grinding -20 mesh, 99.999% Si (obtained from Alfa Products,

Thiokol) to pass a 200 mesh screen. The standard was mixed with petroleum jelly and the slurry was painted on the beam side of the samples. The film used was single-coated, CEA, Reflex 15; which was developed in D19, 1:2, for five minutes at 20°C. The radiation used was Cu K_α at 35 kV and 20ma, with an exposure time of 24 hours from the line source of a vertical X-ray tube.

An analysis demonstrated that the diffraction lines for the phase Al_7Cu_2Fe (which has been positively identified by EDXA and SAD) showed a systematic shift from the positions predicted by the Si calibration curve. This shift is clearly due to the position of the calibrant on the surface of the foil. The equilibrium Al_7Cu_2Fe phase shows no range of composition [18] (as opposed to some other Fe-rich intermetallic phases), is not affected by texture, and, in this alloy, is close to the ideal size for Guinier X-ray diffraction studies. Consequently this phase was chosen as an internal standard.

The angle θ, of the diffraction line, is determined by multiplying S(mm) by K (deg/mm). With the best alignment obtained, the factor K was not constant, but varied from 0.2525 to 0.2490 over the range of interest (0 to 30°). By using available powder diffraction data, and assuming monochromatic Cu K_{α_1} radiation, a calibration curve can be determined from K values calculated from the Al_7Cu_2Fe lines. The K values can be shown to have a good fit to a power curve, by least squares analysis.

The effect of particle size on line width in a completely focusing Guinier camera is [10]:

$$L_G = \frac{K\lambda(\text{mm})}{\cos\theta} \frac{2r(\text{mm})}{G(\text{mm})}$$

where L_G is line breadth, r is camera radius, G is particle size and K is approximately 1.

After six hours at 190°C, the T_1 (002) reflection is generated from a thickness and therefore an effective particle size of 50 Å (since the basal plane is parallel to the thickness), so, for 2r = 114.6mm, θ = 9.45 and λ = 1.5405 Å,

$$L_G = \frac{\lambda 2r}{\cos\theta G} = 3.6\text{mm}$$

Very broad lines, such as this, are difficult to measure accurately. To aid in the detection of diffuse precipitate lines, diffraction graphs were generated. The position of the diffraction lines were calculated for each suspected phase, based on the Al_7Cu_2Fe calibration curve. These were then plotted with the same scale as the diffraction patterns, transferred to transparent plastic and superimposed on the film. All of the lines for the phase could then be examined simultaneously.

The aging conditions studied included: room temperature, 6 and 24 hours at 190° C and 2% stretched + 6 hours at 190° C. All measurements were made with the samples in the same position (window) in the camera, to increase accuracy. The diffraction graphs from one of the films proved to be adequate for qualitative inspection of the others. Typical exposures and diffraction graphs are given in Figure 11.

Results

The Guinier analysis confirms the presence of Al_7Cu_2Fe, T_1, S, Al_3Zr (metastable) and T_2. All phases show evidence of precipitation with aging at 190° C with the exception of Al_3Zr. The stable phases Al_3Zr (equilibrium) and Mg_2Si were not present in large enough quantities to be detected. The identical crystal structures of δ', Al_3Li and Al_3Zr (metastable) precluded the identification of δ'.

REFERENCES

1. P. R. Sperry, Trans. ASM, 48, 1956, 904.

2. R. N. Wilson, P. G. Partridge, Acta Met., 13, 1965, 1321.

3. B. Noble and G. E. Thompson, Metal Sci. J., G, 1972, 167.

4. H. K. Hardy, and J. M. Silcock,"The Phase Sections at 500 C and 350 C of Aluminium-Rich Aluminium-Copper-Lithium Alloys," J. Inst. Metals, 84 (1955-56) 423.

5. H. P. Klug, L. E. Alexander, X-ray Diffraction Procedures, John Wiley & Sons, Inc., New York, 1954, 217.

6. P. M. deWolff, "Multiple Guinier Cameras, " Acta Cryst., 1 (1948) 207.

7. R. W. M. D'Eye, and E. Wait, X-ray Powder Photography in Inorganic Chemistry, Academic Press, Inc., New York, 1960, 28.

8. T. Johannson, "Über ein neuartiges, genau fokussierendes Röntgenspektrometer," Z. Phys., 82 (1933) 507.

9. C. M. Foris, Director of the Guinier Workshop for the Denver X-ray Conference, Private Communication.

10. Huber Guinier System 600 Manual, Robert Huber Diffraktionstechnik, Rimsting, West Germany.

11. A. Brown, "Optimal Calibration Curves for Guinier-Type Focusing Cameras," Adv. X-ray Anal., 21 (1978) 289.

12. M. Möller, "On the Calibration and Accuracy of the Guinier Camera for the Determination of Interplanar Spacings," Atomenergi Report, AE-67, AB Atomenergi, Studsvik, Nyköping, Sweden.

13. A. Brown, "X-ray Powder Diffraction with Guinier-Hagg Focusing Cameras," Aktiebolaget Atomenergi, AE-409, Studsvik, Nyköping, Sweden, 1970, 38.

14. C. R. Hubbard, H. E. Swanson, and F. A. Mauer, "A Silicon Powder Diffraction Standard Reference Material," J. Appl. Cryst., 8 (1975) 45.

15. A. Brown, J. W. Edmonds, C. M. Foris, "Reproducibility and Precision of Measurements of Guinier Powder Patterns Using Powdered Silicon Calibrant," Adv. X-ray Anal., 24 (1981) 111.

16. J. W. Edmonds and W. W. Henslee, Applicaton of Guinier Camera, Microcomputer Controlled Film Densitometry and Pattern Search-match Procedures to Rapid Routine X-ray Powder Diffraction Analysis," Adv. X-ray Anal., 23 (1980) 361.

17. S. Abrahamsson, O. Lindqvist, L. Sjölin, and A. Wlodawer, "Preliminary Investigation of a New X-ray Film," J. Appl. Cryst., 14 (1981) 256.

18. A. Munitz, A. Zangvil, and M. Metzger, Met. Trans. A, 11 (1980) 1863.

FIGURES

Figure 1. Mg_2Si particle and adjoining void. Solution treated 4h, 538°C; aged 16h, 190°C. As polished.

Figure 2. Scanning electron micrograph of sample aged 24h, 190°C. Wet ground to 600 grit SiC, bromine etched.

Figure 3. Transmission electron micrograph of tetragonal (c/a=2.35) Al_7Cu_2Fe particle: (a) bright-field, (b) SAD.

Figure 4. Transmission electron micrograph of tetragonal (c/a=4.32) Al_3Zr: (a) bright-field, (b) SAD showing matrix [111] pattern and Al_3Zr $\{204\}$ spots.

Figure 5. Electron diffraction pattern from 2% + 6h 190°C, [112] zone axis.

Figure 6. Electron diffraction pattern from 2% + 6h 190°C, [100] zone axis.

Figure 7. Dark-field transmission electron micrograph from T_1 $(\bar{2}020)$ spot, including nearby S´contributions. Stretched 2% + 6h 190°C, beam direction near [100].

Figure 8. Transmission electron micrograph of a sample aged at room temperature for one year. Dark-field from a (100) superlattice spot.

Figure 9. Transmission electron micrographs of grain boundary precipitation of S, Al_2CuMg: (a) bright-field, (b) dark-field, (c) SAD.

Figure 10. Transmission electron micrograph of a grain boundary precipitate identified as T_2, Al_6CuLi_3: (a) bright-field, (b) SAD.

Figure 11. Representative Guinier-deWolff diffraction patterns and phase diffraction graphs: (a) room temperature aged, (b) 2% + 6h 190° C, (c) 24h 190 C, (d) T_1, (e) T_2, (f) S.

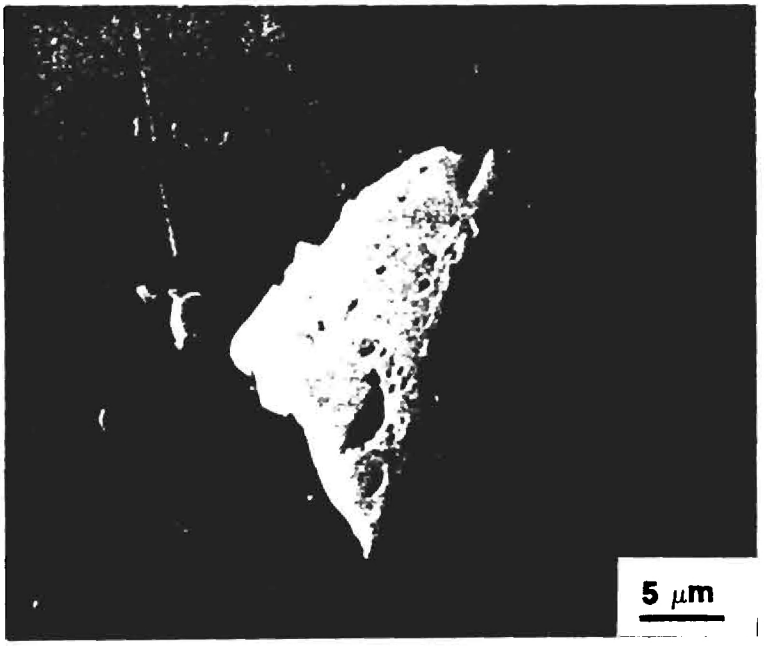

Figure 1. Mg_2Si particle and adjoining void. Solution treated 4h, 538°C; aged 16h, 190°C. As polished.

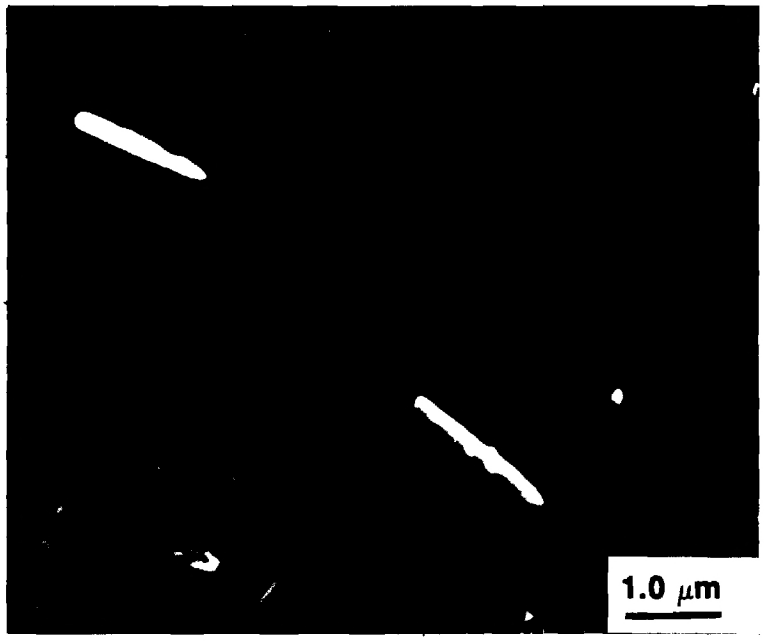

Figure 2. Scanning electron micrograph of sample aged 24h, 190°C. Wet ground to 600 grit SiC, bromine etched.

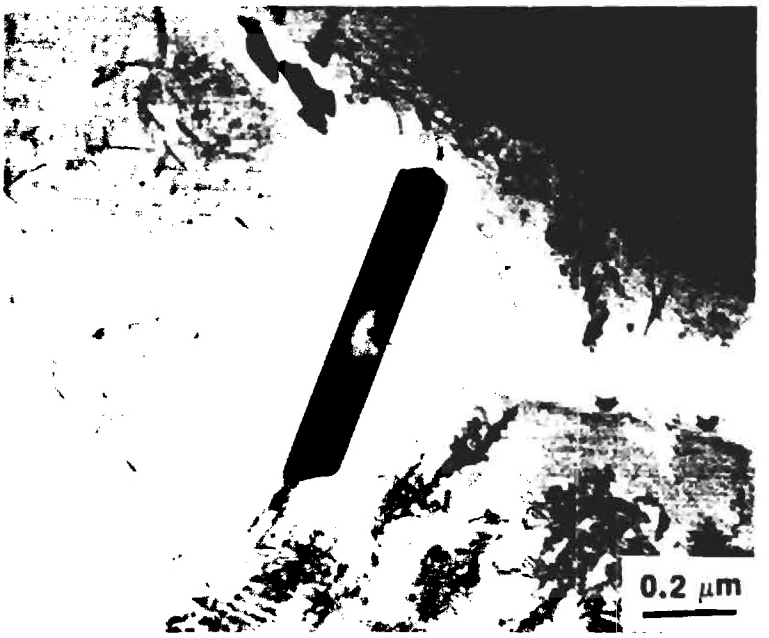

(a)

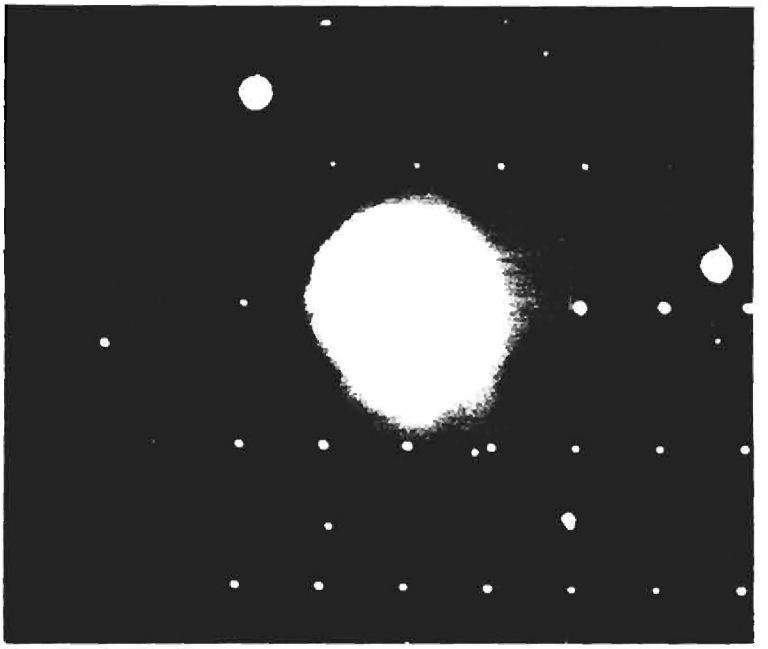

(b)

Figure 3. Transmission electron micrograph of tetragonal (c/a=2.35) Al_7Cu_2Fe particle: (a) bright-field, (b) SAD.

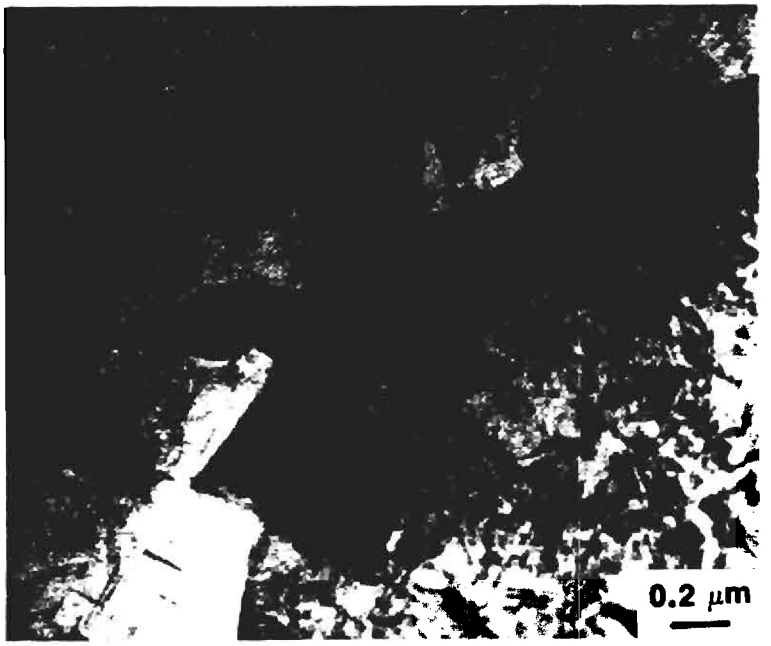

(a)

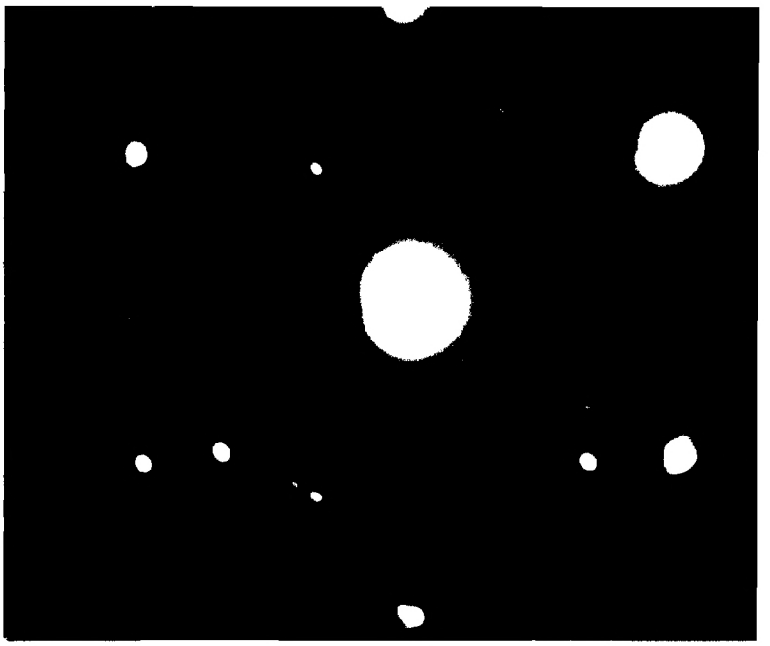

(b)

Figure 4. Transmission electron micrograph of tetragonal (c/a=4.32) Al_3Zr: (a) bright-field, (b) SAD showing matrix [111] pattern and Al_3Zr {204} spots.

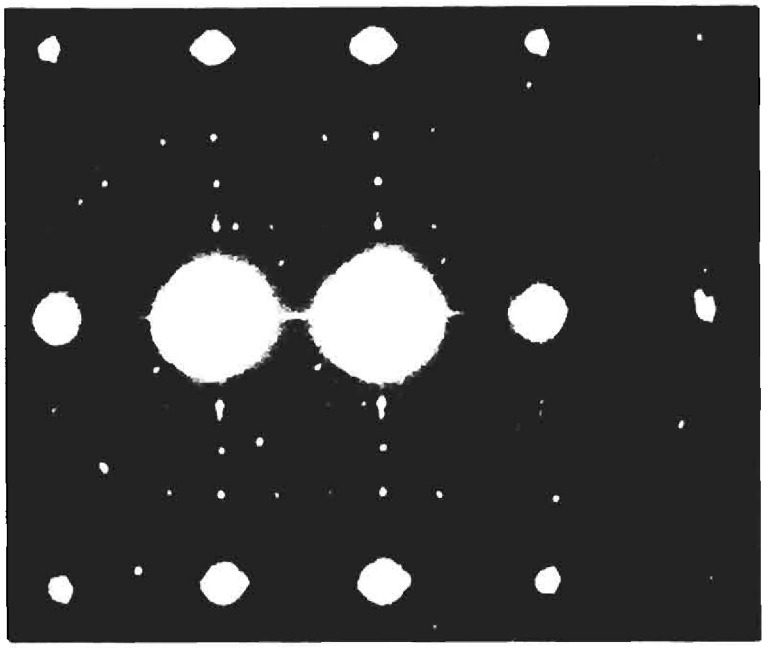

Figure 5. Electron diffraction pattern from 2% + 6h 190° C, [112] zone axis.

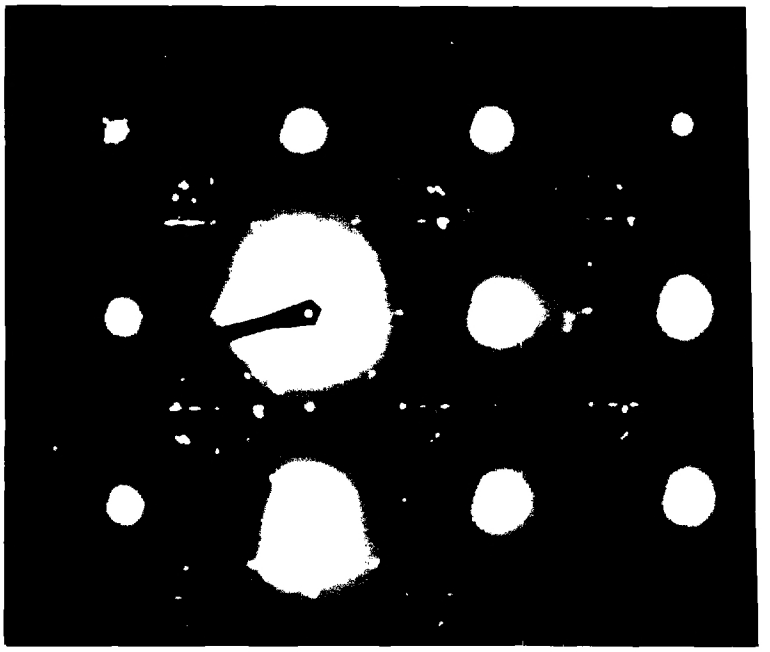

Figure 6. Electron diffraction pattern from 2% + 6h 190° C, [100] zone axis.

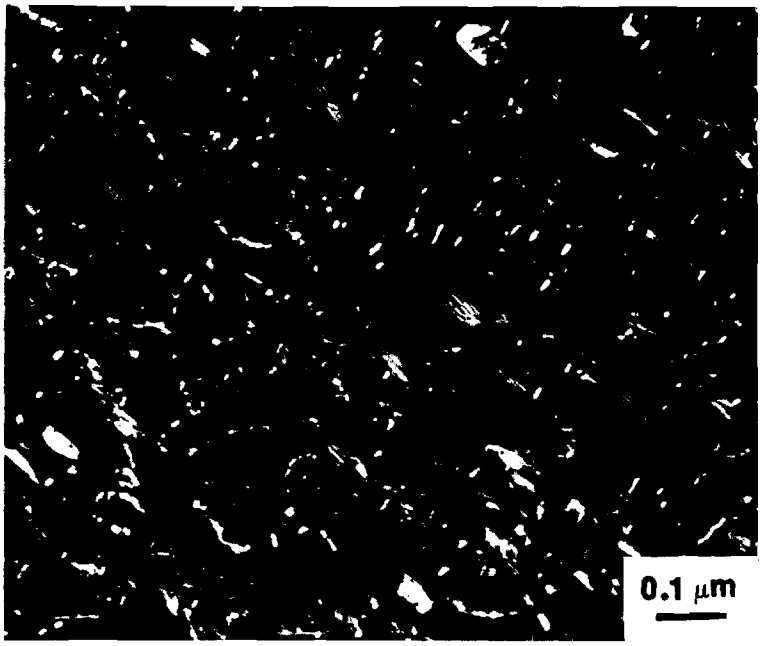

Figure 7. Dark-field transmission electron micrograph from T_1 ($\bar{2}020$) spot, including nearby S′ contributions. Stretched 2% + 6h 190° C, beam direction near [100].

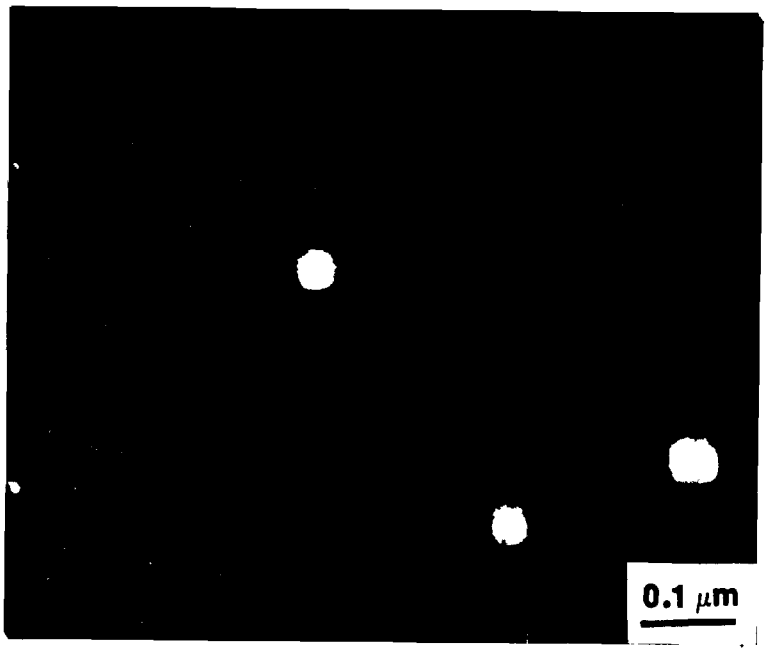

Figure 8. Transmission electron micrograph of a sample aged at room temperature for one year. Dark-field from a (100) superlattice spot.

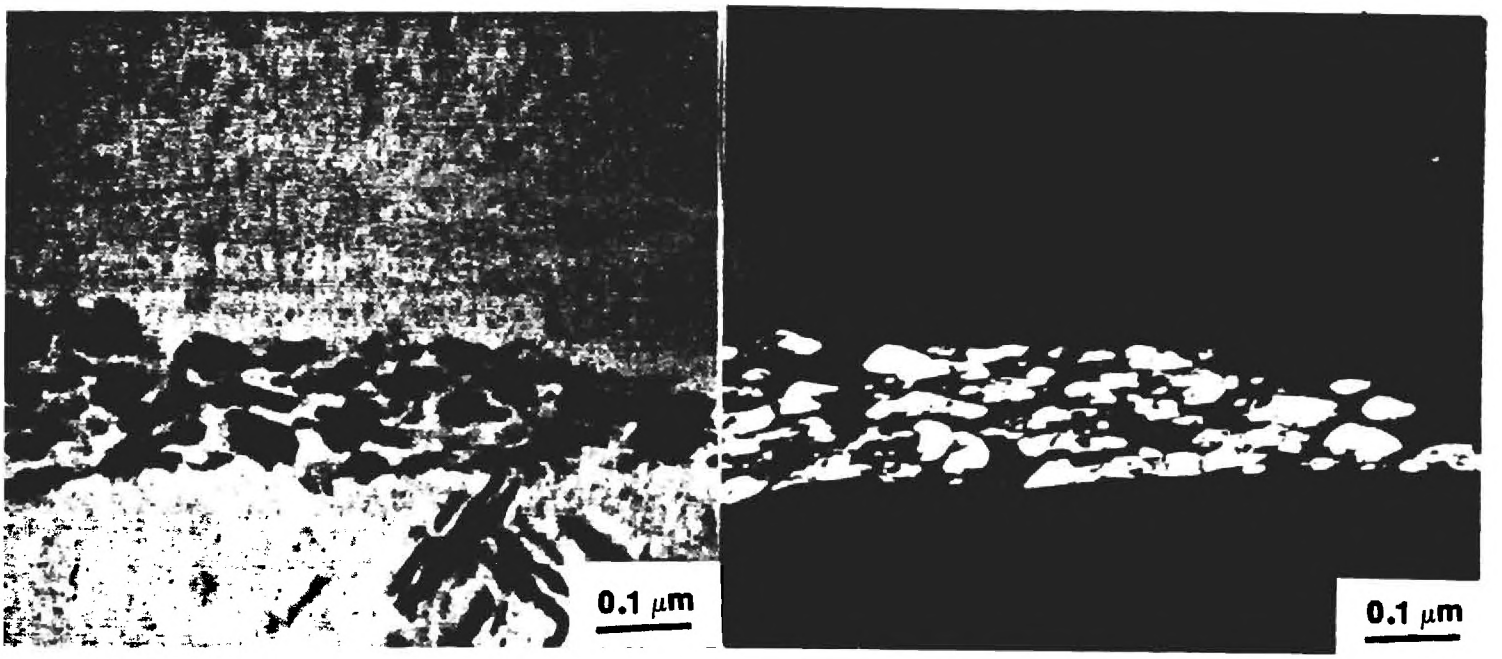

(a) (b)

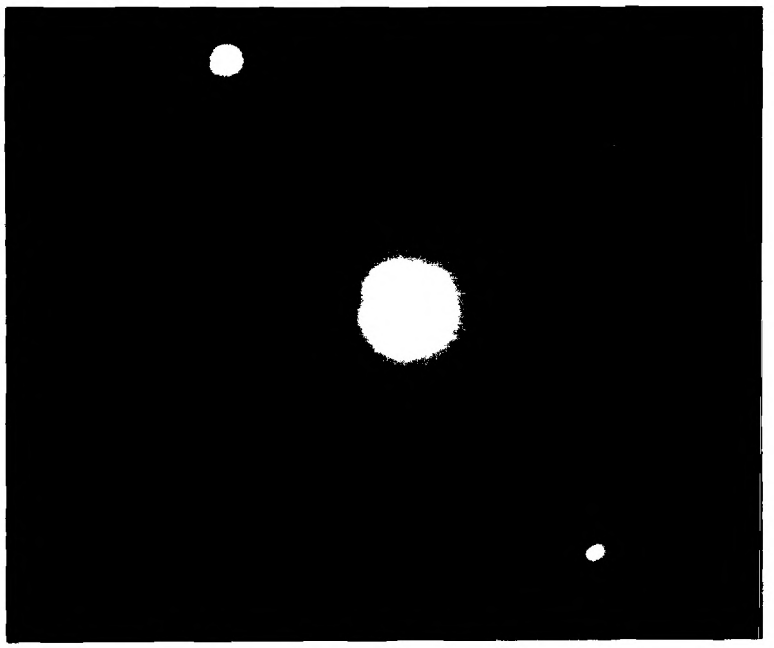

(c)

Figure 9. Transmission electron micrographs of grain boundary precipitation of S, Al_2CuMg: (a) bright-field, (b) dark-field, (c) SAD.

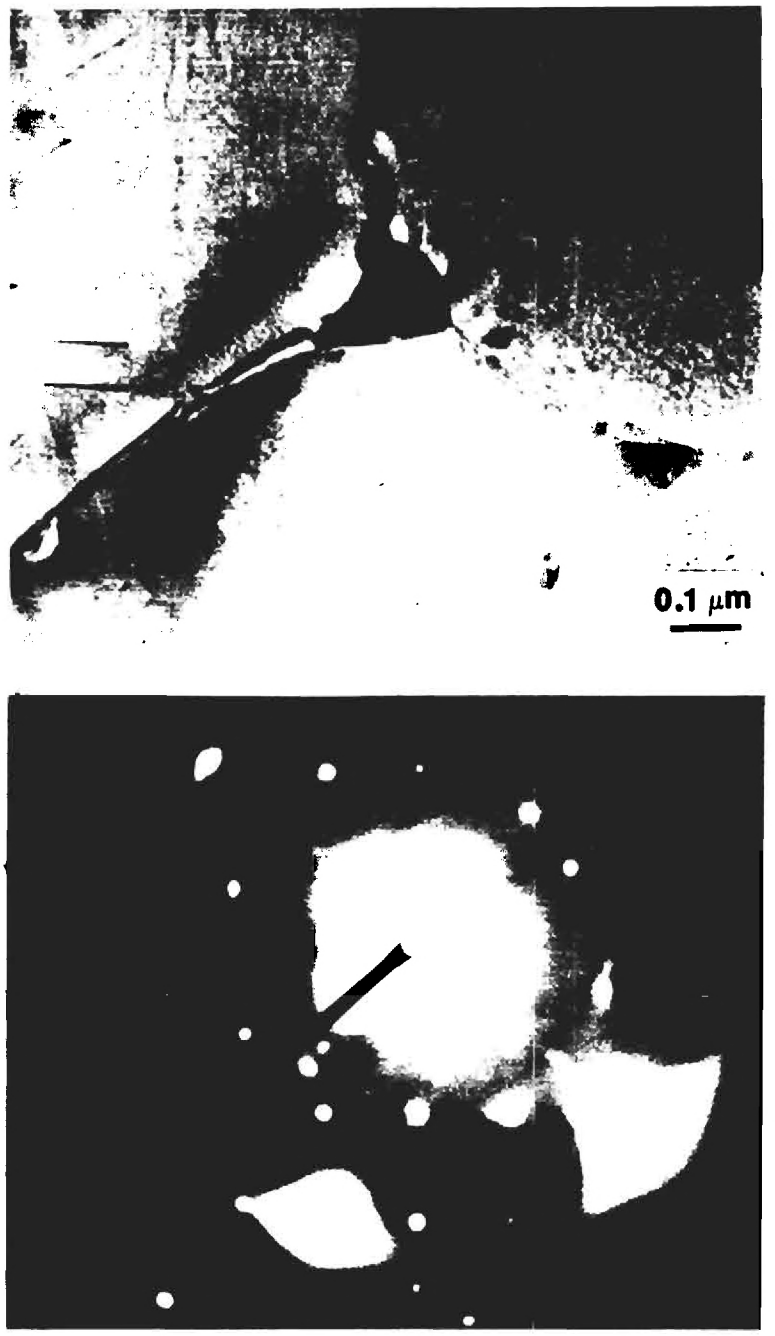

(a)

(b)

Figure 10. Transmission electron micrograph of a grain boundary precipitate identified as T_2, Al_6CuLi_3: (a) bright-field, (b) SAD.

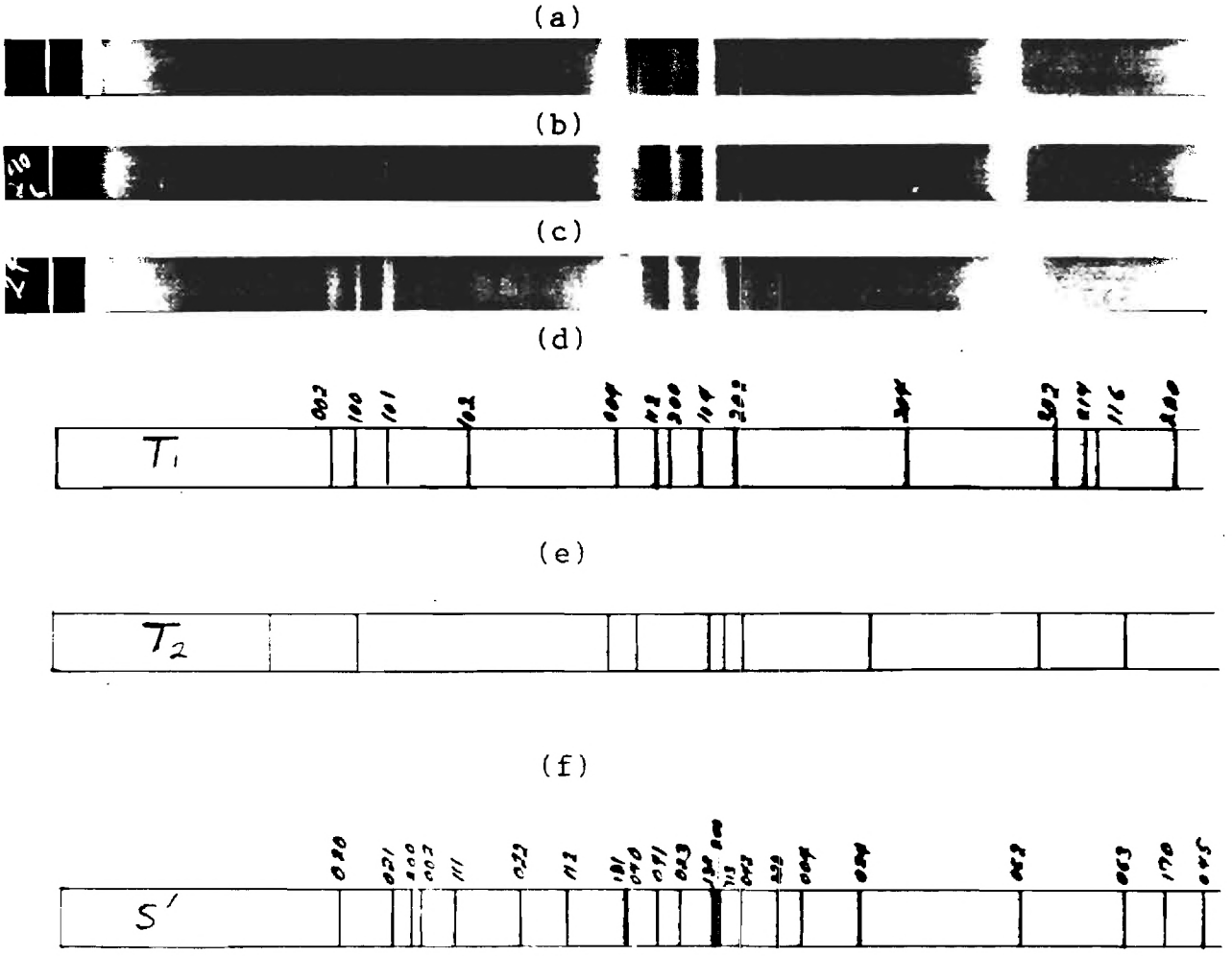

Figure 11. Representative Guinier-deWolff diffraction patterns and phase diffraction graphs: (a) room temperature aged, (b) 2% + 6h 190°C, (c) 24h 190 C, (d) T_1, (e) T_2, (f) S′.

A BRIEF REPORT OF PRELIMINARY WORK ON Al-Li ALLOYS QST AND QSV

R. T. Chen

INTRODUCTION

Two newly developed Al-Li alloys QST and QSV were supplied as 2-inch thick plate by Lockheed Research Laboratory, Palo Alto, California. The nominal compositions are Al-3.0Cu-1.0Mg-2.2Li-0.14Zr and Al-1.7Cu-1.8Mg-3.2Li-0.06Zr for QST and QSV, respectively. Since the received plates were in as-cast condition, the alloys were further processed and characterized prior to fatigue studies. Some of the preliminary experiments are summarized below.

EXPERIMENTAL PROCEDURES AND RESULTS

Homogenization: To avoid melting any low-melting-point phases resulting from previous casting process, a step-heating schedule was selected. The heating schedule for homogenization is shown as follows:

250°C/1 day + 350°C/1 day + 450°C/1 day + 510°C/1 hour + air cooled

Hot Rolling: The plates were preheated at 480°C for 30 min. and hot rolled at the same temperature with a 10% reduction of thickness in each pass. Before hot rolling, the as-received plates were scalped off around 0.25 inch from each surface. Even so, some cracks were still observed on the scalped surface. Furthermore, severe segregation along some grain boundaries was observed across the whole thickness. Figure 1 shows optical micrographs taken from cross sections 1/4 inch and 1 inch below the surface of the as-received QST plate. After scalping, the plate was sliced into two 20 mm-thick plates and this was followed by hot rolling (with finished thickness of 9 mm). Severe cracking occurred on both sides of the plate. It should be noted that severe

surface cracking still occurred, even when a schedule of 5% thickness reduction per pass was adopted.

Differential Thermal Analysis (DTA): DTA was used to determine the transition temperatures of the alloys. The alloy was heated in air at a heating rate of 5°C/min. with Al_2O_3 powder as reference material. Two examples are shown in Figure 2 and Figure 3. The straight line in the lower part of each figure shows heating history (T-t curve); the upper curve is a T-t curve and shows a distinct peak whenever the transition occurs. Figure 2 shows a transition occurred at around 530°C for QSV, and Figure 3 shows a transition occurred at around 540°C.

Solution Heat Treatment (SHT) and Aging: Following DTA results, 550°C was chosen as the SHT temperature for QST. After SHT, the specimens were aged at 190°C in an oil bath. The hardness-time curve is shown in Figure 4. The peak aging condition was determined as 190°C/16 hours.

Tensile Test: Due to the problems encountered in the hot rolling process, it is difficult to prepare a tensile specimen with gage section free of incipient microcracks. Results of one tensile test for QST is included in Table 1. Compared with the Al-Li 2020 alloy, the elongation values are even worse. This could be due to internal cracks which originated during hot rolling.

SUMMARY

Hot rolling for these two Al-Li alloys is practically impossible to proceed. The severe cracking problem during hot rolling may be due to the high density of pores (or cracks) and severe segregation along grain boundaries. A careful control of melting environment and casting practice is suggested.

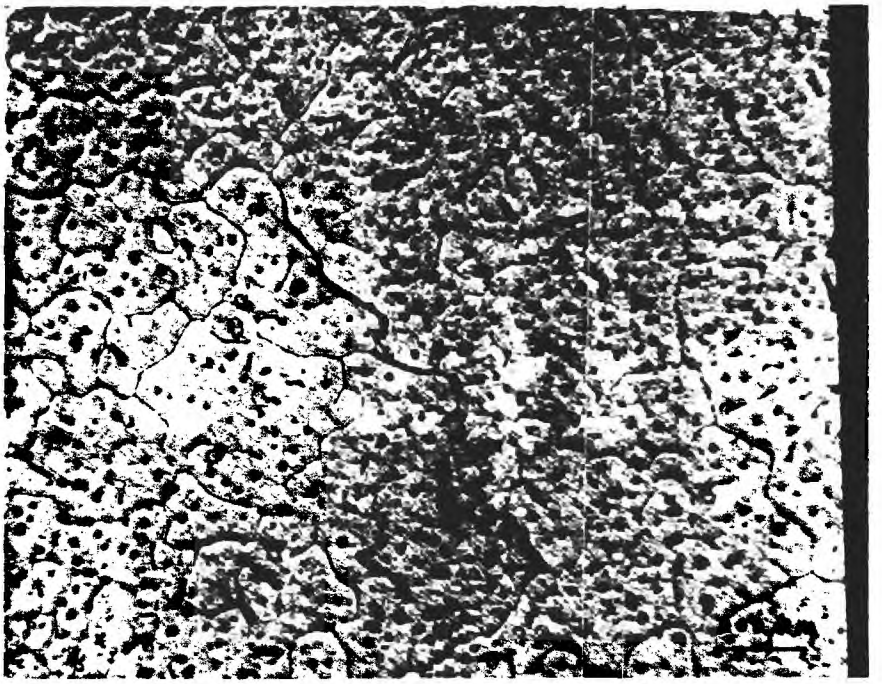

a

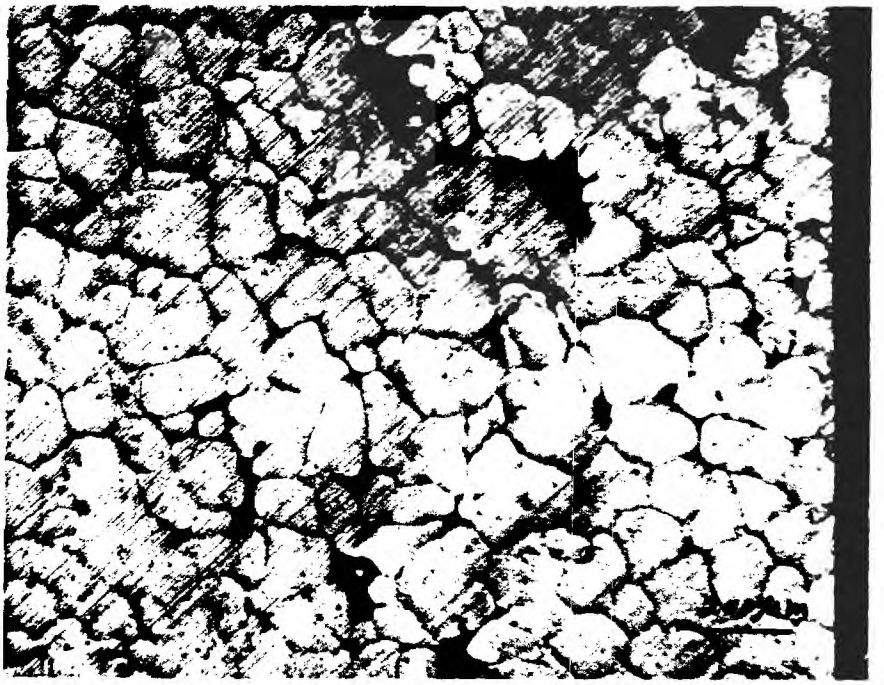

b

Figure 1. Optical micrographs: a) QST, homogenized, 1/4" from the ingot surface, b) QST, homogenized, 1" from the ingot surface.

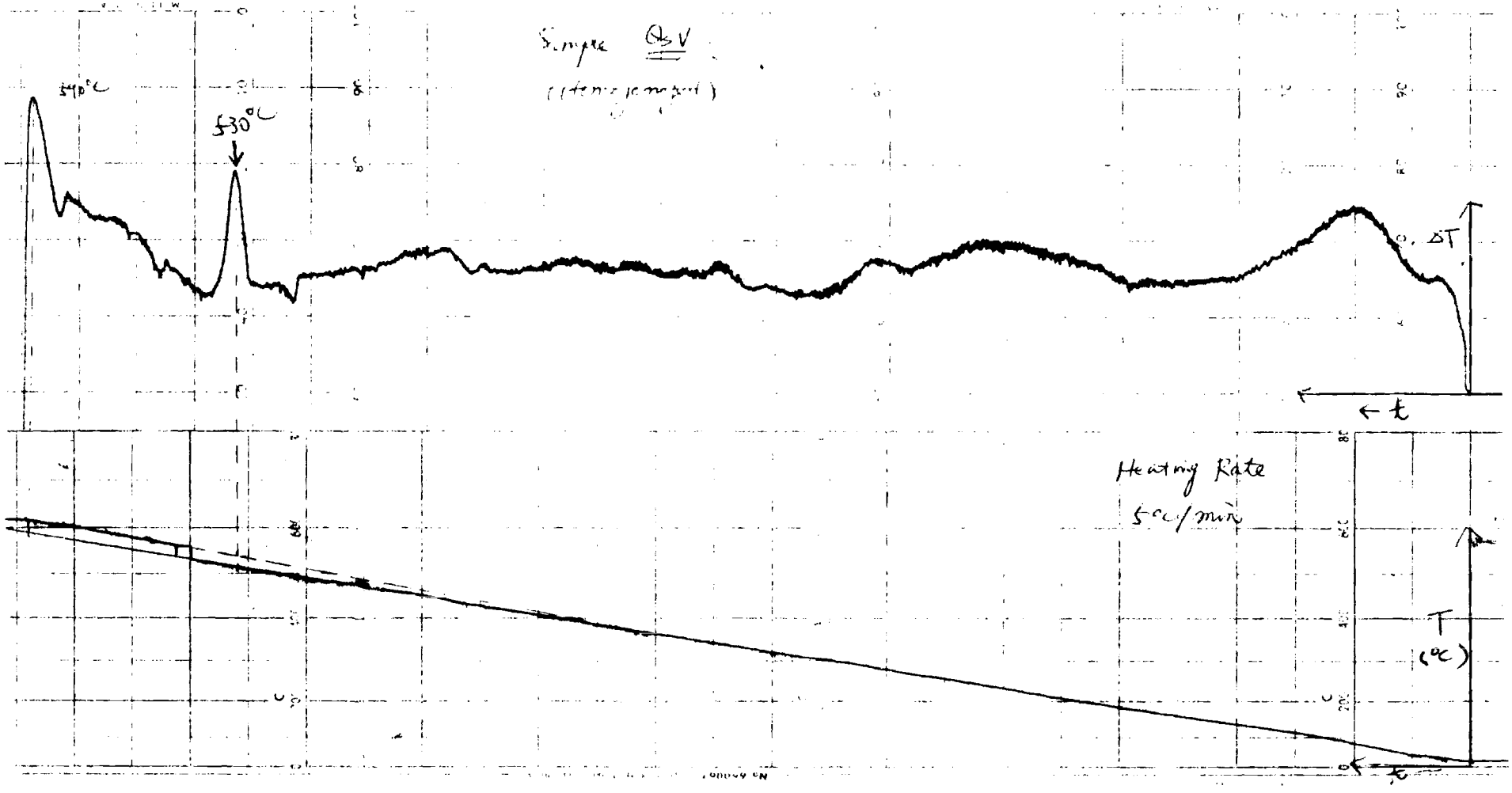

FIGURE 2. DTA RESULT OF QSV ALLOY

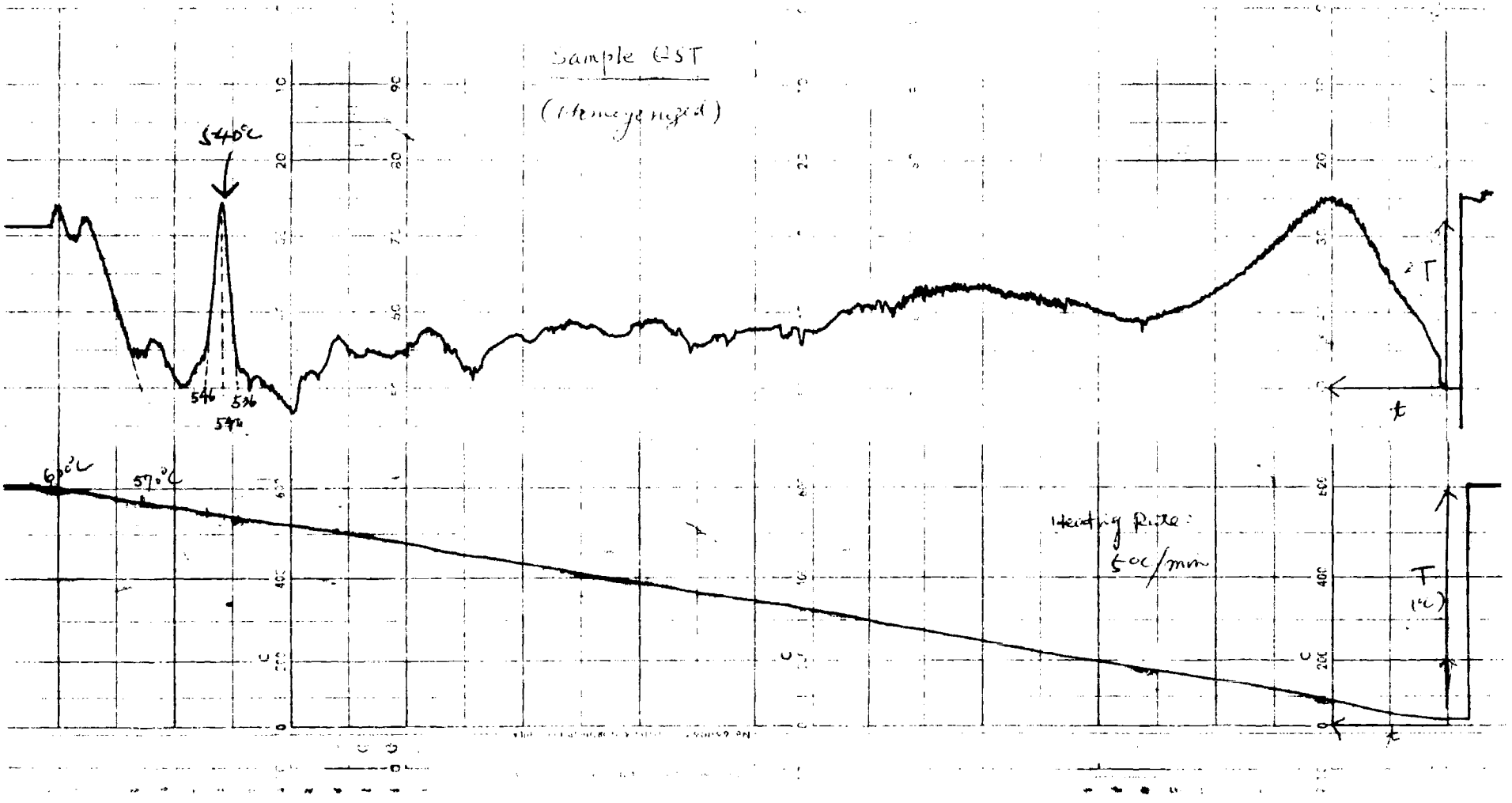

FIGURE 3. DTA Result of QST Alloy

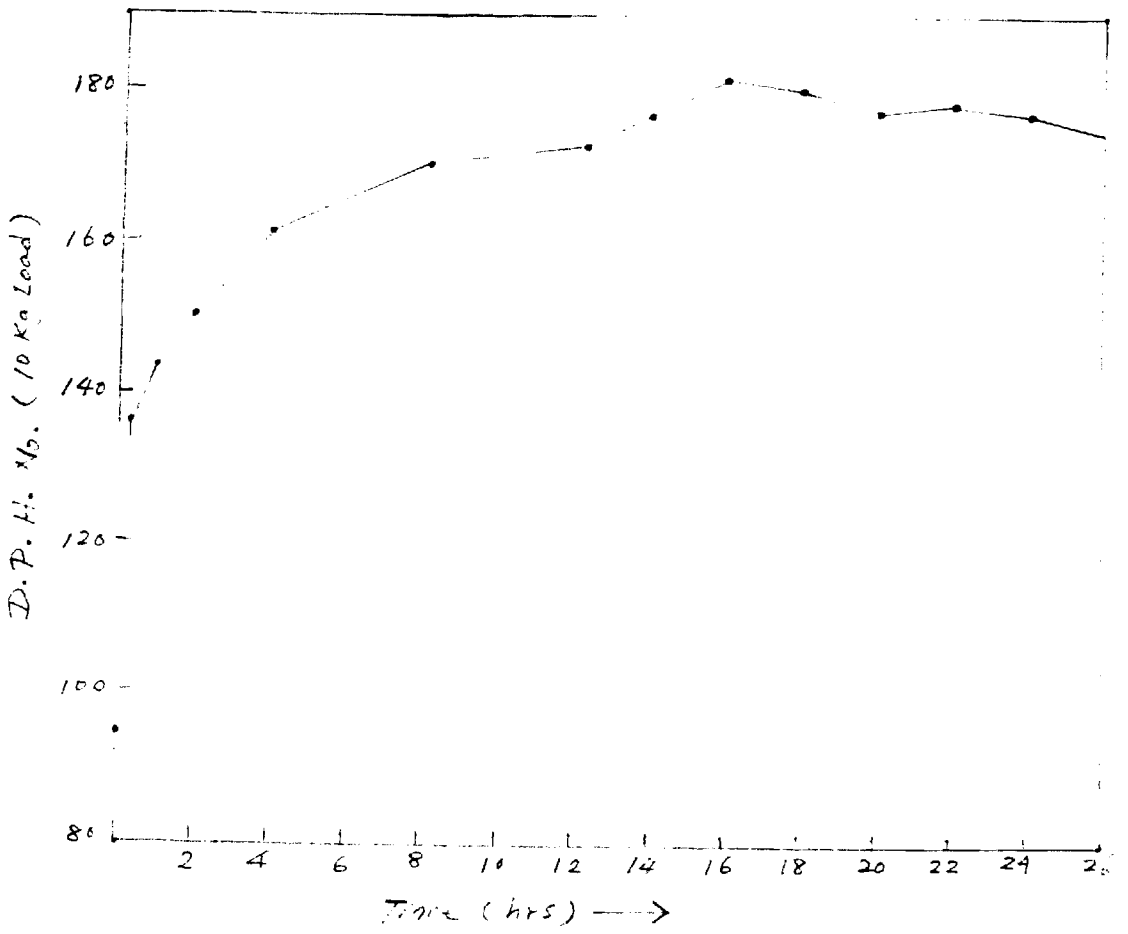

FIGURE 4. Hardness vs. aging time curve for OST alloy at 190°C

TABLE 1. Tensile Properties of QST and A1-2020

Specimen	Yield Stress	Elongation	Young's Modulus
QST	464 MPa	2.6%	77 GPa
A1-2020	531 MPa	3%	79 GPa